

NSG-5205

GODDARD

49497

125P ✓

The Pennsylvania State University

The Graduate School

Department of Meteorology

Dynamic and Static Initialization of a
Mesoscale Model Using VAS Satellite Data

A Thesis in

Meteorology

by

James G. Beauchamp ✓

Submitted in Partial Fulfillment

of the Requirements

for the Degree of

Master of Science

December 1985

(NASA-CR-175967) DYNAMIC AND STATIC
INITIALIZATION OF A MESOSCALE MODEL USING
VAS SATELLITE DATA M.S. Thesis
(Pennsylvania State Univ.) 125 P CSCL 04B

63/47

Unclass
43194

N87-16275

I grant The Pennsylvania State University the nonexclusive right to use this work for the University's own purposes and to make single copies of the work available to the public on a not-for-profit basis if copies are not otherwise available.

James G. Beauchamp
James G. Beauchamp

We approve the thesis of James G. Beauchamp.

Date of Signature

10-25-1985

Thomas T. Warner
Thomas T. Warner, Associate Professor
of Meteorology, Thesis Advisor

1 Nov 85

John A. Dutton
John A. Dutton, Professor and Head
of the Department of Meteorology

10-28-1985

Toby N. Carlson
Toby N. Carlson, Professor of
Meteorology

ABSTRACT

Various combinations of temperature and moisture data from the VISSR Atmospheric Sounder (VAS), conventional radiosonde data, and National Meteorological Center (NMC) global analyses, were used in a successive-correction type of objective-analysis procedure to produce analyses for 1200 GMT 20 July 1981. The NMC global analyses served as the first-guess field for all of the objective analysis procedures. This first-guess field was enhanced by radiosonde data alone, VAS data alone, both radiosonde and VAS data, or by neither data source. All of these objective analyses were utilized in a static initialization of The Pennsylvania State University (PSU)/National Center for Atmospheric Research (NCAR) mesoscale model. In addition, two objective analyses were used in a dynamic initialization: one included only radiosonde data and the other used both radiosonde and VAS data.

The dependence of 12-hour forecast skill on data type and the methods by which the data were used in the analysis/initialization were then investigated. This was done by comparison of forecast and observed fields, of sea-level pressure, temperature, wind, moisture and accumulated precipitation. The use of VAS data in the initial conditions had a slight positive impact upon forecast temperature and moisture but a negative impact upon forecast wind. This was true for both the static and dynamic initialization experiments. Precipitation forecasts from all of the model simulations were nearly the same.

TABLE OF CONTENTS

	<u>Page</u>
ABSTRACT	iii
LIST OF TABLES	vi
LIST OF FIGURES	vii
ACKNOWLEDGEMENTS	x
1.0 INTRODUCTION	1
2.0 DESCRIPTION OF THE 20 JULY 1981 VISSR ATMOSPHERIC SOUNDER (VAS) DATA	6
2.1 Description of the VISSR Atmospheric Sounder	6
2.2 Procedure for VAS-Based Temperature and Moisture Retrieval	7
2.3 Accuracy of VAS-Derived Temperature and Moisture Soundings	9
2.4 Description of VAS-Derived Temperature and Dewpoint Temperature Data for 20 July 1981	10
2.5 Comparison of VAS and Radiosonde Temperature and Dewpoint Temperature Data	11
3.0 SYNOPTIC DISCUSSION	18
3.1 Surface Features	18
3.2 Upper-Air Features	24
3.3 Description of Convective Systems	27
4.0 ANALYSIS OF THE VAS DATA	34
4.1 A Review of the Objective-Analysis Procedure Used with the PSU/NCAR Mesoscale Model	34
4.2 Incorporation of VAS-Derived Temperature and Moisture Data into the Objective Analysis	37
4.2.1 Equal Weighting of VAS and Radiosonde Data in the Objective Analysis	38
4.2.2 Unequal Treatment of VAS and Radiosonde Data in the Objective Analysis	38
4.2.3 Exclusion of Radiosonde Data in the Objective Analysis	39
4.2.4 One-Dimensional Temperature and Moisture Analyses	39

TABLE OF CONTENTS (Continued)

	<u>Page</u>
4.3 Comparison of Objective and Subjective Analyses, Based Upon VAS-Derived Temperature and Moisture Data	44
4.4 Comparison of the Objective Analyses	50
5.0 EXPERIMENTAL DESIGN	65
5.1 Static-Initialization Experiments	65
5.2 Dynamic-Initialization Experiments	67
6.0 THE NUMERICAL MODEL	71
6.1 Model Description	71
6.2 High-Resolution Planetary Boundary Layer Parameterization	76
6.3 Initialization	79
7.0 RESULTS	80
7.1 Verification Procedure	80
7.2 Verification Statistics	81
7.3 A General Comparison of the Forecast Results . . .	85
7.4 Quantitative Precipitation Forecast (QPF) Results	95
7.5 Gravity-Inertia Wave Characteristics of the Forecasts	100
8.0 SUMMARY AND CONCLUSIONS	106
REFERENCES	109

LIST OF TABLES

<u>Table</u>		<u>Page</u>
5.1	Description of the Analysis/Initialization Procedure .	66
6.1	Summary of Model Features and Parameters	72
6.2	Vertical structure of the model. Pressure levels (p) based on $p_{sfc} = 100$ mb, weighting function for convective heating (N), and vertical eddy flux of water vapor (W) are tabulated against sigma at the computational levels	73
6.3	Surface Characteristics Used for Each Surface Index Type	78
7.1	Forecast Verification Statistics	82
7.2	Forecast Precipitation Scale	98

LIST OF FIGURES

<u>Figure</u>		<u>Page</u>
2.1	Differences between radiosonde temperatures and VAS temperatures interpolated to radiosonde locations . .	13
2.2	Same as Fig. 2.1 except dewpoint temperature differences are shown	16
3.1	Sequence of infrared GOES satellite images	19
3.2	Sequence of surface charts	23
3.3	Streamline and isotach analysis of the 500-mb wind .	25
3.4	Streamline and isotach analysis of the 300-mb wind .	26
3.5	Sequence of upper tropospheric relative humidity (%/10) over the VAS image of 6.7- μ m atmospheric water vapor radiance emission (Smith, 1982)	28
3.6	Radar composites	30
3.7	Cumulative precipitation amounts (inches) for the 12-h forecast period from 1200 GMT 20 July through 0000 GMT 21 July 1981. Shaded areas have amounts greater than one inch	33
4.1	Analysis and computational domain for 20 July 1981 case	35
4.2	900-mb one-dimensional temperature and mixing-ratio analyses	40
4.3	Subjective and objective 700-mb temperature analyses based on VAS data, for 1200 GMT 20 July 1981	46
4.4	Subjective and objective 500-mb temperature analyses based on VAS data, for at 1200 GMT 20 July 1981 . . .	47
4.5	Subjective and objective 700-mb mixing-ratio analyses based on VAS data, for 1200 GMT 20 July 1981	48

LIST OF FIGURES (Continued)

<u>Figure</u>		<u>Page</u>
4.6	Subjective and objective 500-mb mixing-ratio analyses based on VAS data, for at 1200 GMT 20 July 1981 . . .	49
4.7	NOVAS and VAS 900-mb temperature analyses for 1200 GMT 20 July 1981	51
4.8	NOVAS and VAS 500-mb temperature analyses for 1200 GMT 20 July 1981	53
4.9	NOVAS and VAS 300-mb temperature analyses for 1200 GMT 20 July 1981	54
4.10	NOVAS and VAS 850-mb mixing-ratio analyses for 1200 GMT 20 July 1981	56
4.11	NOVAS and VAS 500-mb mixing-ratio analyses for 1200 GMT 20 July 1981	57
4.12	NOVAS and VAS 300-mb mixing-ratio analyses for 1200 GMT 20 July 1981	59
4.13	NOVAS and VAS cross-sections of potential temperature and mixing ratio, taken through the stationary front for 1200 GMT 20 July 1981	60
4.14	Differences in the static stability ($^{\circ}\text{K}/50\text{ mb}$) of the 750- to 700-mb layer between the NOVAS and VAS (NOVAS-VAS) analyses	63
6.1	Model terrain for numerical simulations	75
6.2	Surface index distribution for numerical simulations	77
7.1	Sea-level pressure analyses	86
7.2	500-mb temperature (T) and geopotential height (ϕ) analyses	88
7.3	Streamline and isotach analysis of the 500-mb wind	90
7.4	850-mb mixing-ratio (w) analyses	92

LIST OF FIGURES (Continued)

<u>Figure</u>		<u>Page</u>
7.5	Temperature differences between E1 and E2 (E1-E2) for sigma level 0.95	94
7.6	Total predicted rainfall during the 12-h fore- cast period, 1200 GMT 20 July to 0000 GMT 21 July 1981, for experiments E1 to E7	96
7.7	Gravity-wave noise as shown by the temporal variation of $ \partial^2 p^* / \partial t^2 $ for all experiments except E2	101

ACKNOWLEDGEMENTS

I wish to express my sincere gratitude to my thesis advisor, Dr. Thomas T. Warner, for the scientific insight, patient guidance, and continual encouragement that he provided during this research. I would also like to thank Dr. Toby N. Carlson for his critical review of the manuscript.

All of the members of the NWP group deserve much credit for their ready assistance in nearly every aspect of this research. In particular, my thanks go to Dr. Nelson L. Seaman for sharing his expertise with the PSU objective-analysis software and to David R. Stauffer for his assistance with the dynamic-initialization procedure and the forecast verification programs.

My gratitude is also extended to all my friends among the department's graduate students. Their friendship, in good times and bad, helped make graduate school a more pleasant experience. Finally, I offer my special thanks to my parents, Mr. Emmette W. Beauchamp and Mrs. Mary E. Beauchamp, for their constant love, support, and encouragement.

This research was supported by the National Aeronautics and Space Administration under Grant NSG 5205. Computing support was provided by the National Center for Atmospheric Research which is funded by the National Science Foundation.

1.0 INTRODUCTION

The predictive skill of numerical weather prediction models has significantly improved during the past two decades because of the existence of larger, faster computers; more sophisticated model physics; and improved model numerics. This improvement has led to an increased interest in the use of mesoscale models to predict significant mesoscale events such as heavy precipitation. Model predictive skill, however, is limited by how well initial fields of temperature, moisture, and horizontal winds are specified. This is especially relevant for the prediction of mesoscale events.

The horizontal resolution of conventional radiosonde data is frequently too poor to resolve important mesoscale features in the initial conditions of a numerical forecast. Therefore, to improve the predictive skill of a mesoscale model, it is necessary to use other data sources to supplement radiosonde data. Radiometric instruments aboard satellites are capable of sensing atmospheric temperature and moisture with finer horizontal resolution than radiosondes. Therefore, the potential exists for improving the predictive skill of mesoscale models by using high quality satellite data to help specify the initial temperature and moisture fields.

1.1 Previous Use of Satellite Data in Numerical Models

Satellite-derived temperature soundings were first retrieved in 1969 by Nimbus-3. In 1972, operational satellite-derived temperature soundings first became available from the Vertical Temperature Profile

Radiometer (VTPR). Ohring (1979) reviewed a number of studies which attempted to assess the impact of both NOAA-4 and Nimbus-6 temperature soundings upon numerical forecasts. On the average, inclusion of satellite data led to a small improvement in 48-hour, 500-mb geopotential height forecasts.

Atkins and Jones (1975) found that using VTPR data slightly improved numerical forecasts of sea-level pressure and 500-mb geopotential height. However, local weather forecasts would not have been significantly improved by the use of these data in the model. Bonner et al. (1976) and Druyan et al. (1978) also report VTPR data to have a very small positive impact on predictive skill. According to Bonner et al. (1976), the smallness of this impact may be partly due to the VTPR's inability to sense temperatures in areas of extensive cloud cover.

The Data Systems Tests (DST), conducted by the National Aeronautics and Space Administration (NASA) and the National Oceanic and Atmospheric Administration (NOAA), examined the utility of temperature sounding data from satellites in numerical modeling. These temperature soundings were provided by the High Resolution Infrared Sounder (HIRS) and the Scanning Microwave Spectrometer (SCAMS), both on board the Nimbus-6, and by the VTPR on NOAA-4. Several researchers used these satellite data in the DST. Ghil et al. (1979) used a general circulation model to evaluate different methods of satellite temperature assimilation for eleven forecasts generated for periods between January and March 1976. The use of satellite data resulted in a small but statistically significant improvement in 48- and 72-hour

forecast skill. This impact depended upon both the quantity of satellite data used and the method of satellite data assimilation. Tracton et al. (1980), using a different numerical model, found that satellite temperature data had less impact on numerical forecast skill. Atlas et al. (1982) ran 72-hour forecasts on both coarse- and fine-grid models, with and without satellite temperatures, and found that higher model resolution increased the impact of satellite data.

Thus far, experiments have been reviewed which tested the effects of assimilating only temperature sounding data, from polar-orbiting satellites, into numerical forecast models. Polar-orbiting satellites are capable of sensing a particular region only twice per day, a frequency which is insufficient to monitor mesoscale developments. An instrument placed on a geostationary satellite however, is capable of monitoring temperature and moisture structures frequently enough to be useful for mesoscale applications. Such an instrument, first proposed by Suomi et al. (1971), is the Visible Infrared Spin-Scan Radiometer (VISSR) Atmospheric Sounder (VAS) aboard the Geostationary Operational Environmental Satellites (GOES).

Cram and Kaplan (1984) tested the impact of VAS-derived temperature and moisture soundings from 20 July 1981 on a mesoscale forecast. A scheme was developed to variationally adjust the model first-guess field toward temperature and moisture gradients observed by VAS. Variational assimilation of VAS gradients was used because there is often a systematic bias in satellite retrieved temperatures. For this reason, the gradient information is often more reliable than the absolute values (Hillger and Vonder Haar, 1977; Chesters et al., 1981).

It was found that using VAS data improved the forecast of developing potential instability (measured by the 500-mb lifted index) in regions where VAS better resolved mesoscale temperature and moisture features. Also the high temporal resolution of the VAS data allows rather continuous data assimilation during the early part of a numerical forecast. Cram and Kaplan (1984) found that assimilating satellite data from more than one time made a greater impact on the forecast.

1.2 Research Objectives

In this study, VAS-derived temperature and moisture data, available for a 12-hour period on 20-21 July 1981, were used to investigate the utility of VAS sounding data in the initialization of a mesoscale model. Both the impact of satellite data upon forecast skill and the method of VAS data assimilation were evaluated. Three types of data were employed: radiosonde data, VAS data, and data from a smooth global analysis. Several different combinations of these datasets were used to initialize the mesoscale model. Unlike the Cram and Kaplan (1984) study, the absolute values and not the gradients of VAS-derived temperature and moisture were used in a successive-correction type of objective analysis scheme (Benjamin and Seaman, 1985).

A standard static-initialization procedure as well as a dynamic-initialization technique, that is based on a Newtonian nudging procedure, were employed. Geostrophic adjustment theory suggests that for mesoscale motions, the temperature field adjusts to the wind field. Therefore, it is possible that during the forecast, the wind field,

analyzed using data solely from a synoptic-scale radiosonde network, could smooth out some of the mesoscale detail in the temperature field provided by the VAS satellite data. The dynamic-initialization period allows the wind field to adjust to the VAS-scale temperature analysis, even though this is attempting to force the adjustment in an unnatural way for this scale of motion.

1.3 Thesis Organization

Chapter 2 describes the VAS instrument, the VAS dataset used for this research, and the consistency between these data and radiosonde data. The 20-21 July 1981 synoptic situation is discussed in Chapter 3. Chapter 4 relates how VAS-derived temperature and moisture data were incorporated into an objective-analysis scheme. It also compares initial conditions with and without VAS data. The experimental design for model forecasts using various initial conditions is described in Chapter 5. The numerical model used to perform these experiments is discussed in Chapter 6. Chapter 7 describes the forecast verification and presents the results of all the experiments. Finally, Chapter 8 contains a summary and some conclusions.

2.0 DESCRIPTION OF THE 20 JULY 1981 VAS DATA

The VISSR Atmospheric Sounder, first launched aboard the GOES-4 satellite in 1980, is a major improvement over the VISSR which was first carried on the SMS/GOES-series satellite during the 1970's. Situated on a geosynchronous satellite, the VAS can monitor the development of mesoscale weather systems. This chapter includes a description of the VAS instruments, the retrieval algorithm, and the accuracy of VAS-derived temperature and moisture profiles. For more information on the VAS instrument and retrieval method refer to Chesters et al. (1982), Lee et al. (1983), and Smith (1983). The 20 July 1981 dataset used for this research will also be discussed.

2.1 Description of the VISSR Atmospheric Sounder

The VAS senses upwelling radiances in 12 spectral bands. Each of the 12 channels has a 15-km horizontal resolution at nadir (some also have a 7-km resolution) and a 5-km vertical resolution. Channel wavelengths, chosen to distinguish the effects of tropospheric temperature, moisture, and cloud cover upon upwelling radiances, lie between 4 and 15 microns. Of these 12 channels, 7 are used to detect temperature, 3 measure moisture, and 2 window channels sense surface temperatures.

The VAS can be operated in two modes: a Dwell Sounding (DS) mode and a Multi-Spectral Imaging (MSI) mode. The DS mode is used to determine complete temperature and moisture profiles. It uses

radiance from all 12 channels and employs two methods for improving channel signal-to-noise ratio. The first method, called "dwell averaging", temporally averages channel radiance from several spins along the same line. This is possible because the VAS spins in a west to east direction at 100 revolutions per minute. Channel noise characteristics determine the required number of spins to be averaged over, or the spin budget, for each channel. In the second method, spatially averaging the radiance of several fields-of-view further reduces radiometric noise but also lowers the effective horizontal resolution. In the DS mode, the VAS can observe a band of earth, 20 degrees in latitude wide, in approximately 30 minutes.

The presence of low clouds, high terrain, and irregular surface emissions makes the accurate interpretation of VAS radiance data impossible. For this reason, careful selection of sounding sites is necessary for successful soundings.

2.2 Procedure for VAS-Based Temperature and Moisture Retrievals

Jedlovec (1984) cites three VAS retrieval methods: physical, modified physical, and linear regression. For physical retrievals, an inverted form of the radiative transfer equation is solved iteratively. The modified physical procedure uses an analytic solution to enhance vertical structure. Smith (1983) describes these two procedures in detail. In the linear regression technique, local radiosonde and surface data determine statistical relationships between radiance data and sounding structure so that temperature and moisture profiles can be estimated from radiance measurements. Chesters et al. (1982) and

Lee et al. (1983) explain linear regression retrievals. The data used in this research were obtained using the linear regression approach.

The accuracy of the VAS retrievals depends upon the quality and availability of conventional data used in the regression. Chesters et al. (1982) found that retrievals using "local" weather statistics have smaller residual errors than those using "global" data. Coincident satellite/radiosonde observations are often used to ensure good statistical training and to provide a means for retrieval testing.

VAS retrievals are only possible over cloudless regions because the linear regression technique assumes clear-column radiances. In order to have enough radiosonde data for an accurate regression, it may be necessary to select radiosonde observations near the edge of clouds. For these cases, it is necessary to increase the radiosondes' dewpoint depressions so that better regression correlations with clear-air radiances are achieved. Although adjusting radiosonde observations in this manner biases retrievals toward drier air, it nearly always improves VAS retrievals.

Lee et al. (1983) found that using surface temperature and dewpoint temperature data in the statistical training base significantly improved VAS-derived temperature and dewpoint temperature values in the boundary layer. Surface data are necessary because VAS channel weighting functions are too broad to resolve the fine vertical temperatures and moisture structure of the boundary layer. Near midday, surface temperatures are especially important because radiosonde training is not available and because surface (skin) temperatures from the VAS window channels are too high.

2.3 Accuracy of VAS-Derived Temperature and Moisture Soundings

Chesters et al. (1982), Jedlovec (1984), Lee et al. (1983), and Mostek et al. (1983) have investigated the accuracy of VAS-derived temperature and moisture soundings by comparing the VAS data with appropriate radiosonde data.

Mostek et al. (1983) used conventional radiosonde data to evaluate the accuracy of VAS-derived temperature and dewpoint temperature data from 6 March 1982. Retrieval residuals (root-mean-square differences) were calculated for the same radiosonde observations used for the regression equation. Residuals for both temperature and dewpoint temperature were best at the surface (less than 1°C) because of their high correlation with surface reports. Temperature errors were greater at 920 mb and 850 mb (2°C), and then they decreased with height through the 500-mb level (1.4°C). Dewpoint temperature retrieval residuals increased with height through the 700-mb level (4.3°C). Above 700 mb, the large moisture variance rendered further comparison impossible. Chesters et al. (1982) and Lee et al. (1983) found similar retrieval residuals for different cases. Chesters et al. (1982) reported that these errors were comparable to those of polar-orbiting satellites.

A number of factors contribute to errors in VAS retrievals. The VAS has poor vertical resolution because its infrared channels have such broad weighting functions. This poor vertical resolution makes it impossible to consistently capture fine vertical structure in the atmosphere. It follows that large temperature and dewpoint temperature errors are more likely to occur just above the surface where there is greater atmospheric variability. Jedlovec (1984)

reports that the greatest temperature errors are associated with temperature inversions. Large temperature errors are also probable near the tropopause because the VAS's 15 micron CO₂ channels cannot resolve the marked changes in lapse rate characteristic of the tropopause. Accurate moisture sounding in the lower troposphere is difficult because there is only one channel designed to sense moisture at this level. Instrument noise and calibration error are other sources of error.

Chesters et al. (1982) found that the mean errors in VAS retrievals were greater than the standard deviations. This supports the theory that gradient information from VAS retrievals may be more useful than absolute values (Hillger and Vonder Haar, 1977; Chesters et al., 1982). Chesters et al. (1982), Jedlovec (1984), and Mostek et al. (1983) all found that the VAS was usually able to capture temperature and moisture gradients, however, these VAS gradients were often too weak.

2.4 Description of VAS-Derived Temperature and Dewpoint Temperature Data for 20 July 1981

The VAS-derived temperature and dewpoint temperature data used in this study were supplied by the Severe Storms Branch, Laboratory for Atmospheres at the Goddard Space Flight Center. Keyser (1983) discusses the details of this dataset. The VAS-derived temperature and dewpoint temperature soundings were available at five times: 1202, 1502, 1802, 2102, and 2301 GMT 20 July 1981. Retrieval sites were approximately 100 km apart and were located between 29° and 48°N and 86° and 102°W. VAS soundings ranged in number from 192 to 225,

depending on cloud cover. VAS-derived temperature and dewpoint temperature values were defined on fifteen pressure levels: 1000, 920, 850, 700, 600, 500, 400, 350, 300, 250, 200, 175, 150, 125, and 100 mb. The data also included estimates of surface values of pressure, temperature, and dewpoint temperature. Surface temperature and dewpoint temperatures were interpolated bilinearly from surface airways sites to retrieval locations.

Radiosonde observations from 1200 GMT 20 July (26) and from 0000 GMT 21 July (24), were used to calculate the correlation-coefficient matrix. Visible imagery helped ensure that radiosonde soundings were selected from cloud-free regions. Radiance measurements from 11 VAS channels and surface airways observations comprised the statistical predictors for this regression.

2.5 Comparison of VAS and Radiosonde Temperature and Dewpoint Temperature Data for 20 July 1981

Temperature and dewpoint temperature data from the VAS and radiosonde observations were compared to determine the consistency between the two datasets. Radiosonde observations from both 1200 GMT and 0000 GMT were selected, provided that they were located in an area having a sufficient density of 1202 GMT and 2301 GMT VAS data. For each case, a composite VAS-derived temperature and dewpoint temperature sounding was produced by interpolating nearby VAS soundings to the radiosonde location using a distance-weighted influence function. A correction was applied to the radiosonde location at each level to account for balloon drift. Twenty-five pairs of radiosonde and interpolated VAS soundings were then compared by computing

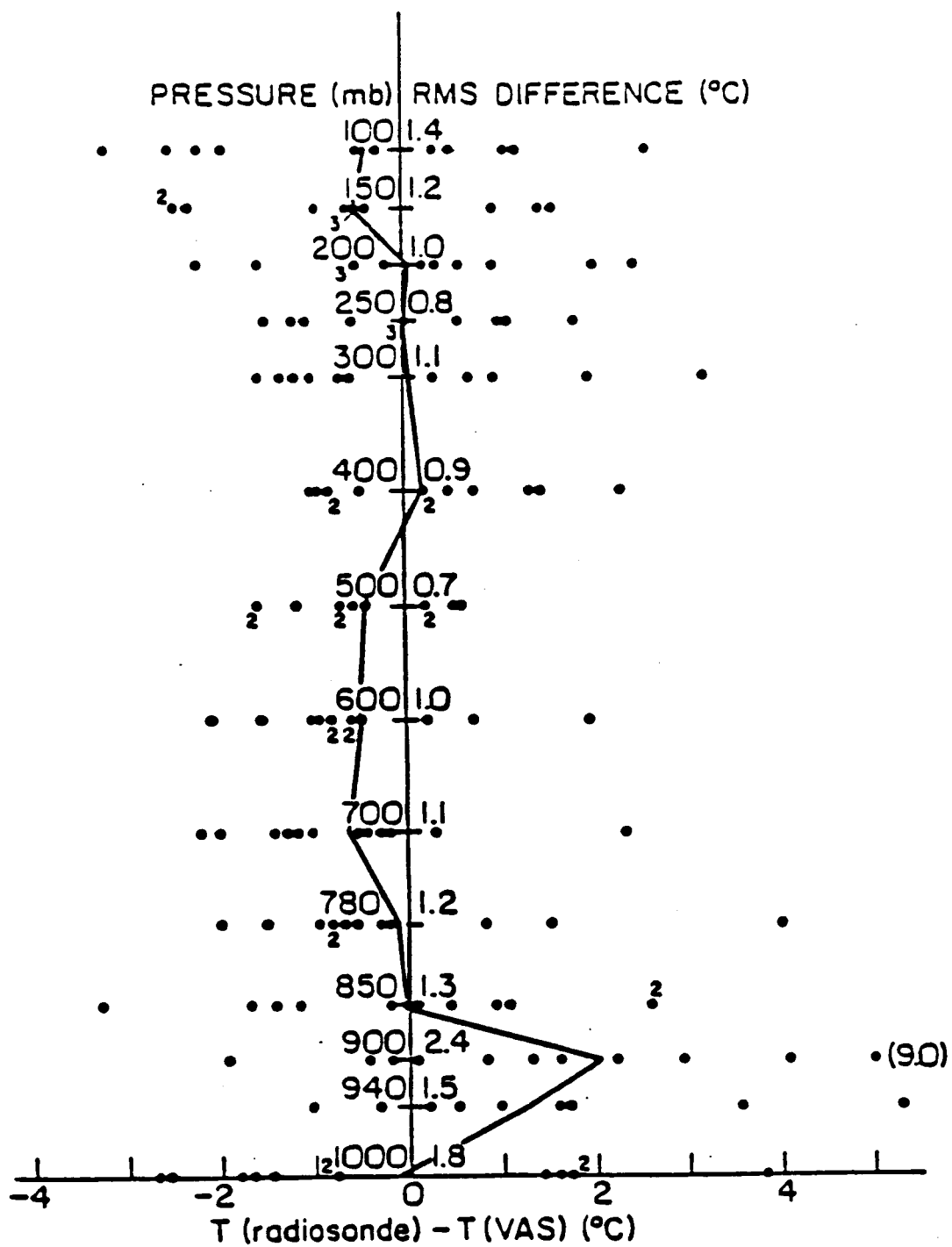
root-mean-square (rms) differences and mean differences at the objective analysis pressure levels.

Differences between the data resulted from vertical interpolation of the VAS and radiosonde data to the analysis levels, from the horizontal interpolation to the location of each radiosonde observation, from the horizontal interpolation to the location of each radiosonde observation, from errors in regression equations, and from the measurement error of both the VAS and radiosonde instruments. The relative contribution from each of these sources of error was difficult to assess, but from a practical standpoint, the differences did reflect how inconsistent the two data sources were for each of the analysis pressure levels.

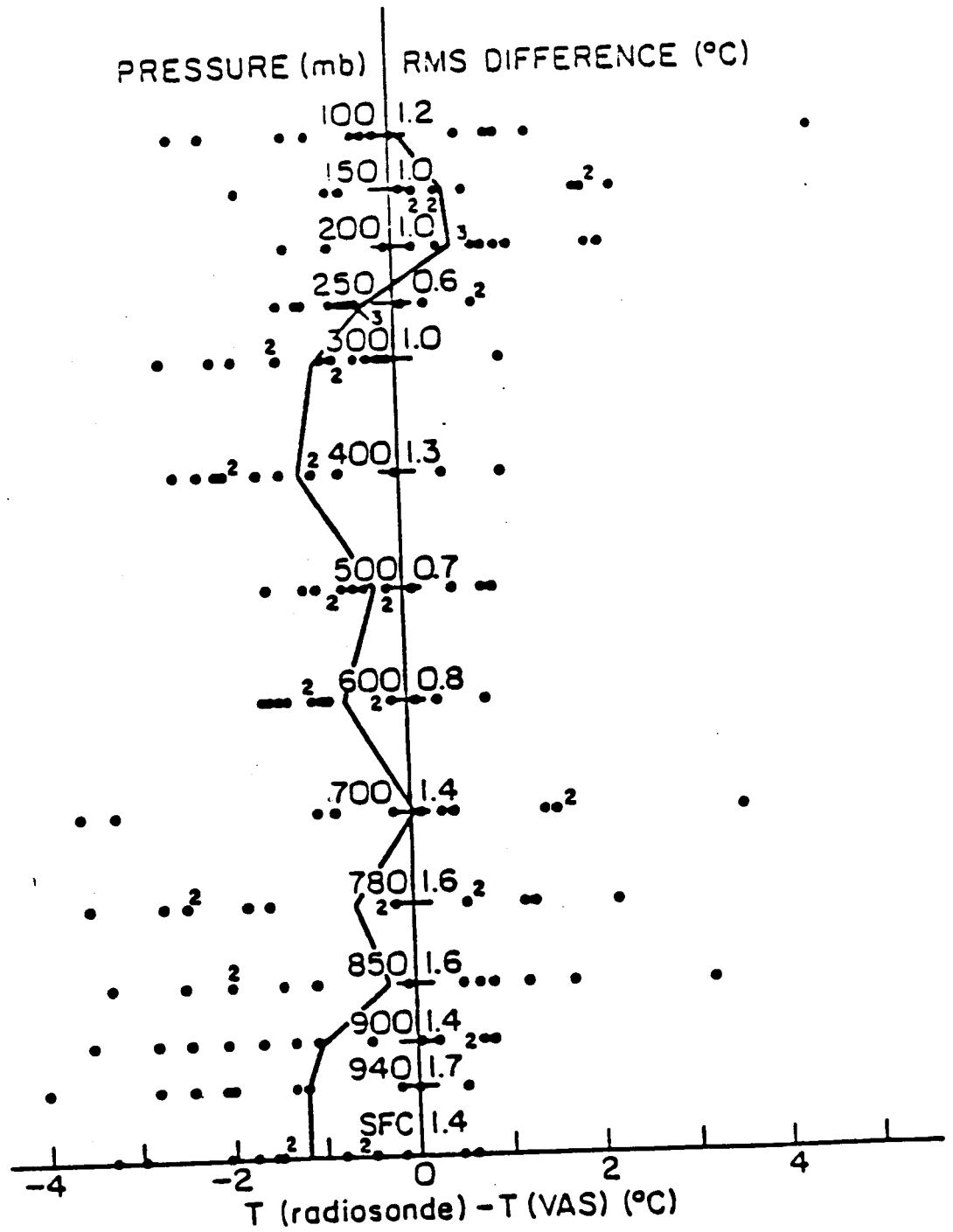
Figures 2.1a and 2.1b illustrate both the rms differences and the mean differences between horizontally interpolated VAS-derived temperatures and radiosonde temperatures at each of the analysis levels for 1200 GMT and 0000 GMT. Figures 2.2a and 2.2b do likewise for interpolated-VAS and radiosonde dewpoint temperatures. For both times, temperature rms differences are greatest below the 850-mb level and then gradually decrease with height through the middle troposphere. Dewpoint temperature rms differences are lowest below 850 mb and increase markedly with height above this level. Mean temperature differences at 1200 GMT indicate a cold bias for VAS-derived temperatures between the surface and 850 mb; above 850 mb, VAS-derived temperatures do not have any systematic bias. There is a weak warm bias for VAS-derived temperatures throughout the troposphere at 0000 GMT. There appears to be no systematic bias in the

Figure 2.1 Differences between radiosonde temperatures and VAS temperatures interpolated to radiosonde locations. Each dot represents an intercomparison of the two data sets at a radiosonde site. Comparisons were made at the levels for which objective analyses of the initial data were performed by the model preprocessing software. Numbers in parentheses at the left and right (if any) show the value of temperature differences that fall off the scale. The line shows the arithmetic average of the data differences to illustrate the existence of any systematic bias at a given level.

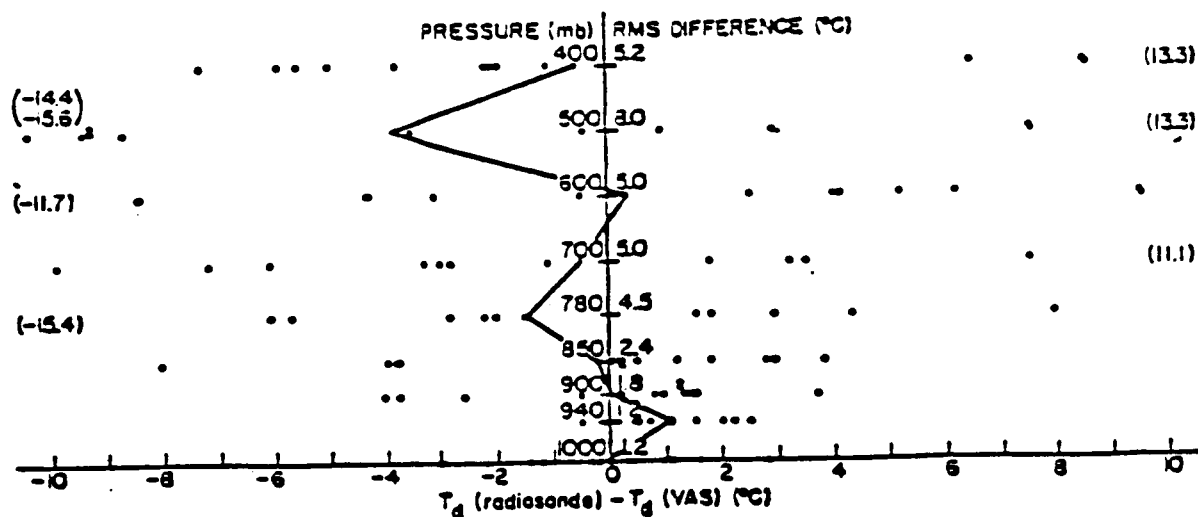
- a. 1200 GMT 20 July 1981
- b. 0000 GMT 20 July 1981



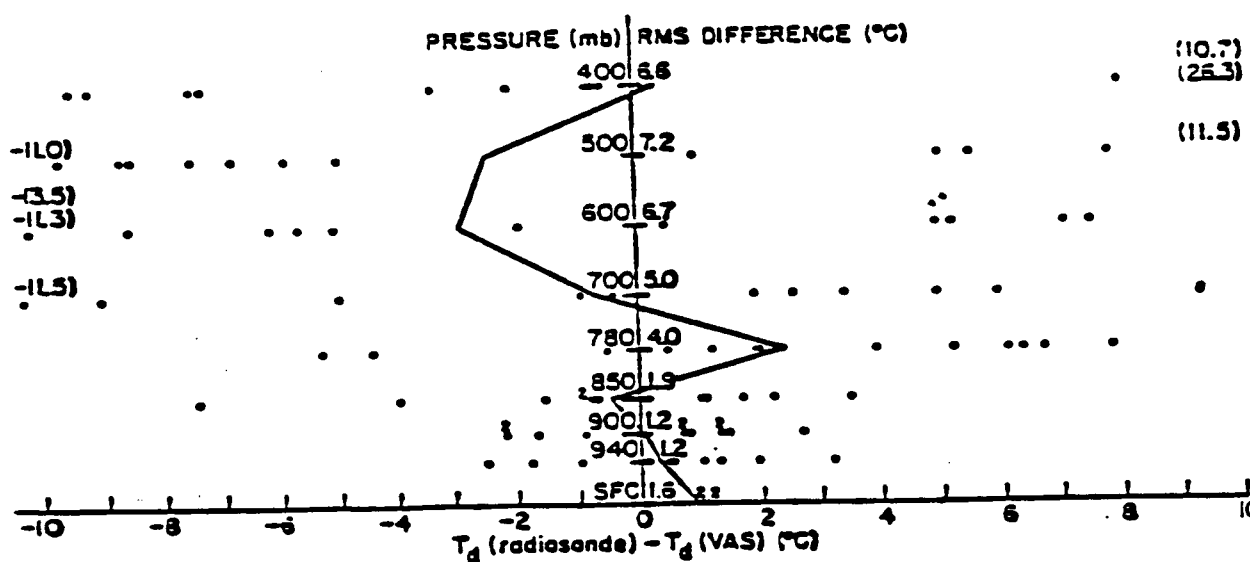
(a)



(b)



(a)



(b)

Figure 2.2 Same as Fig. 2.1 except dewpoint temperature differences are shown.
 a. 1200 GMT 20 July 1981
 b. 0000 GMT 21 July 1981

VAS-derived dewpoint temperatures for either time. These temperature and dewpoint temperature rms differences are consistent with similar studies reviewed earlier in this chapter.

3.0 SYNOPTIC DISCUSSION

The synoptic situation prevailing during the 20 July 1981 case-study period has been discussed by Smith et al. (1982), Keyser (1983), Petersen et al. (1983a,b), and Cram and Kaplan (1984). Infrared imagery from 0000 GMT 21 July (Fig. 3.1c) shows two major areas of convection that evolved during the daylight hours of 20 July 1981 over central United States. The first convective cell, which extended over eastern Missouri and southern Illinois, became visible at approximately 2000 GMT and drifted southeastward during that afternoon. The second major convective area, a line of cells extending from the Texas panhandle, across Oklahoma, and into southern Missouri developed after 2100 GMT. Infrared imagery for 1200 GMT (Fig. 3.1a) indicates that the pre-convective environment over much of the central United States was cloud free. This is important because VAS-derived temperature and moisture soundings can only be obtained during clear conditions.

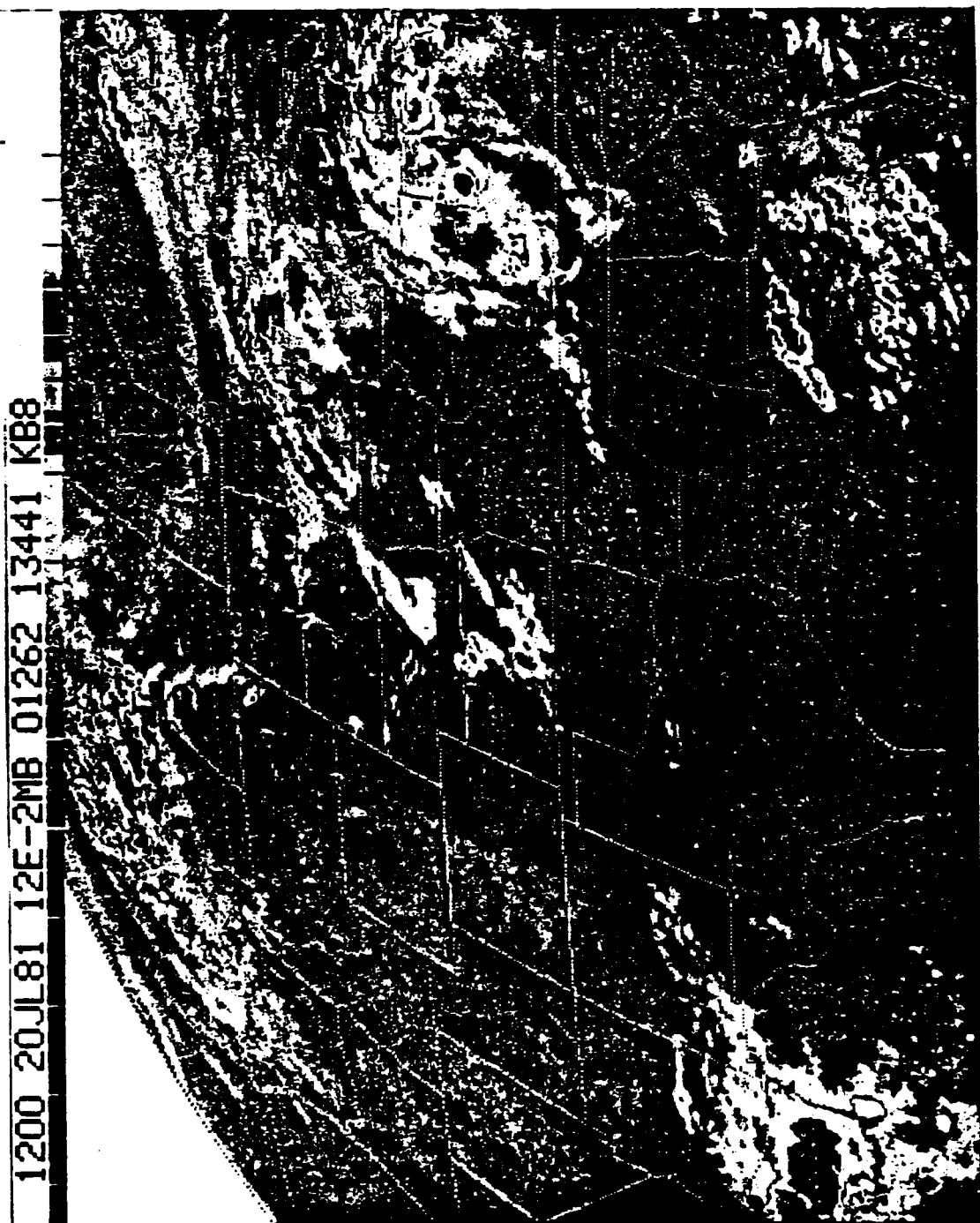
3.1 Surface Features

Figures 3.2a, 3.2b, and 3.2c are surface charts for 1200 GMT and 1800 GMT 20 July and 0000 GMT 21 July respectively. At 1200 GMT, a stationary front extended from a weak low pressure system over Michigan, westward to Colorado. This front separated warm, moist air over the south central states from cooler, drier air to the north. South of the front, surface winds were southerly and dewpoints reached 75°F in Missouri and Arkansas. Temperatures and dewpoints were

Figure 3.1 Sequence of infrared COES satellite images.

- a. 1200 GMT 20 July 1981
- b. 1800 GMT 20 July 1981
- c. 0000 GMT 21 July 1981

ORIGINAL PAGE IS
OF POOR QUALITY

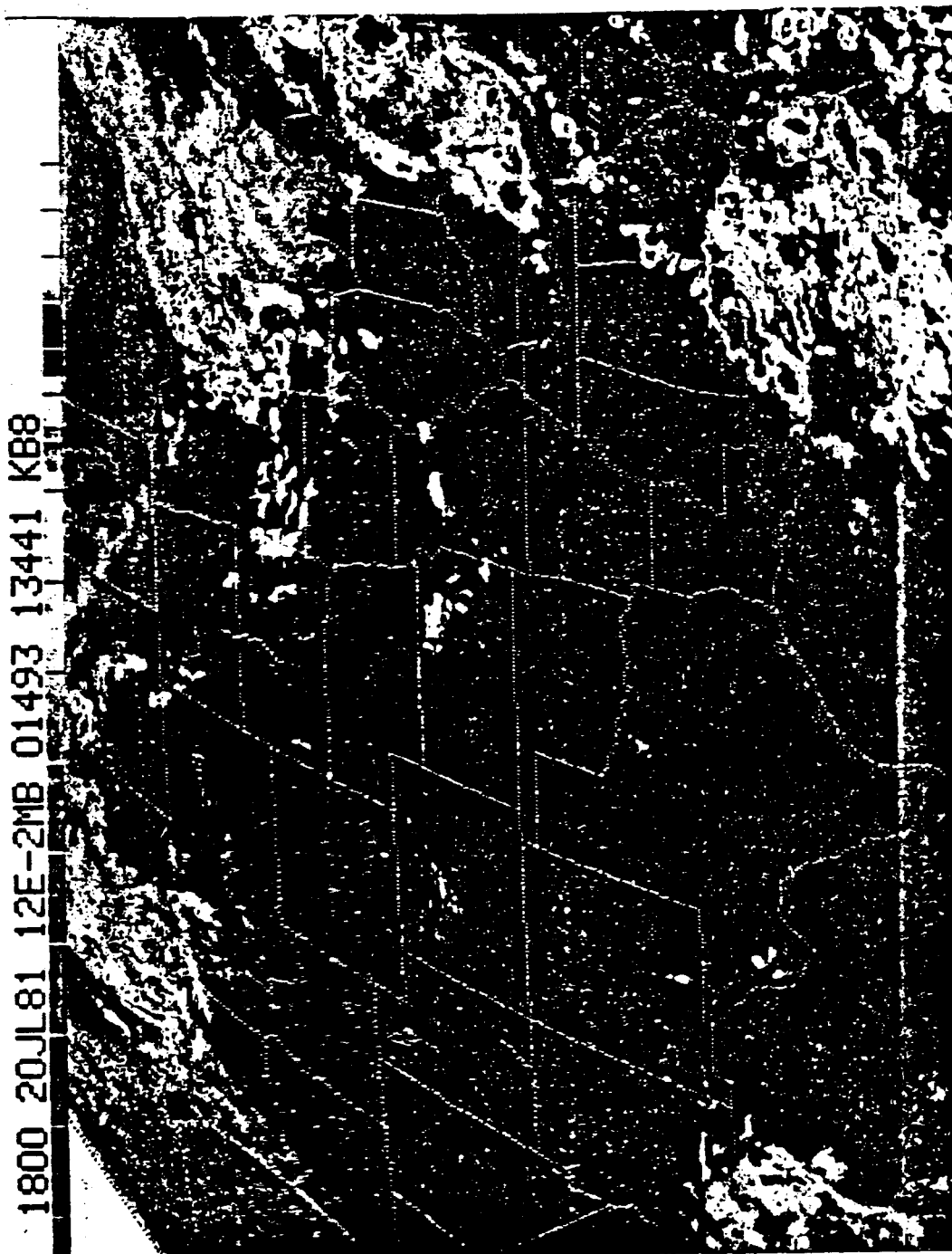


1200 20JL81 12E-2MB 01262 13441 KB8

(a)

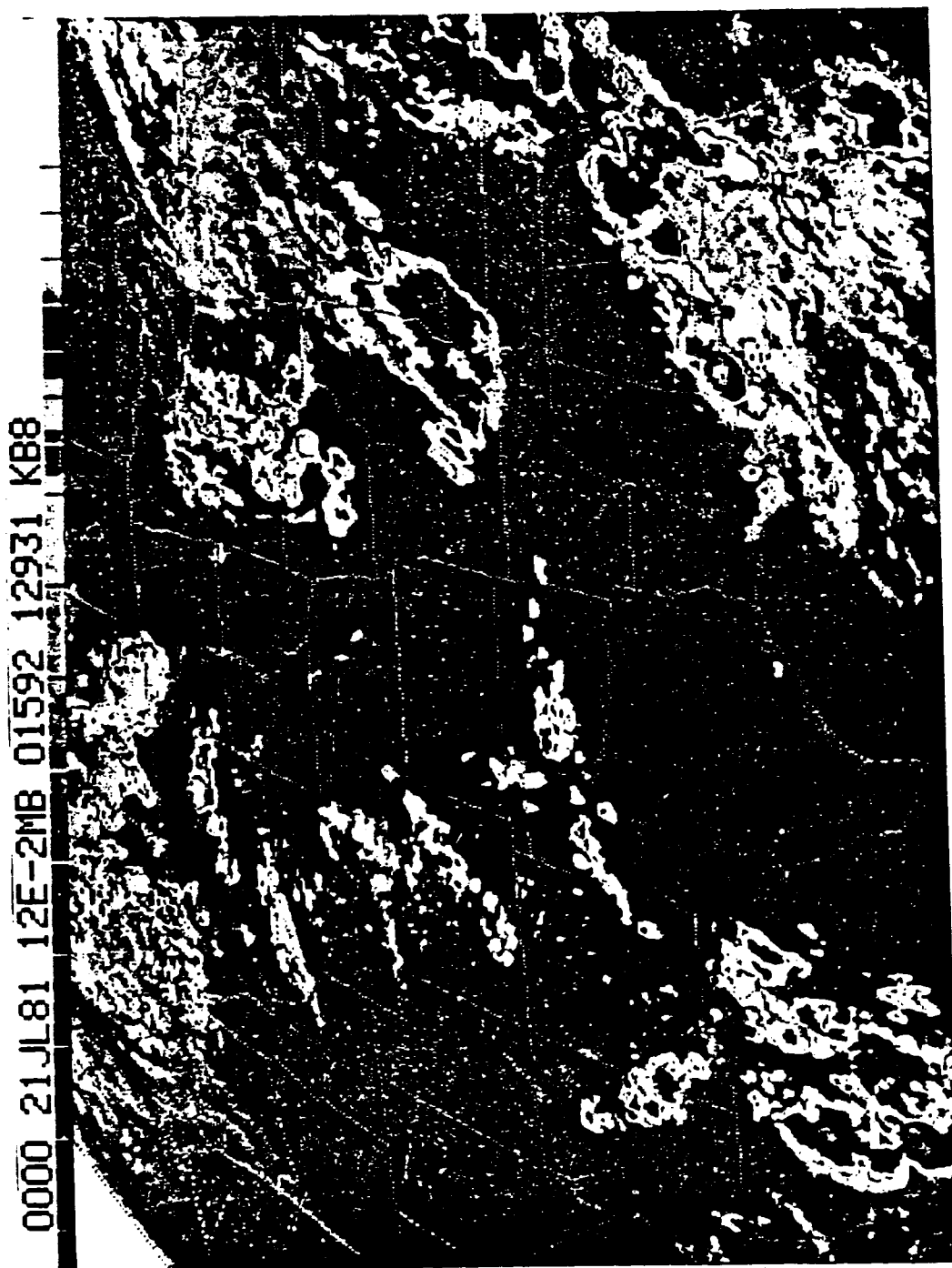
ORIGINAL PAGE IS
OF POOR QUALITY

1800 20JL81 12E-2MB 01493 13441 KB8

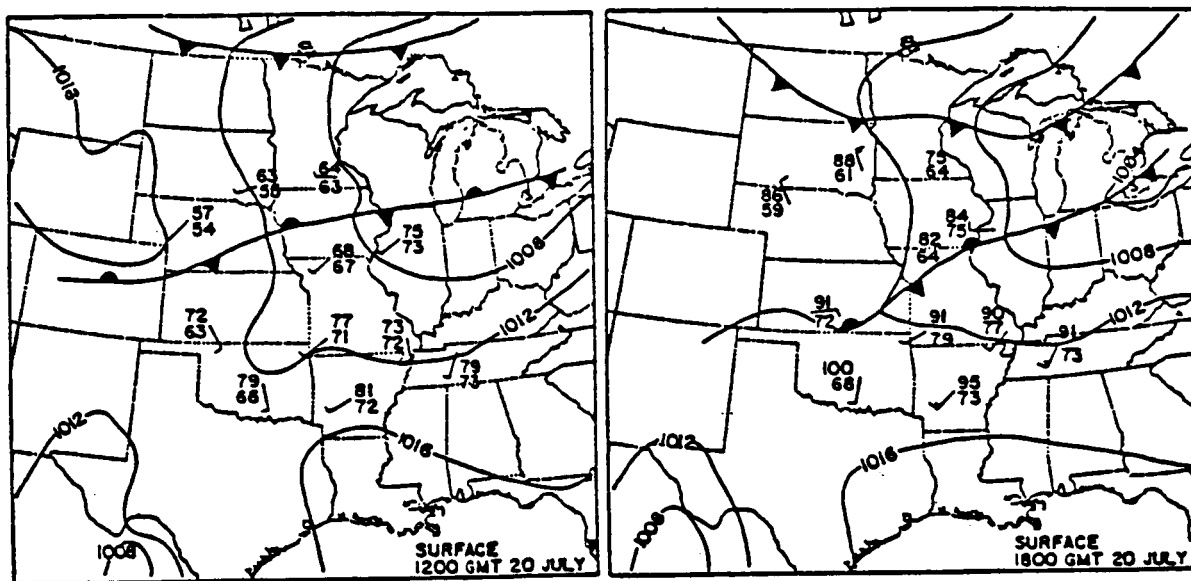


(b)

ORIGINAL PAGE IS
OF POOR QUALITY

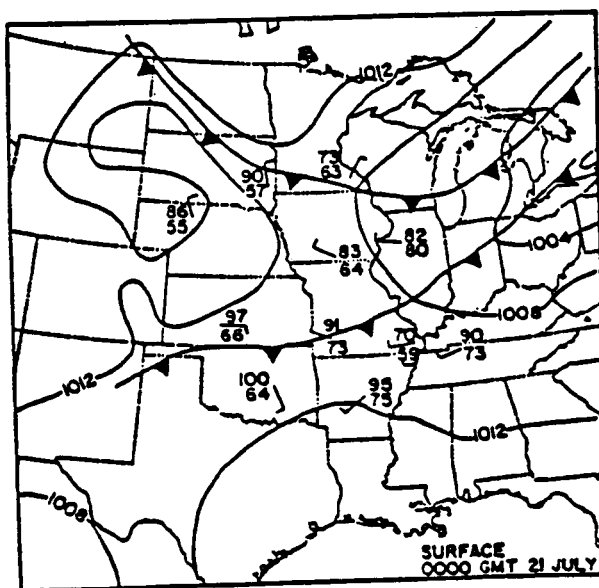


(c)



(a)

(b)



(c)

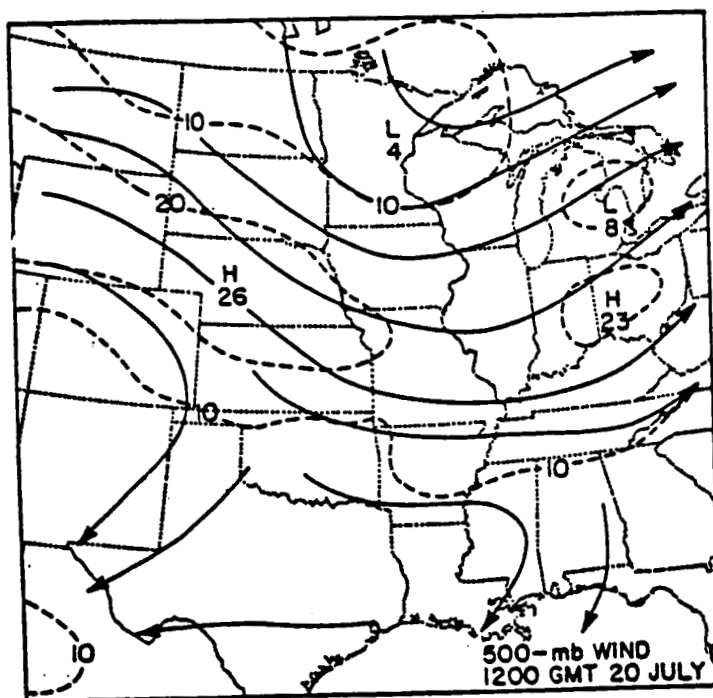
Figure 3.2 Sequence of surface charts.
 a. 1200 GMT 20 July 1981
 b. 1800 GMT 20 July 1981
 c. 0000 GMT 21 July 1981

significantly lower north of the front. By 1800 GMT, the front had drifted southward into Missouri and Kansas and surface wind confluence was apparent along the front from Missouri to Illinois. The initial stages of the large convective area that developed in eastern Missouri and southern Illinois are apparent in the 1800 GMT infrared imagery (Fig. 3.1b) just to the south of the front. By 0000 GMT 21 July, the front (now considered a cold front) had advanced into southern Missouri and Illinois. Infrared imagery from 0000 GMT (Fig. 3.1c) shows two convective systems aligned with the cold front: a line of cells through Oklahoma and a massive convective system over eastern Missouri, southern Illinois, and southern Indiana.

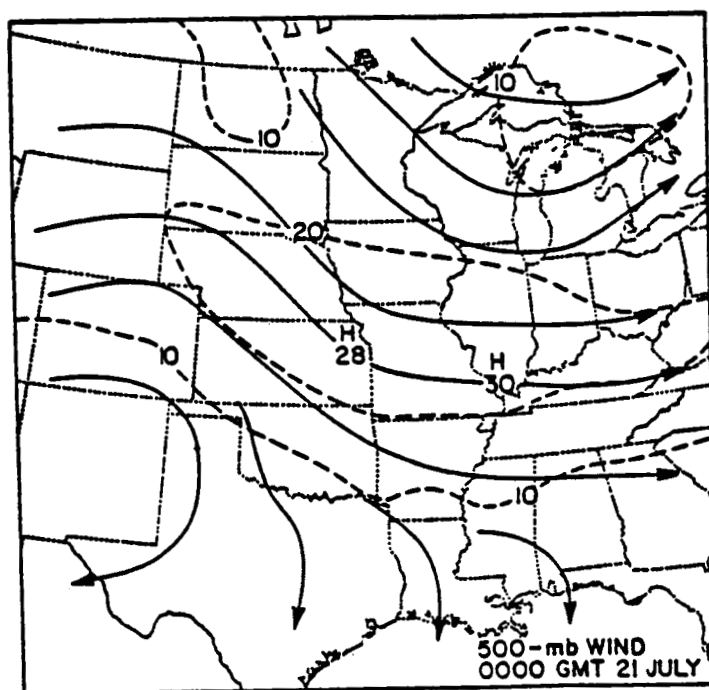
3.2 Upper Air Features

The 500-mb charts for 1200 GMT 20 July and 0000 GMT 21 July (Figs. 3.3a and 3.3b) indicate a short wave was moving toward the upper Mississippi Valley. Associated with this short wave was a region of significant cold-air advection which destabilized the atmosphere, contributing to the development of convection in Missouri. This region of cold-air advection was situated beneath an upper-level jet streak which propagated from eastern Nebraska to Illinois between 1200 GMT 20 July and 0000 GMT 21 July (Figs. 3.4a and 3.4b)

Two intrusions of dry air, indicated by analysis of 6.7 micron VAS imagery (Smith et al., 1982; Keyser, 1983; Petersen et al., 1983a), were possibly important factors associated with the outbreak of the two previously mentioned areas of convection. The first intrusion of dry air was associated with the strongest flow around a mid-level short



(a)

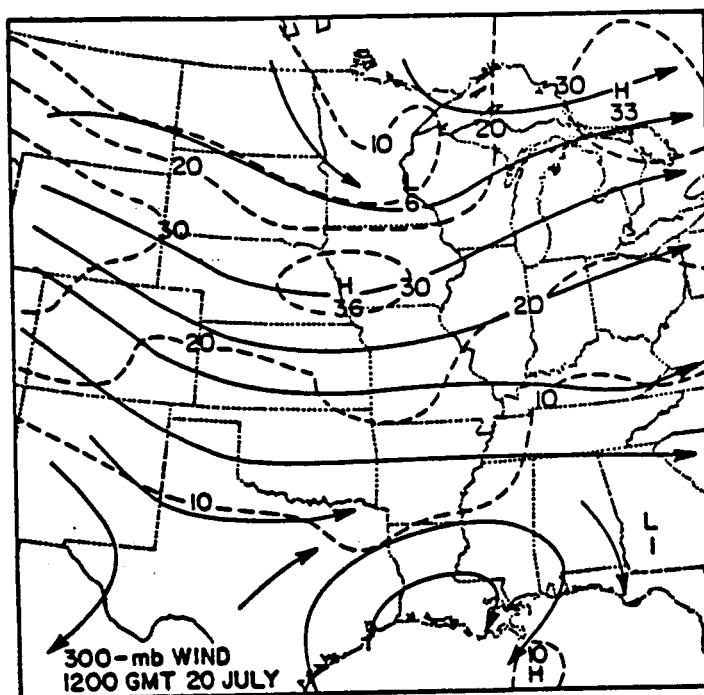


(b)

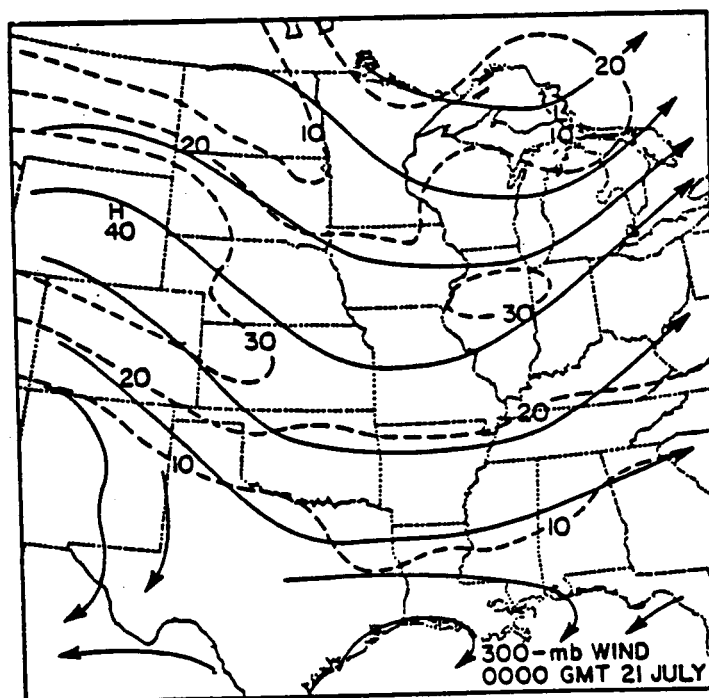
Figure 3.3 Streamline and isotach analysis of the 500-mb wind. The contour interval for wind speed is 10 ms^{-1} .

a. 1200 GMT 20 July 1981

b. 0000 GMT 21 July 1981



(a)



(b)

Figure 3.4 Streamline and isotach analysis of the 300-mb wind. The contour interval for wind speed is 10 ms^{-1} .
 a. 1200 GMT 20 July 1981
 b. 0000 GMT 21 July 1981

wave. At 1200 GMT this dry intrusion extended from Montana, through western South Dakota, Nebraska, northern Missouri and Iowa, and into southern Wisconsin. The southeastward movement of this pattern is evident in Figs. 3.5a-d, which have contours of derived upper-tropospheric relative humidity superimposed over imagery from the VAS 6.7 micron channel used in delineating mid-and upper-level moisture patterns (Smith et al., 1982). The large area of convection over eastern Missouri and Illinois is apparent in Fig. 3.5d. The second dry intrusion extends from the Texas/Oklahoma panhandle across Kansas and moved southeastward into central Oklahoma. It was probably associated with subsidence upstream at high levels, related to along-stream velocity convergence near 300 mb (Petersen et al., 1983a). These two mid- and upper-level dry intrusions led to a decrease in potential stability. Because values for potential stability ($\frac{\partial \theta}{\partial z}$) were never determined, it is uncertain whether these dry intrusions produced a potentially unstable environment, which would have been conducive to thunderstorm development in both Missouri and Oklahoma.

3.3 Description of Convective Systems

The massive thunderstorms over eastern Missouri and southern Illinois began when two smaller cells merged at approximately 2000 GMT 20 July. Radar composites for 2035 GMT 20 July and 0035 GMT 21 July (Figs. 3.6a and 3.6b) show this system developing and moving southeastward into southern Illinois. Figure 3.6b indicates that cloud-top heights reached 61,000 feet in Illinois for 0035 GMT 21 July. Four tornadoes, hail, and wind speeds up to 50 miles per hour were

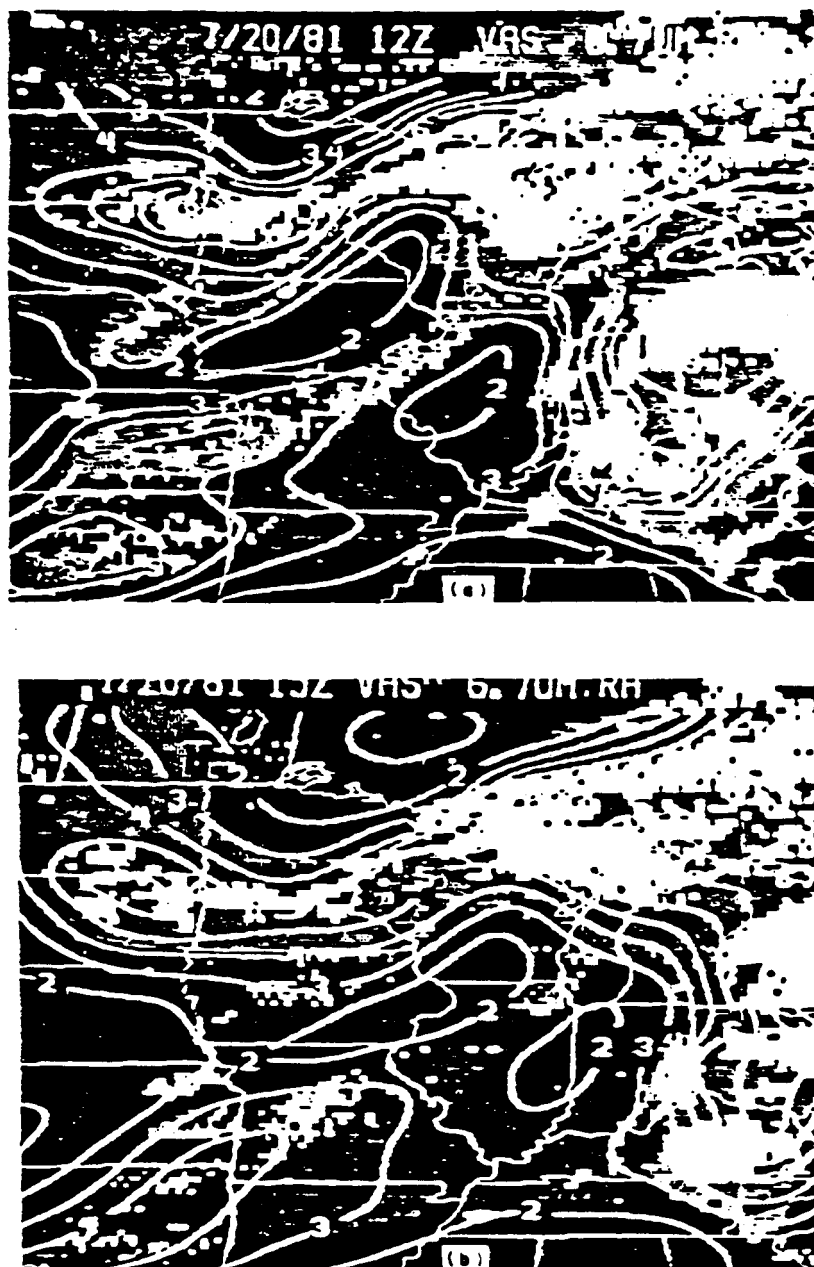


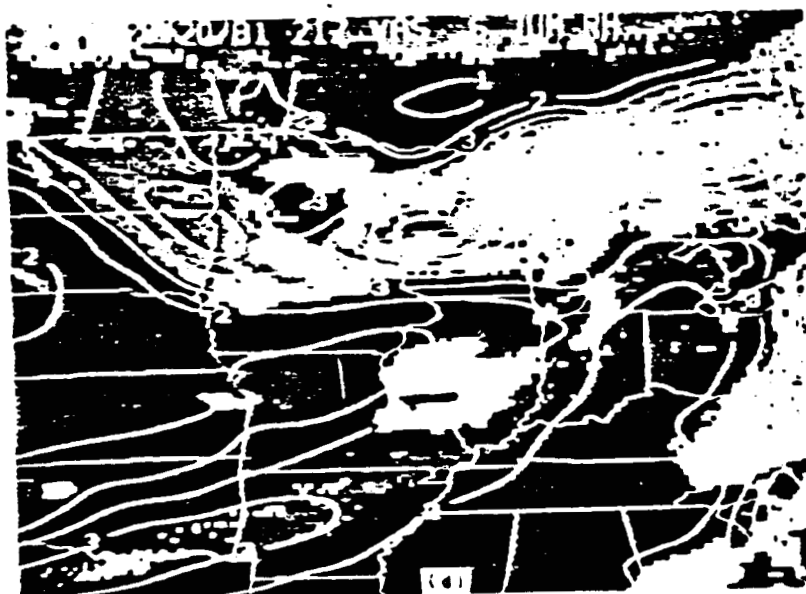
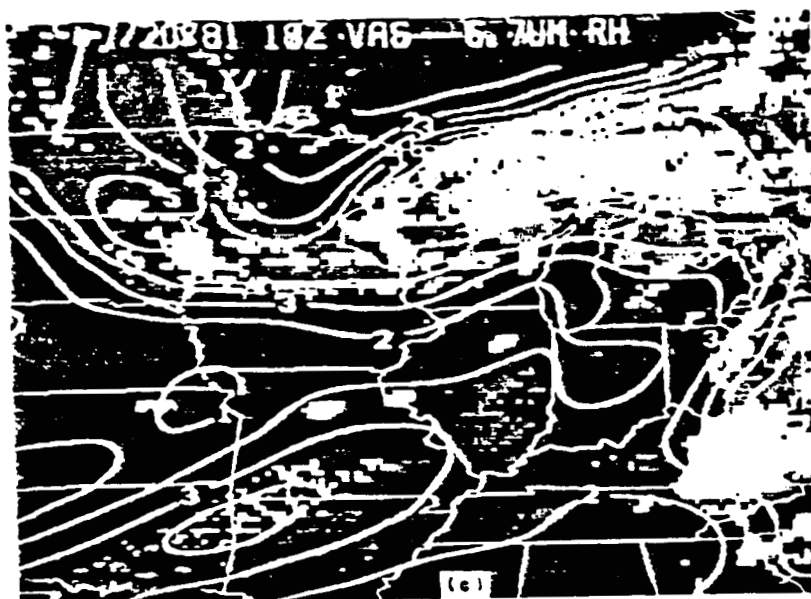
Figure 3.5 Sequence of upper tropospheric relative humidity (%/10) over the VAS image of 6.7- μ m atmospheric water vapor radiance emission (Smith, 1982).

- a. 1200 GMT 20 July 1981
- b. 1500 GMT 20 July 1981
- c. 1800 GMT 20 July 1981
- d. 2100 GMT 20 July 1981

ORIGINAL PAGE IS
OF POOR QUALITY

ORIGINAL PAGE IS
OF POOR QUALITY

29




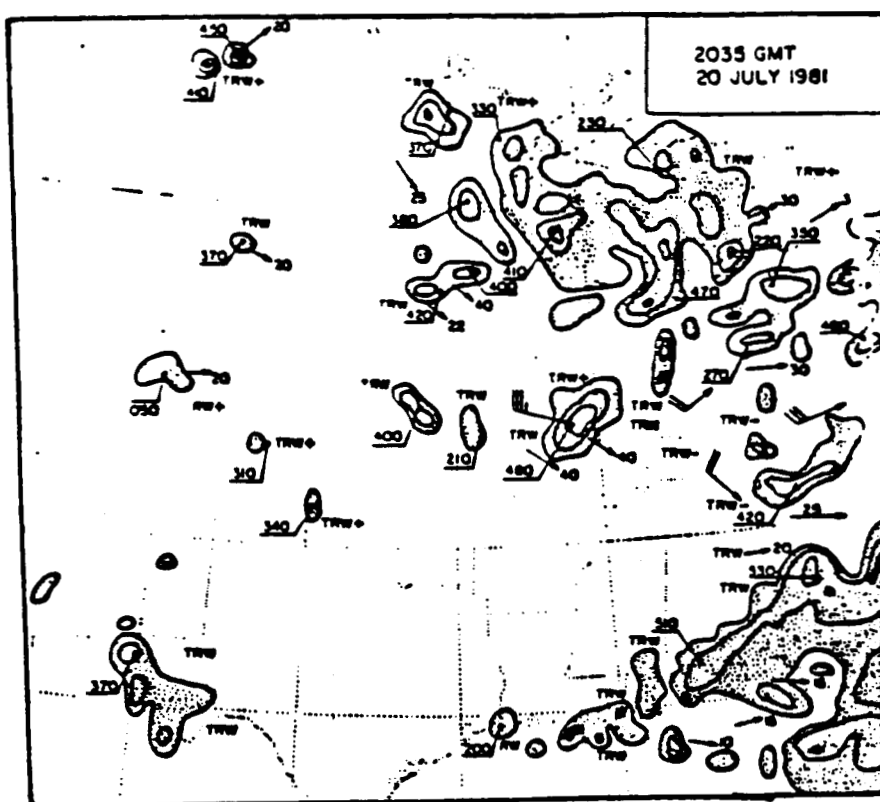
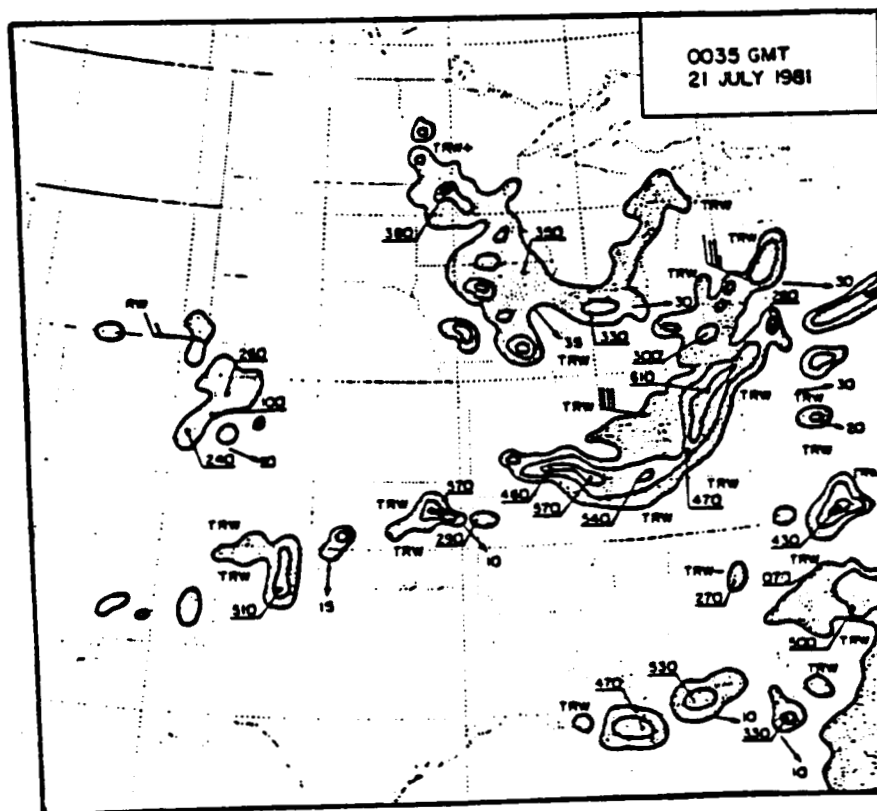


Figure 3.6 Radar composites.
a. 2035 GMT 20 July 1981
b. 0035 GMT 21 July 1981



(a)



(b)

observed in Missouri between 1900 GMT and 2100 GMT (Keyser, 1983). Recorded rainfall amounts for this area, between 1200 GMT and 0000 GMT, were as large as 0.8 inches (Fig. 3.7).

The radar composite for 0035 GMT 21 July (Fig. 3.6b) shows the fully developed line of convection that stretched from the Texas panhandle across Oklahoma into southern Missouri. Cloud top heights reached 57,000 feet in northeastern Oklahoma and southern Missouri. Only one rainfall observation (0.37 inches) was recorded for the period 1200 GMT to 0000 GMT in Oklahoma.

During this same period, there were several other distinct areas of thunderstorm activity within the VAS sounding network. A line of convection developed in northwest Illinois at approximately 1700 GMT and moved eastward across northern Illinois (Figs. 3.1b and 3.6a). Another convective system began in northwestern Iowa at 1900 GMT (Fig. 3.6a) and drifted into south-central Iowa by 0000 GMT (Figs. 3.1c and 3.6b) before weakening. Recorded precipitation from this storm reached 0.3 inches in central Iowa (Fig. 3.7). Finally, between 1700 GMT and 1800 GMT, another area of convection formed in north-central Kansas. It matured and moved eastward into northeastern Kansas (Figs. 3.1b and 3.6a) before dissipating shortly after 2200 GMT.

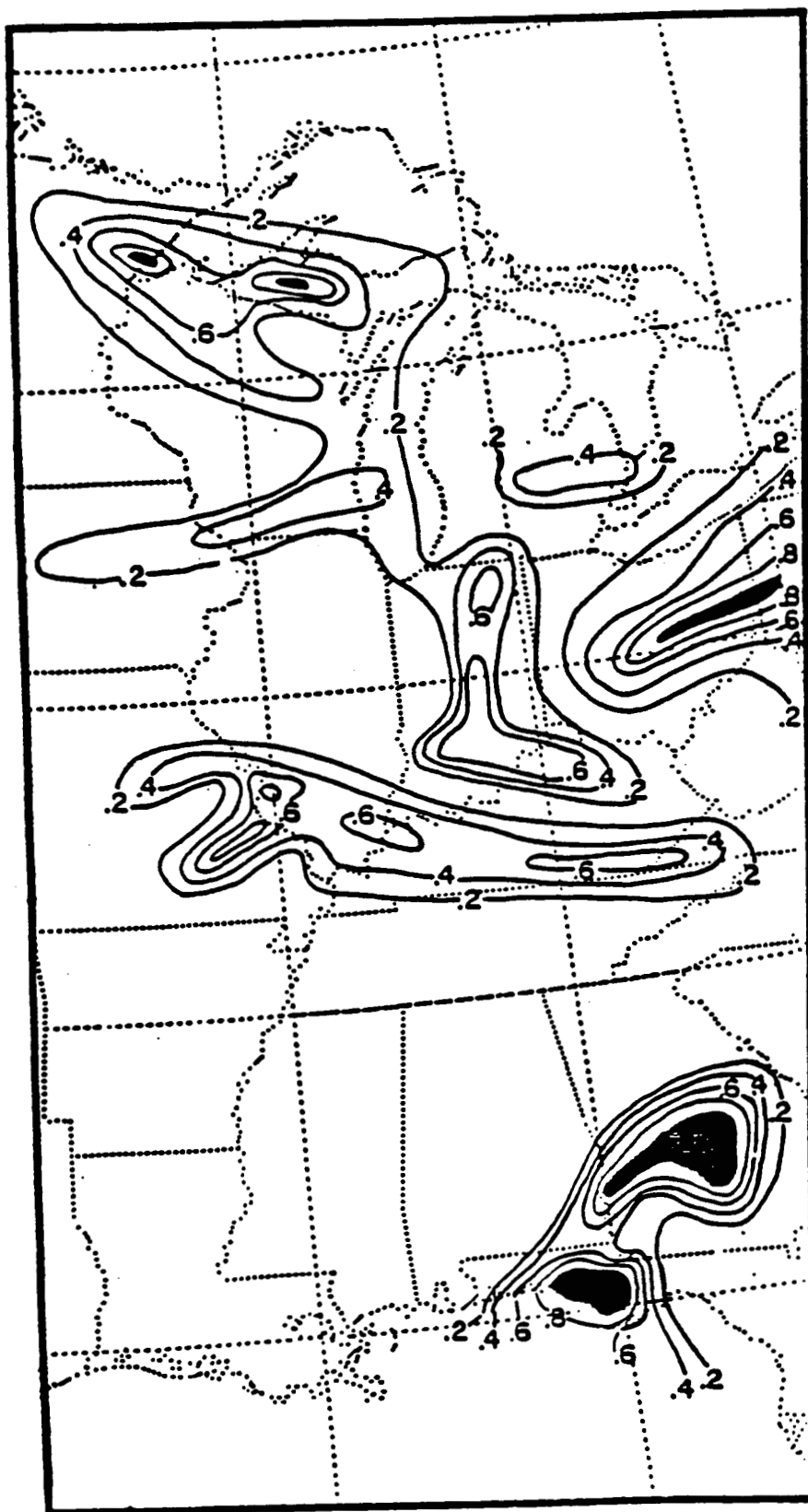


Figure 3.7 Cumulative precipitation amounts (inches) for the 12-h forecast period from 1200 GMT 20 July through 0000 GMT 21 July 1981. Shaded area have amounts greater than one inch.

4.0 ANALYSIS OF THE VAS DATA

VAS-derived temperature and moisture soundings and conventional radiosonde data, both available at 1200 GMT 20 July 1981 and 0000 GMT 21 July 1981 over the central United States, were used to enhance first-guess fields based upon National Meteorological Center (NMC) hemispheric octagonal grid data. These analyses served as the basis for the initial and boundary conditions of the model simulations. Figure 4.1 shows the analysis and computational domain for this research and the locations for the 1200 GMT VAS and radiosonde soundings. The high horizontal resolution of the VAS data in the central portion of the domain is clearly evident from this figure. Relatively large gaps in the distribution of the VAS data occur over parts of Nebraska and Kansas. These areas correspond to cloudy regions, apparent in the 1200 GMT infrared imagery (Fig. 3.1a).

4.1 A Review of the Objective Analysis Procedure Used With the PSU/NCAR Mesoscale Model

A successive-correction type of objective analysis procedure was used to analyze the radiosonde and VAS data. This type of objective analysis procedure, first developed by Cressman (1959), uses a series of successively smaller corrective scans around observation points to improve the grid point values of the first guess or previous analysis. In Cressman's objective analysis procedure, each observation has a circular area of influence with a distance-dependent weighting function ranging from 0.0 to 1.0. Corrections are based upon differences

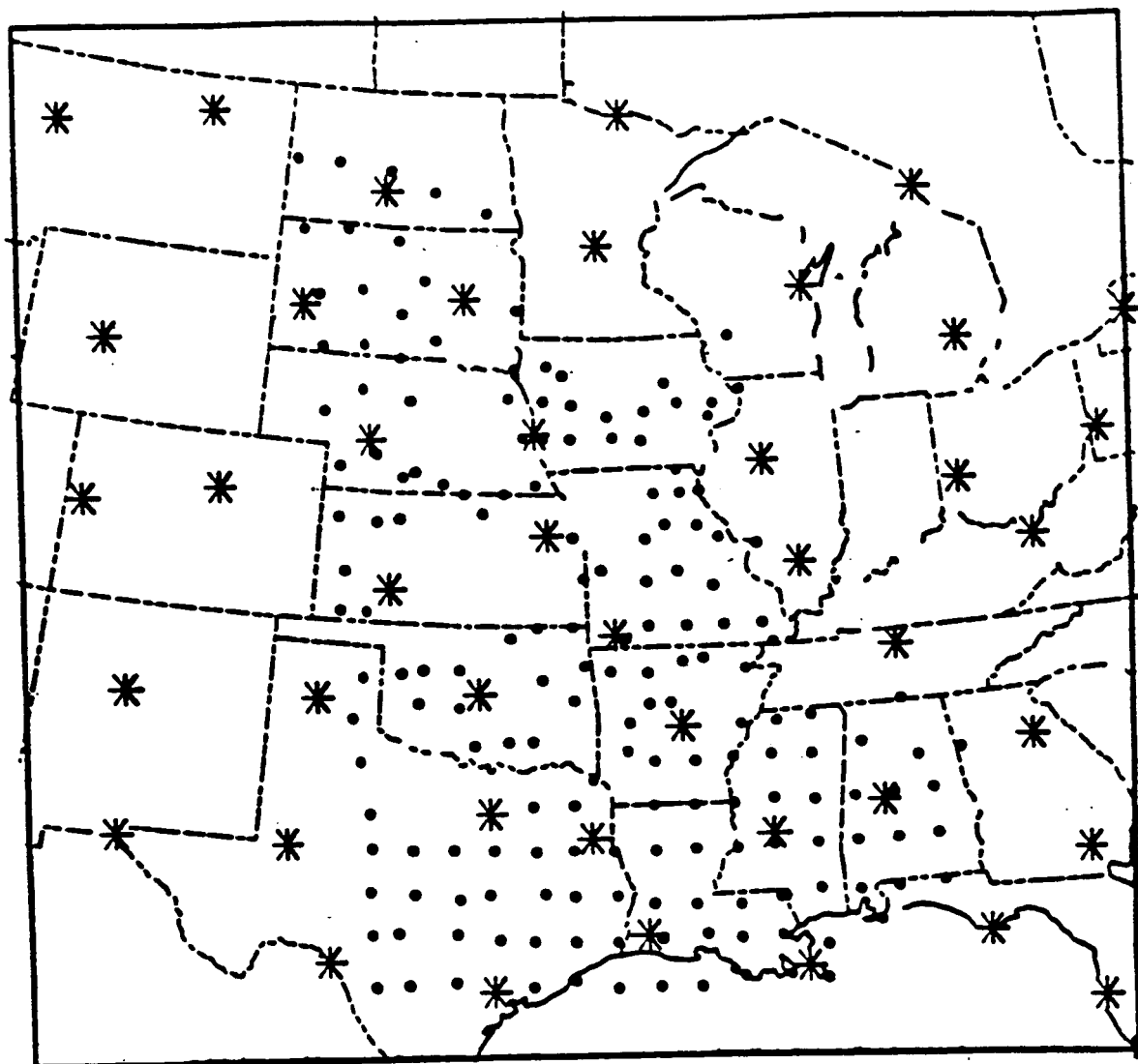


Figure 4.1 Analysis and computational domain for 20 July 1981 case. The locations for 1200 GMT radiosonde and VAS observations are indicated by asterisks and dots, respectively.

between the interpolated values of the first-guess field at the observation points and the observed values.

Under certain conditions, meteorological variables, particularly wind and moisture, exhibit a streaked pattern. This phenomenon is commonly accounted for in subjective analysis procedures. With this in mind, Inman (1970) applied an elliptical weighting function in an objective-analysis scheme. This improved analyses for straight flow but was found to be insufficient in areas of high wind speed and strong curvature (Anthes et al., 1982). For curved flow, a simple curved ellipse or a "banana-shaped" weighting function would be more appropriate. Benjamin and Seaman (1985) developed a "banana-shaped" weighting function for the objective analysis procedure that is used with the PSU/NCAR mesoscale model.

In the objective analysis procedure used in this study, the influence region surrounding an observation may have one of three possible shapes: circular, elliptical, or curved-elliptical. Because temperature fields seldom have this streaked pattern, only the circular weighting function is used to analyze temperature. A pressure-dependent critical wind speed is determined for each analysis level. The elliptical and "banana" weighting functions are only used for observations where the observed wind speed exceeds this critical value. If this criterion is met, then the streamline radius of curvature at the observation point determines whether the elliptical or the "banana" function is used. The "banana" function is required when the radius of curvature is less than three times the initial radius of influence about

the observation point. This initial radius of influence is 1.6 times the average spacing of the upper air stations (approximately 325 km for North America). The radius of influence is decreased by multiplying the previous scan radius by 0.7. In the analysis of conventional radiosonde data, four scans are made for all analyzed variables except relative humidity, which requires five scans. For a particular scan, only those grid points falling within the radius of influence may be corrected by the observed value.

In all of the objective analysis experiments used in this research, temperature, relative humidity, and the u and v components of the wind were analyzed at the surface and at all of the mandatory pressure levels from 850 to 100 mb. Additional analysis levels were selected at 980, 940, 900, 780, and 600 mb to improve the vertical resolution in the lower troposphere. Station observations of surface pressure were converted to sea-level pressure, which could then be objectively analyzed.

4.2 Incorporation of VAS-Derived Temperature and Moisture Data into the Objective Analysis

Three different procedures were developed to incorporate VAS-derived temperature and moisture data using this objective analysis technique. The first method made no distinction between VAS and radiosonde data. In the second procedure, the fine-scale gradient information provided by the VAS was retained, but the large-scale structure was adjusted so that the final analyses were more consistent with the radiosonde data. The third method included only temperature and moisture soundings from the VAS.

4.2.1 Equal Weighting of VAS and Radiosonde Data in the Objective Analysis

Several changes in the objective analysis procedure were made to incorporate VAS-derived temperature and moisture data. The addition of several, smaller scans about the observations was necessary to ensure that the inclusion of the VAS data would yield more mesoscale detail in the temperature and moisture fields. As in the larger scans, a multiplication factor of 0.7 was used to reduce the radius of influence between scans. It was determined that seven scans for both the temperature and moisture analyses would be sufficient. After the fourth scan in the temperature analysis, and after the fifth scan in the moisture analysis, radiosonde data were only used if VAS soundings fell within the same scan. Therefore, the final objective analysis only produced fine structure in areas where data were dense, without using inappropriately-small influence functions in regions where only radiosonde observations were available.

4.2.2 Unequal Treatment of VAS and Radiosonde Data in the Objective Analysis

When VAS and radiosonde data were treated equally, the final analyses of temperature and moisture were frequently inconsistent with radiosonde observations to a degree that was considered unacceptable. This was most apparent for low levels, where radiosonde temperature and mixing-ratio values differed by as much as 4°C and 3 g/kg from the final analyses. In areas where the VAS data were available, the VAS soundings dominated the analysis. Because the radiosonde data probably contain less bias error than the VAS data, a

second procedure was developed that allows the large-scale structure of the final analyses to be more consistent with radiosonde temperature and moisture values without eliminating smaller-scale features provided by the VAS. This procedure had two cycles. In the first cycle, VAS and radiosonde data were objectively analyzed in exactly the same manner as described in Section 4.2.1. A second cycle, used only for temperature and moisture, consisted of five corrective scans around radiosonde soundings. To ensure that only the large-scale structure was changed, the initial radius of influence (which is the largest) was used for all five scans.

4.2.3 Exclusion of Radiosonde Data in the Objective Analysis

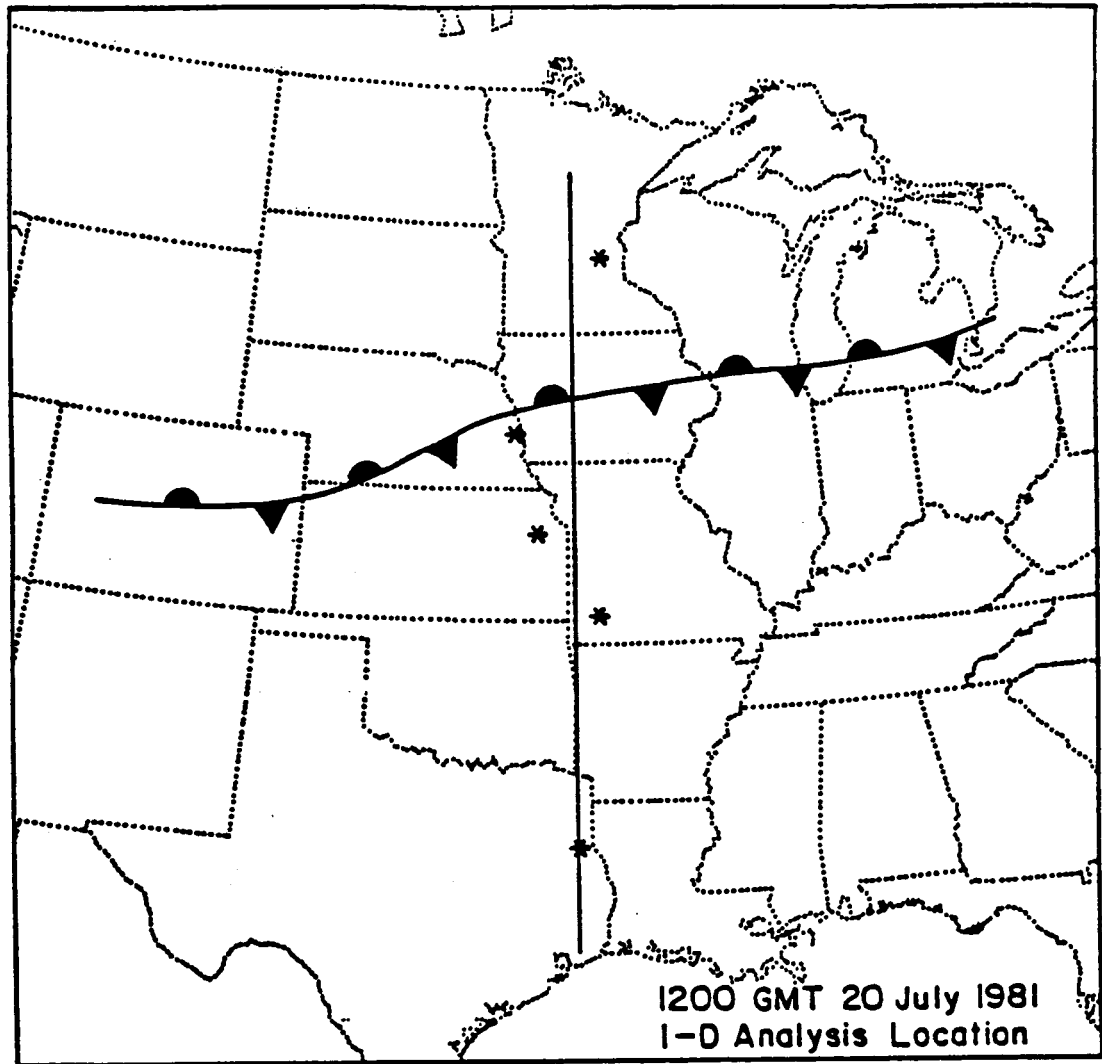
This objective-analysis procedure is like the one described in Section 4.2.1 except that all radiosonde data were excluded. As in the procedure described in Section 4.2.1, seven corrective scans were used and the radius of influence was reduced by a factor of 0.7 after each scan.

4.2.4 One-Dimensional Comparisons of Temperature and Moisture Analyses

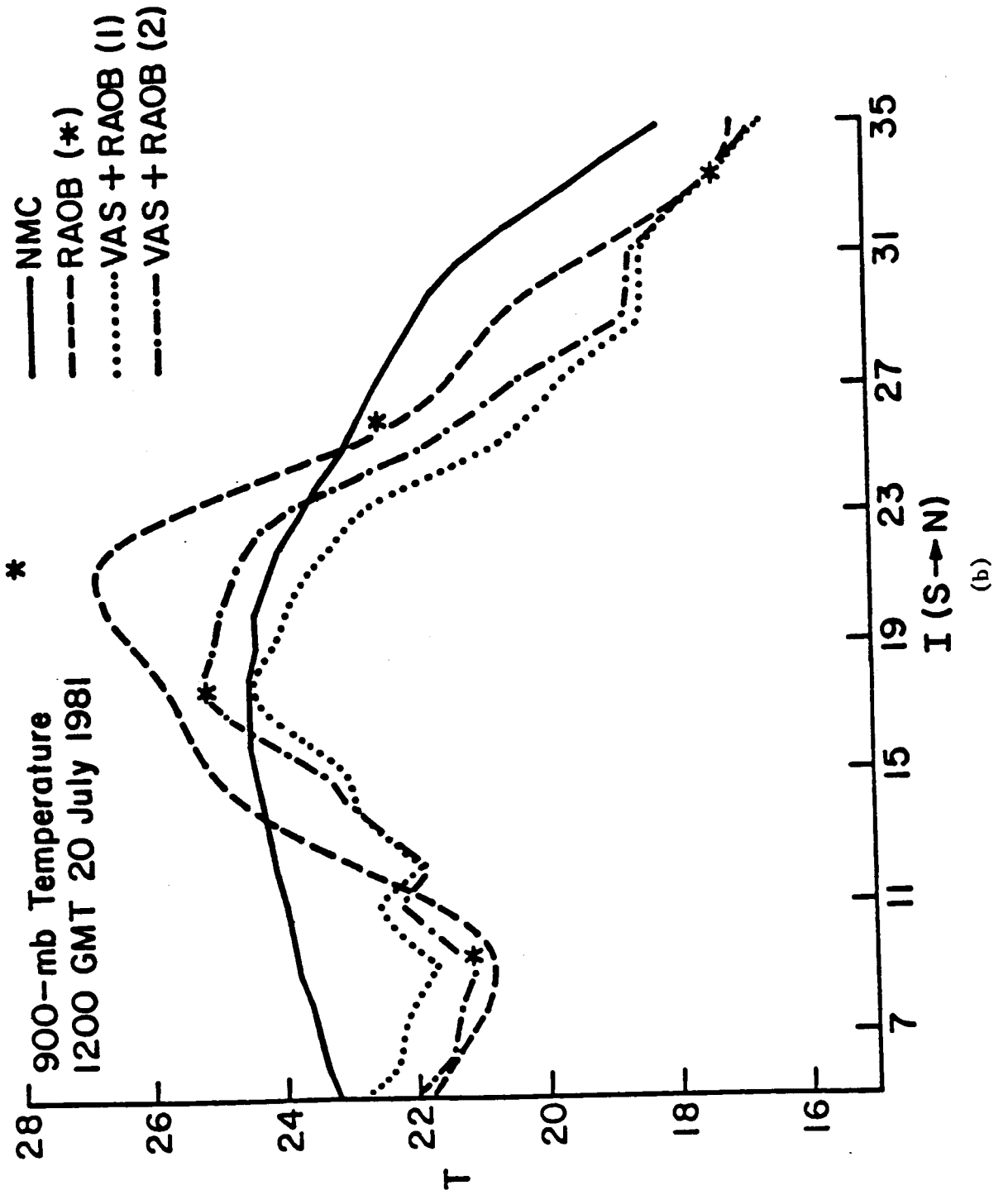
Several one-dimensional comparisons of the analyses of temperature and mixing ratio were made to compare the results from four of the different objective analysis procedures. These analyses were obtained by plotting temperature and mixing-ratio values from analysis pressure levels, along a north-south line (Fig. 4.2a). This line was chosen to pass close to several radiosonde observation sites (denoted by

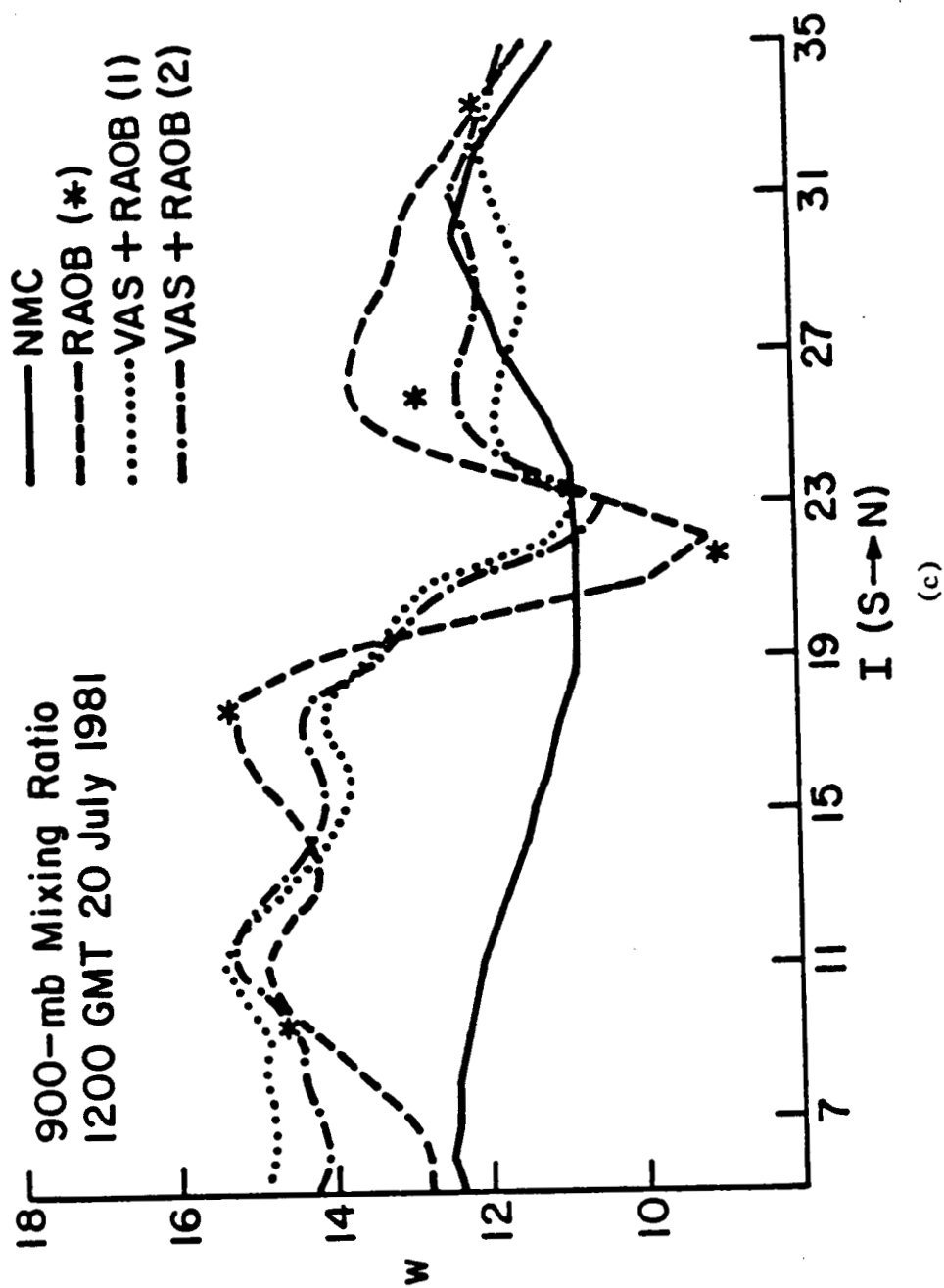
Figure 4.2 900-mb one-dimensional temperature and mixing-ratio analyses. There are four analyses. One is based on NMC global data only, one uses only radiosonde data, and two use a combination of radiosonde and VAS data as described in Sections 4.2.1 and 4.2.2. All analyses are valid for 1200 GMT 20 July 1981.

- a. Both the location of the stationary front for 1200 GMT 20 July 1981 and the north-south line used in the one-dimensional analyses are indicated. The asterisks denote radiosonde observations near the line.
- b. Temperature ($^{\circ}\text{C}$) analyses. The front is located near $I = 27$.
- c. Mixing-ratio (g/kg) analyses. The front is located near $I = 27$.



(a)





asterisks) and to cross the stationary front. Figures 4.2b and 4.2c show 900-mb analyses of temperature and mixing ratio for 1200 GMT 20 July based upon NMC global data (Analysis 1), radiosonde data (Analysis 2), and the two analyses that used both radiosonde and VAS data (Analysis 3 and Analysis 4).

The results of these one-dimensional analyses of temperature and mixing ratio are similar. For both variables, the relative lack of detail in Analysis 1 is readily apparent. Analysis 2, which uses only radiosonde data, agrees most closely with observed temperatures and mixing ratios from nearby radiosondes, and contains the greatest amplitude in the large-scale variance. Analyses of temperature and mixing ratio, using only VAS data (not shown), have less amplitude in the large-scale variance than do all the analyses except Analysis 1. In Analysis 3, several small-scale features are apparent, but analyzed temperatures and mixing ratios differ markedly from radiosonde values in some cases because of a bias that has been introduced. Analysis 4 of temperature and mixing ratio is much like Analysis 3 but is somewhat more consistent with radiosonde values. The location and strength of the temperature gradient associated with the stationary front are similar for all of the temperature analyses except for Analysis 1.

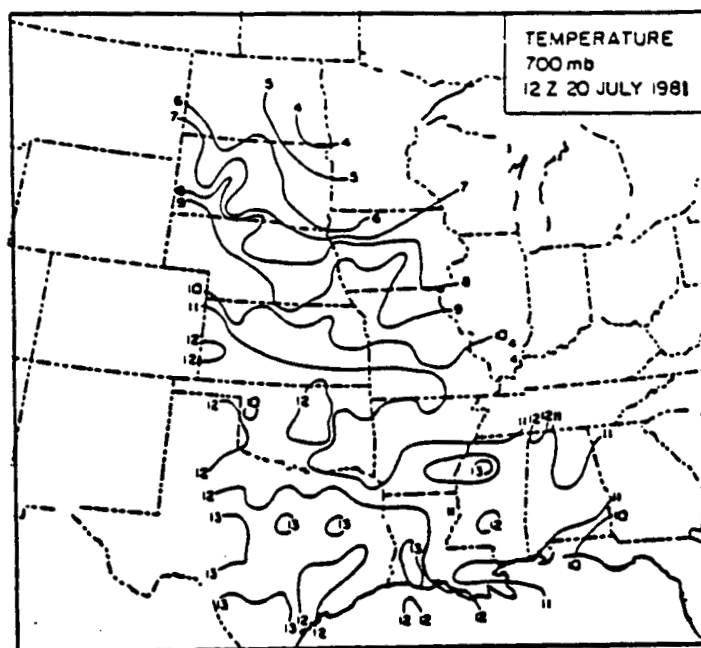
4.3 Comparison of Objective and Subjective Analyses, Based Upon VAS-Derived Temperature and Moisture Data

Several levels of temperature and mixing-ratio data, precipitable water, and several stability indices, all derived only from VAS measurements and valid for 1200 GMT 20 July 1981, were plotted and subjectively analyzed. In these subjective analyses, little attempt was made to smooth the data. The subjective temperature and

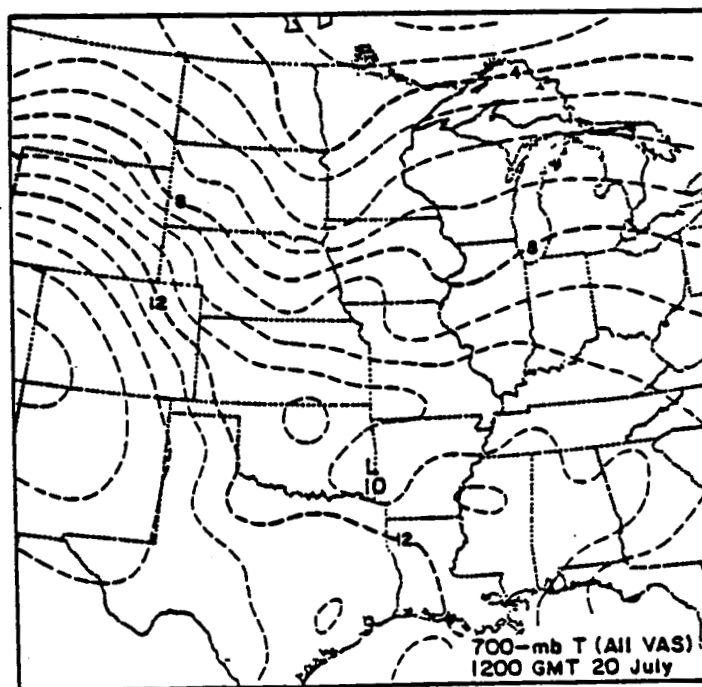
mixing-ratio analyses were then compared with objective analyses of these same variables for several levels. These objective analyses were based upon radiosonde data only, VAS data only, and a combination of these two data sources. As expected, the objective analyses that used only VAS data were the most consistent with the subjective analyses. Comparison of the objective and subjective analyses of VAS data, in the VAS-data-rich region, gives some indication of how well these data are being incorporated by the objective analysis procedure.

Subjective and objective analyses of VAS-derived temperatures are shown in Figs. 4.3a and 4.3b (700 mb) and in Figs. 4.4a and 4.4b (500 mb). There is a very good agreement between the subjective and objective analyses of 700-mb temperature. The most noticeable difference between these analyses is the relative smoothness of the isotherms in the objective analysis. At 500 mb, the subjective and objective analyses are also quite consistent. There is less difference between the two analyses with respect to the smoothness of the isotherms than there is at 700 mb. Two tongues of warm air, one over eastern Missouri and the other near southeastern Louisiana are very similar in the two analyses.

The subjective and objective analyses of VAS-derived mixing ratios are shown in Figs. 4.5a and 4.5b (700 mb) and in Figs. 4.6a and 4.6b (500 mb). For both levels (700 and 500 mb), the subjective analyses of VAS-derived mixing ratio contain more small-scale detail than do the objective analyses of the same data. This is consistent with the comparison of the analyses using VAS-derived temperatures. Comparison of the two 700-mb analyses of mixing ratio indicates two areas of



(a)

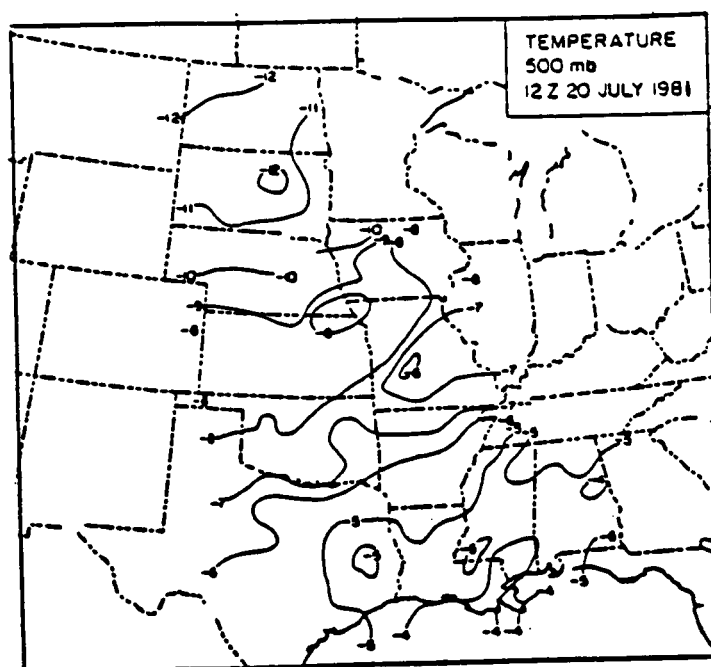


(b)

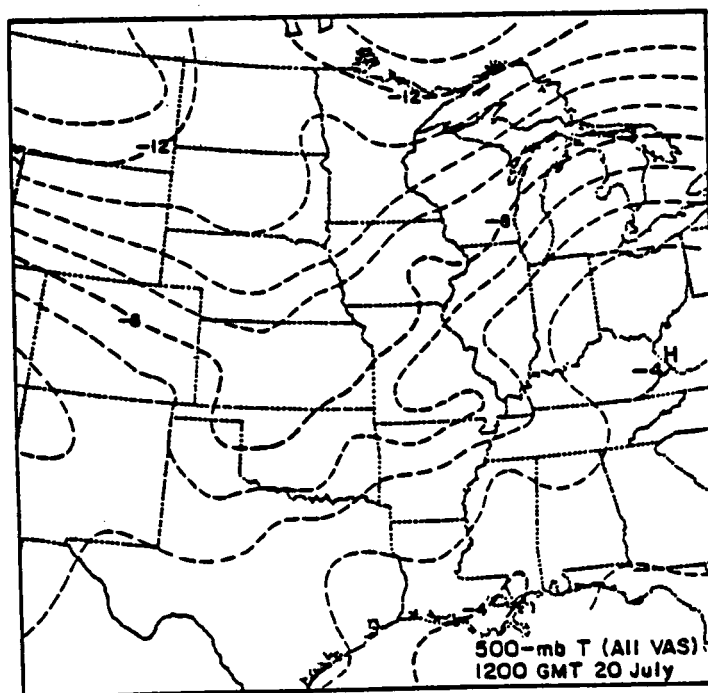
Figure 4.3 Subjective and objective 700-mb temperature analyses based on VAS data, for 1200 GMT 20 July 1981. The contour interval is 1°C.

a. Subjective analysis

b. Objective analysis



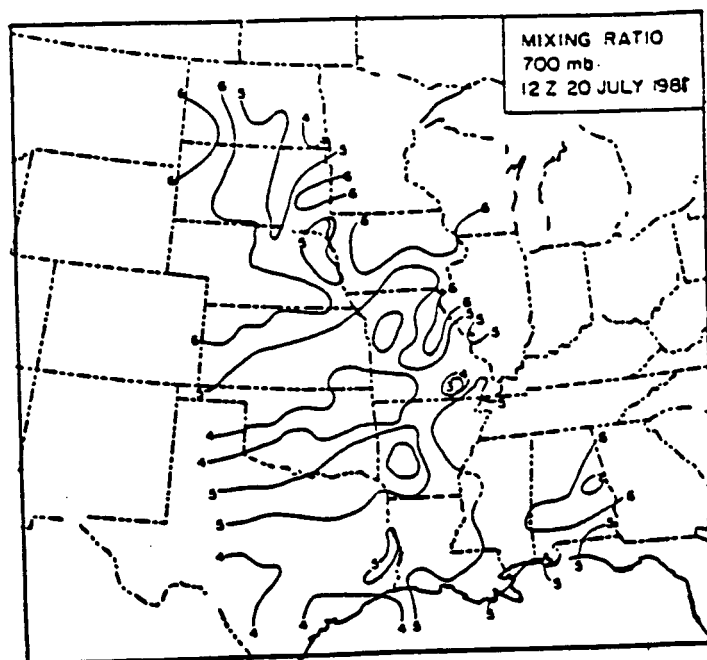
(a)



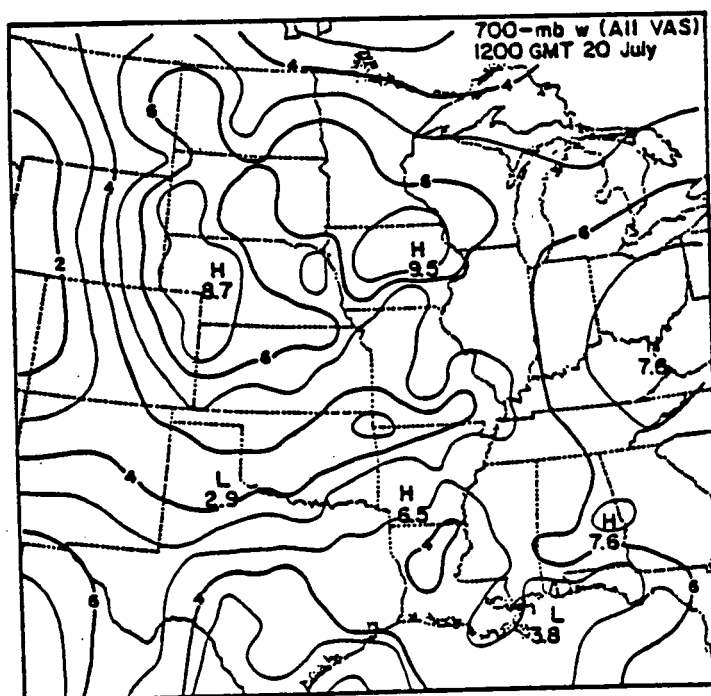
(b)

Figure 4.4 Subjective and objective 500-mb temperature analyses based on VAS data, for 1200 GMT 20 July 1981. The contour interval is 1°C.

- a. Subjective analysis
- b. Objective analysis



(a)



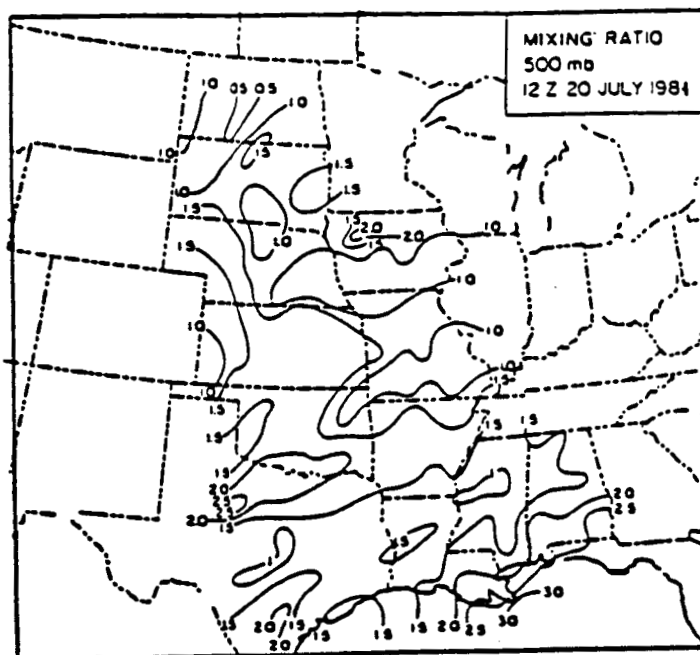
(b)

Figure 4.5 Subjective and objective 700-mb mixing ratio analysis based on VAS data, for 1200 GMT 20 July 1981. The contour interval is 1 g/kg.

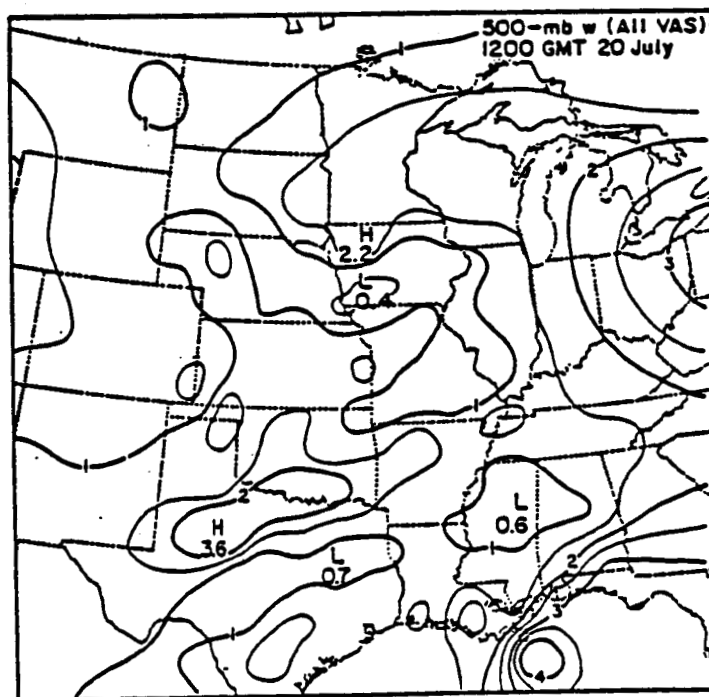
a. Subjective analysis

b. Objective analysis

ORIGINAL FILED
OF POOR QUALITY



(a)



(b)

Figure 4.6 Subjective and objective 500-mb mixing-ratio analyses based no VAS data, for 1200 GMT 20 July 1981. The contour interval is 0.5 g/kg.
a. Subjective analysis
b. Objective analysis

significant disagreement but also many features common to both analyses. Significant moisture maxima over western Nebraska and eastern Iowa are present in the objective analysis but not in the subjective analysis. The reason for this discrepancy is that for both places a relatively high VAS moisture value was excluded from the subjective analysis but not the objective analysis. Three moist tongues are apparent in both analyses. These are located over eastern Missouri, northern Texas and southwestern Arkansas, and over Alabama. In both analyses, a dry tongue of air, stretching across Oklahoma and into southwestern Missouri, is evident. The subjective and objective 500-mb analyses of VAS-derived mixing ratios are also in very close agreement.

4.4 Comparison of the Objective Analyses

In order to determine what impact the addition of VAS data might have on a numerical forecast, it was necessary to compare the temperature and moisture analyses, both with (VAS analysis) and without (NOVAS analysis) VAS data, in terms of how well the analyses defined the synoptic conditions which led to the outbreak of convection during the forecast period. The discussion of this comparison utilizes VAS and NOVAS temperature and mixing-ratio analyses from the lower, middle, and upper troposphere. Also included are cross-sections of potential temperature and mixing ratio, taken through the stationary front for 1200 GMT 20 July. Finally, there is a comparison between VAS and NOVAS stability for a particular layer.

Figures 4.7a and 4.7b are NOVAS and VAS 900-mb temperature analyses. In many respects the two analyses are alike. One prominent

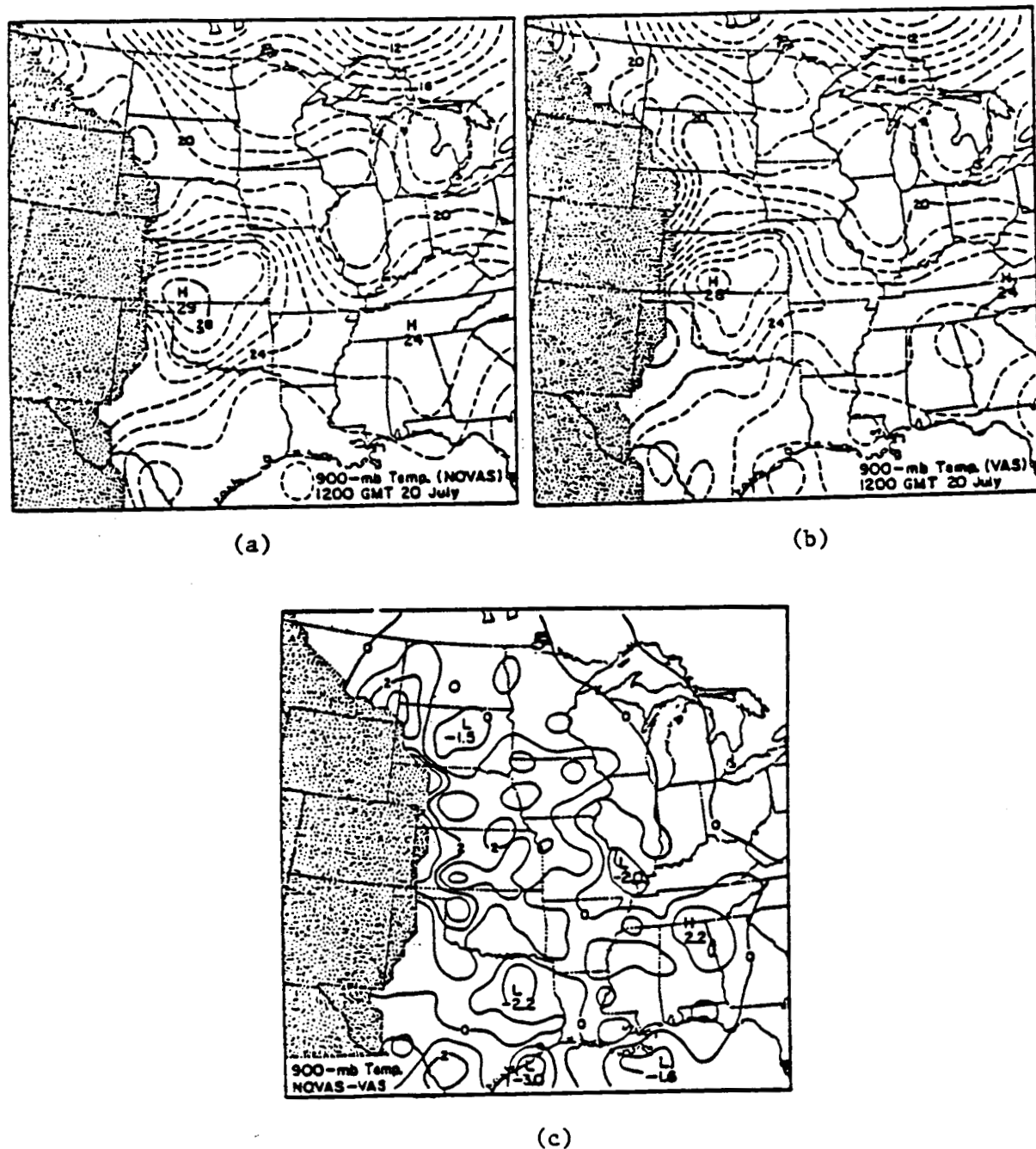


Figure 4.7 NOVAS and VAS 900-mb temperature analyses for 1200 GMT 20 July 1981. The stippled area represents the region where surface pressure is less than 900 mb. The contour interval is 1°C.

- a. NOVAS analysis
- b. VAS analysis
- c. Differences between NOVAS and VAS (NOVAS-VAS) analyses. Positive differences indicate lower VAS temperatures.

feature, common to both, is a tongue of warm air extending from Texas through Oklahoma and into Kansas. The highest temperatures are similarly located in southern Kansas, although this maximum is about 1°C lower in the VAS analysis. A baroclinic zone is indicated by both analyses in the vicinity of the stationary front. Northern Iowa and southern Minnesota are cooler in the VAS analysis, which leads to a slightly stronger temperature gradient through Iowa. The VAS analysis provides a weaker gradient across Missouri. Figure 4.7c shows the 900-mb temperature difference between the NOVAS and VAS analyses. Throughout much of the domain, temperatures are slightly cooler in the VAS analysis. Warming effects from higher VAS temperatures are more localized.

The NOVAS and VAS 500-mb temperature analyses (Figs. 4.8a and 4.8b, respectively) are much alike in that gradients are similarly oriented and of comparable strength. In addition, over most of the domain, local temperature differences are less than 1°C (Fig. 4.8c). Because cold-air advection in the middle troposphere is a possible factor in the evolution of the convection over Missouri, streamlines have been added to Figs. 4.8a and 4.8b to facilitate comparison of thermal advection. Both the NOVAS and VAS analyses indicate cold-air advection over much of the central United States; however, in the VAS analysis there appears to be weaker cold-air advection over Iowa, eastern Kansas, and Missouri.

A baroclinic zone, extending from the central Rockies to eastern Canada, is evident in both the NOVAS and VAS 300-mb temperature analyses (Figs. 4.9a and 4.9b, respectively). The gradient in the VAS

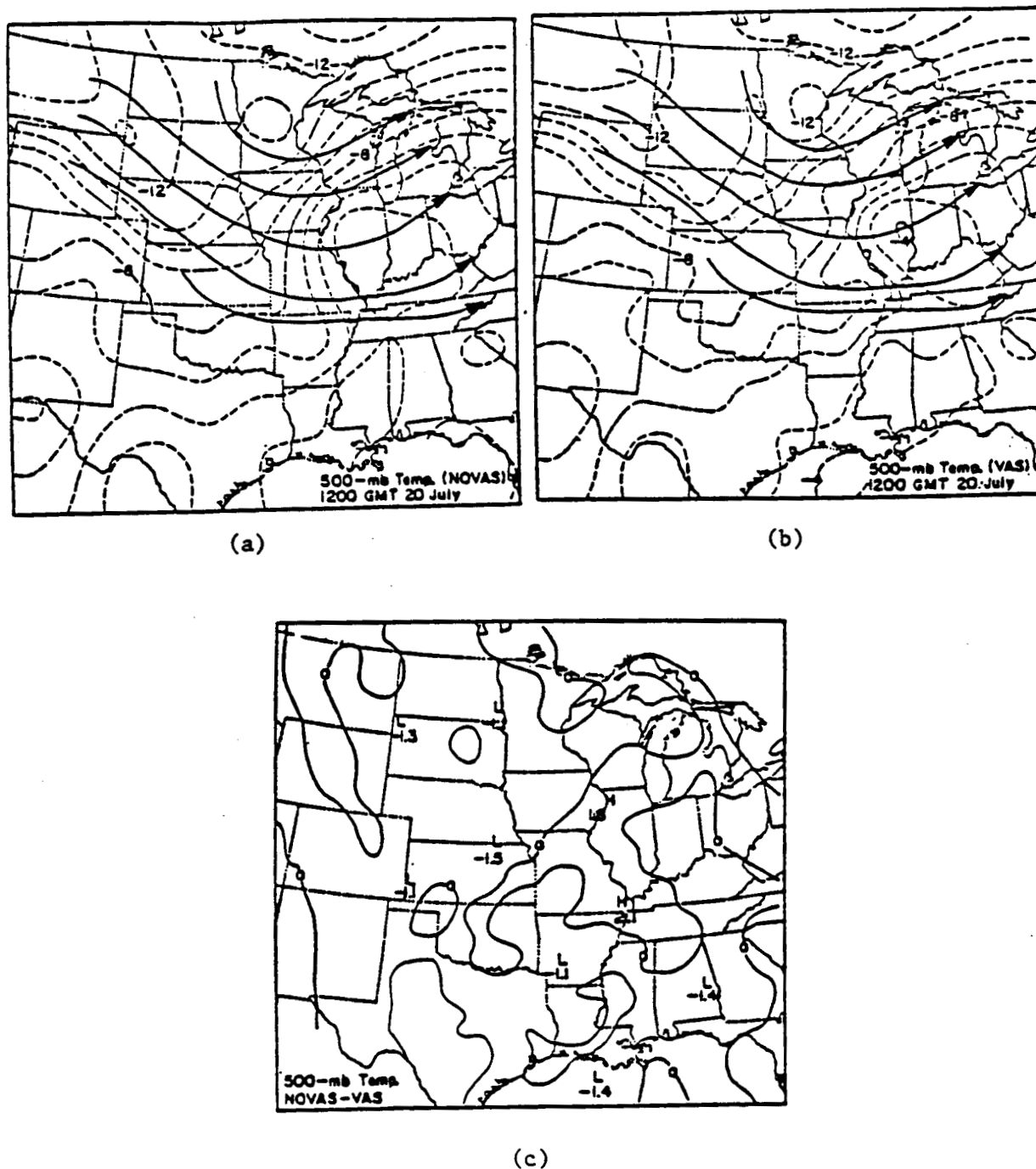


Figure 4.8 NOVAS and VAS 500-mb temperature analyses for 1200 GMT 20 July 1981. The contour interval is 1°C.

- NOVAS analysis. A streamline analysis is included to facilitate comparison of thermal advection patterns.
- VAS analysis. A streamline analysis is included to facilitate comparison of thermal advection patterns.
- Differences between NOVAS and VAS (NOVAS-VAS) analyses. Positive differences indicate lower VAS temperatures.

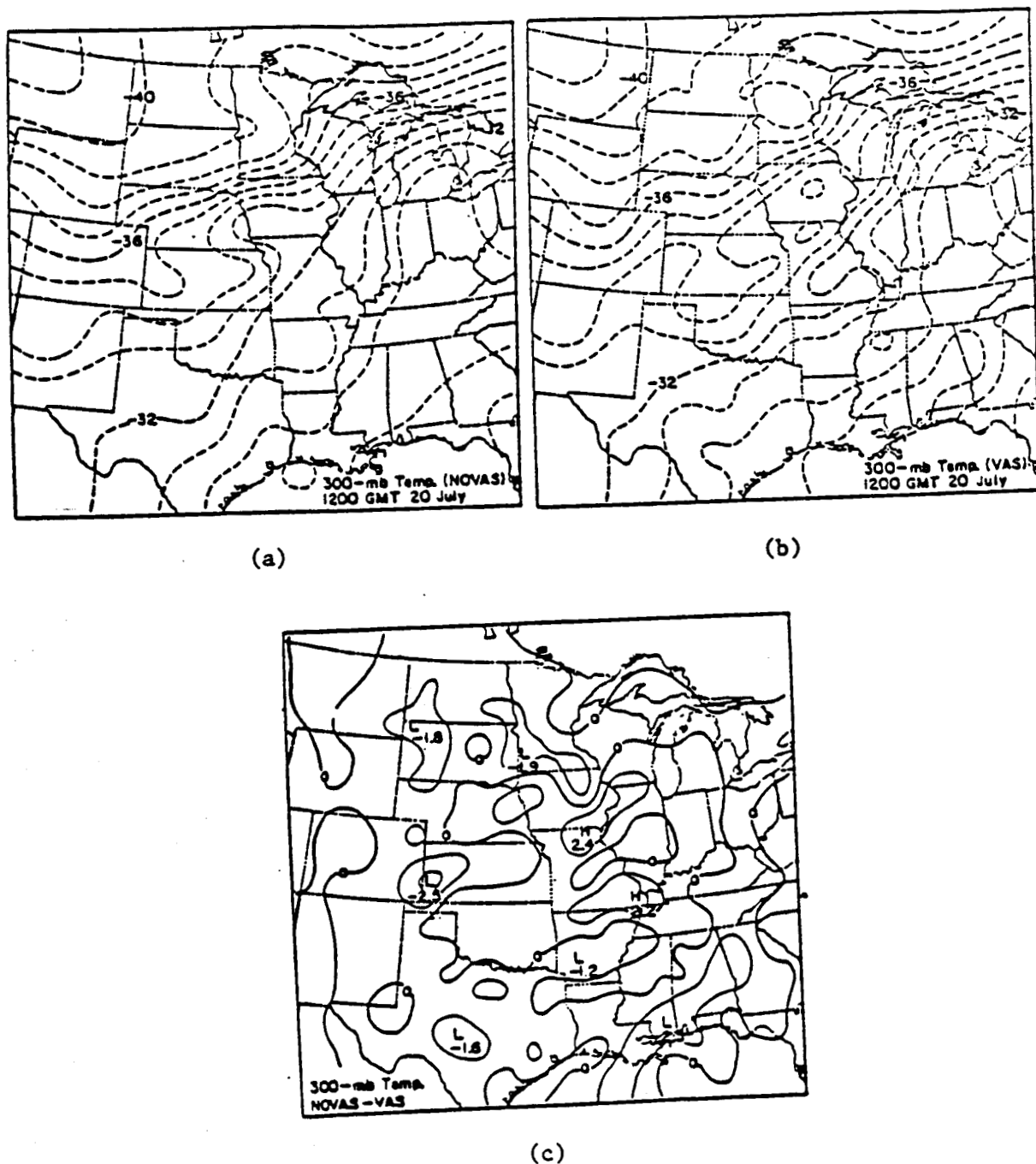


Figure 4.9 NOVAS and VAS 300-mb temperature analyses for 1200 GMT 20 July 1981. The contour interval is 1°C .

- a. NOVAS analysis.
- b. VAS analysis.
- c. Differences between NOVAS and VAS (NOVAS-VAS) analyses. Positive differences indicate lower VAS temperatures.

analysis is weaker throughout much of this zone. A thermal wave pattern is evident in the VAS analysis over Nebraska and South Dakota but is missing in the NOVAS analysis. A wave over Kansas, southern Nebraska, and Iowa, is much more pronounced in the NOVAS analysis than in the VAS analysis. This pattern may be attributed to the radiosonde observation from Omaha, Nebraska. The nearby VAS-derived temperatures differ from this radiosonde temperature by nearly 3°C and they cause smoothing of the analysis in this vicinity. Figure 4.9c indicates that over the central portion of the domain, from Oklahoma to Michigan, the VAS analysis is cooler, especially in northern and southeastern Missouri. Several isolated areas of VAS warming are also apparent in South Dakota, western Kansas, Texas, Arkansas, and southern Mississippi.

Shown in Figs. 4.10a and 4.10b are the NOVAS and VAS mixing-ratio analyses for the 850-mb level. Although the overall moisture pattern is very similar in both analyses, significant local differences in mixing ratio are apparent in Fig. 4.10c. The addition of VAS moisture data yields higher moisture values from Kansas to southeastern Montana. In the eastern part of the VAS-data region, from the Gulf of Mexico northward to Wisconsin, the VAS analysis leads to lower humidities. The addition of VAS data also produces a lower humidity over the Texas panhandle and Oklahoma. The additional moisture over Kansas in the VAS analysis is favorable for the outbreak of convection in Missouri. On the other hand, the drier air over Oklahoma is not conducive to thunderstorm development in this area.

The VAS and NOVAS mixing-ratio analyses at 500 mb (Figs. 4.11a and 4.11b respectively) are much alike, however the addition of VAS

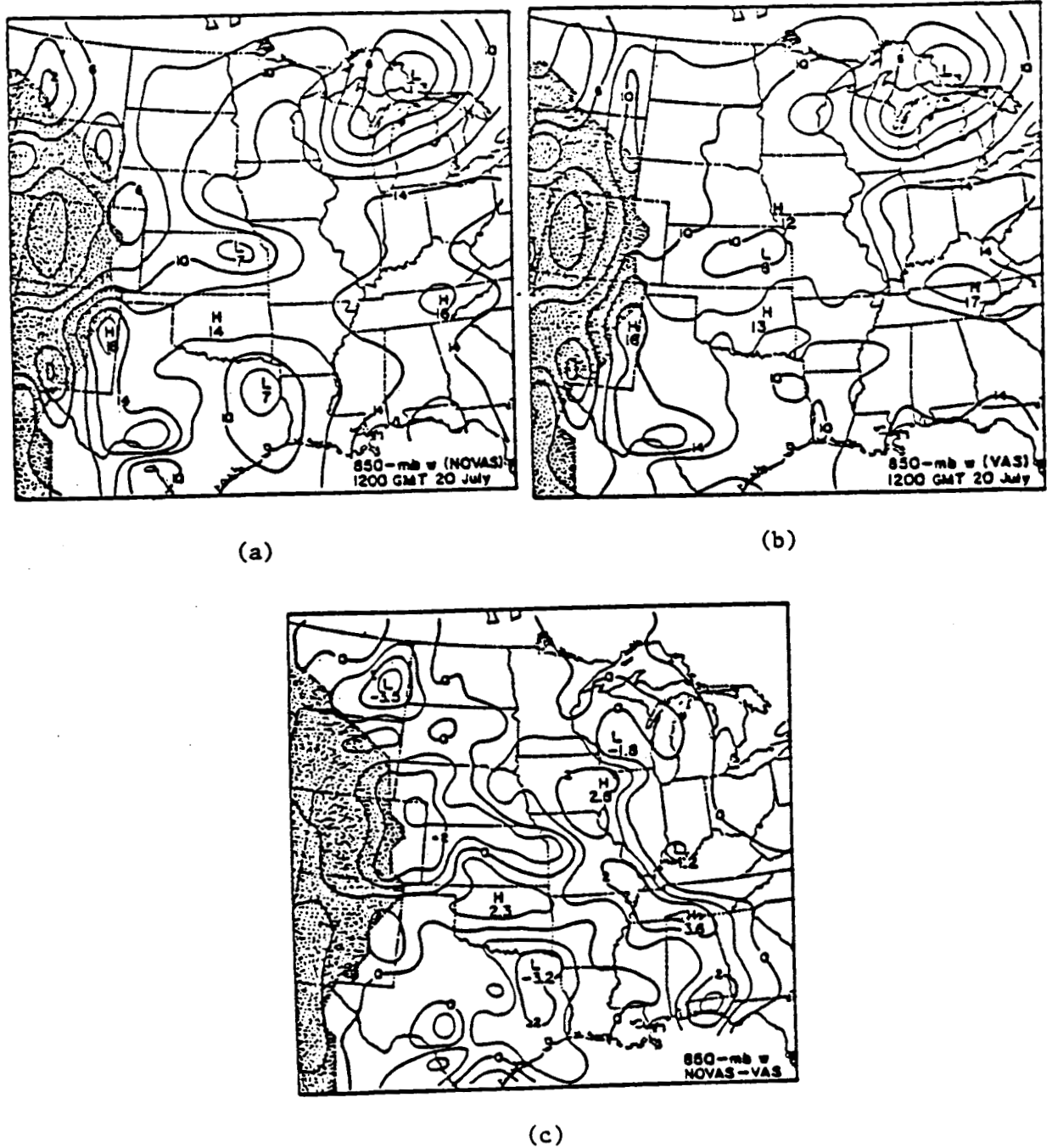


Figure 4.10 NOVAS and VAS 850-mb mixing-ratio analyses for 1200 GMT 20 July 1981. The stipled area represents the region where surface pressure is less than 850 mb.

- NOVAS analysis. The contour interval is 2 g/kg.
- VAS analysis. The contour interval is 2 g/kg.
- Differences between NOVAS and VAS (NOVAS-VAS) analyses. Positive differences indicate a drier VAS analysis. The contour interval is 1 g/kg.

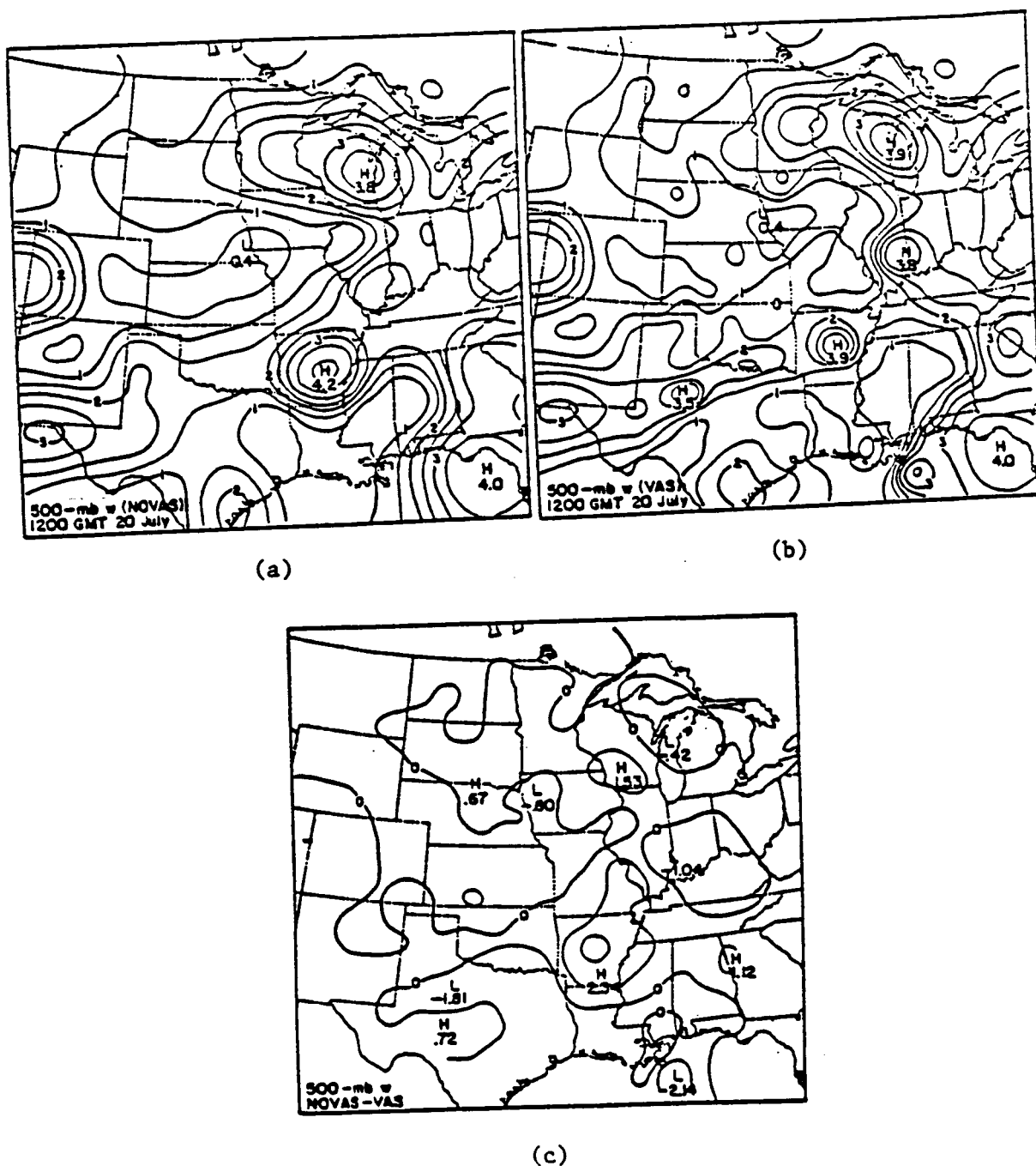


Figure 4.11 NOVAS and VAS 500-mb mixing-ratio analyses for 1200 GMT 20 July 1981.

- NOVAS analysis. The contour interval is 0.5 g/kg.
- VAS analysis. The contour interval is 0.5 g/kg.
- Differences between NOVAS and VAS (NOVAS-VAS) analyses. Positive differences indicate a drier VAS analysis. The contour interval is 1 g/kg.

data does cause a few notable differences. A moisture maximum in southern Illinois is much more prominent in the VAS analysis. A channel of moist air, extending from western Texas to Tennessee, is better defined in the VAS analysis. The VAS analysis also provides more detail along the Gulf coast. Figure 4.11c indicates that the mixing-ratio differences between the two analyses are generally small and isolated.

The 300-mb mixing-ratio values are rather low in both the NOVAS and VAS analyses (Figs. 4.12a and 4.12b) except for several moist areas. Several moisture bulls-eyes are apparent in these analyses and also in mixing-ratio analyses for other levels. The bulls-eyes occur near radiosonde soundings having relatively high mixing-ratio values. Although the accuracy of these radiosonde mixing-ratio values is suspect, no mixing-ratio observations are omitted from the final analysis. A moist tongue, which runs from southwestern Texas to western Missouri, is narrower in the VAS analysis. In Chapter 3, an upper-level channel of very dry air, shown in Fig. 3.5.a, was discussed in terms of being possibly associated with the outbreak of convection over Missouri. The VAS analysis defines this feature over Iowa and southwestern Wisconsin better than does the NOVAS analysis. Figure 4.12c indicates that the VAS analysis has significantly lower mixing-ratio values in southwestern Wisconsin.

Several cross-sections of potential temperature and mixing ratio, nearly perpendicular to the stationary front, were produced from both the NOVAS and VAS analyses. Cross-sections from the NOVAS and VAS analyses are shown in Figs. 4.13b and 4.13c, and the location of these

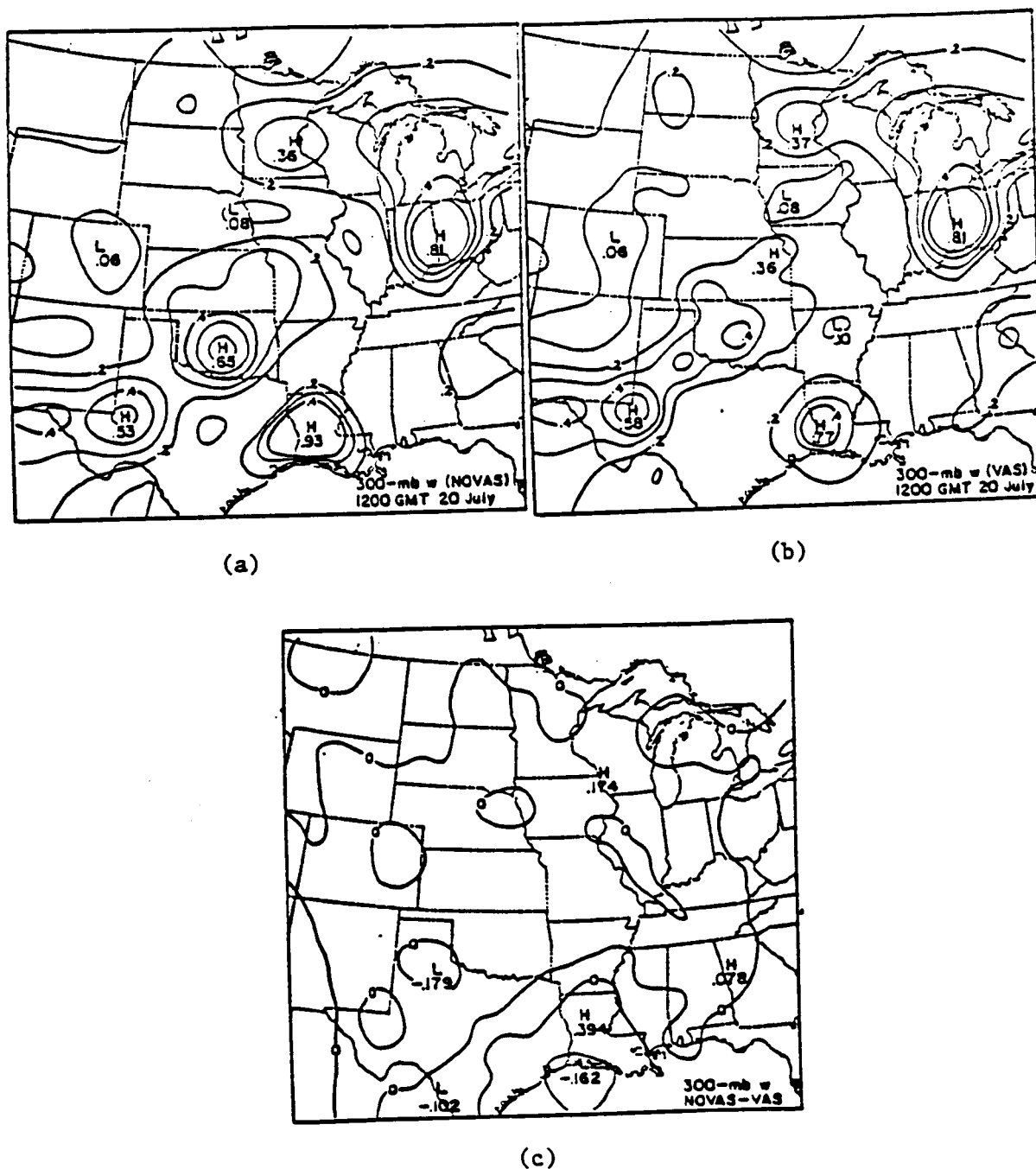
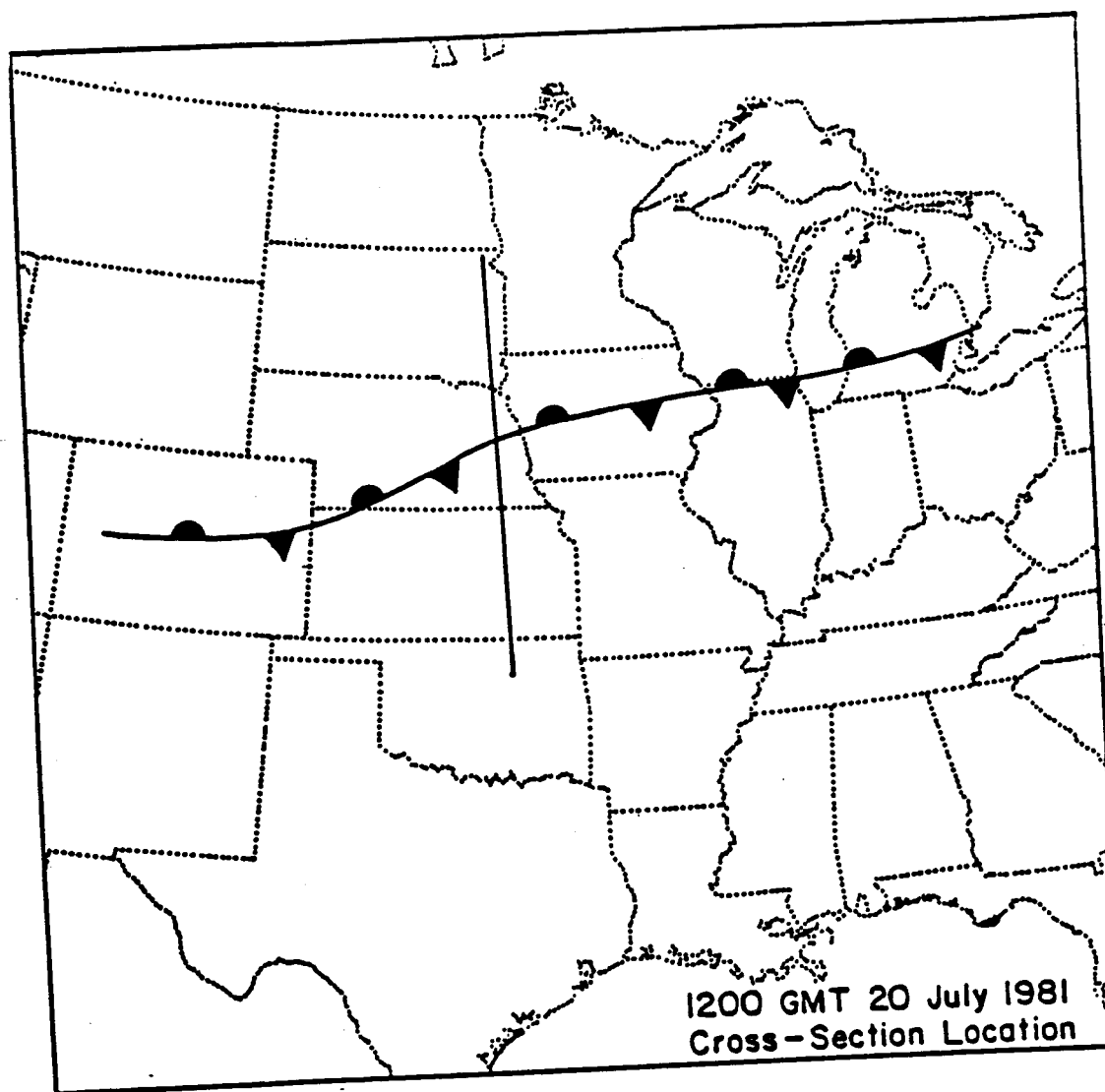


Figure 4.12 NOVAS and VAS 300-mb mixing-ratio analyses for 1200 GMT 20 July 1981.

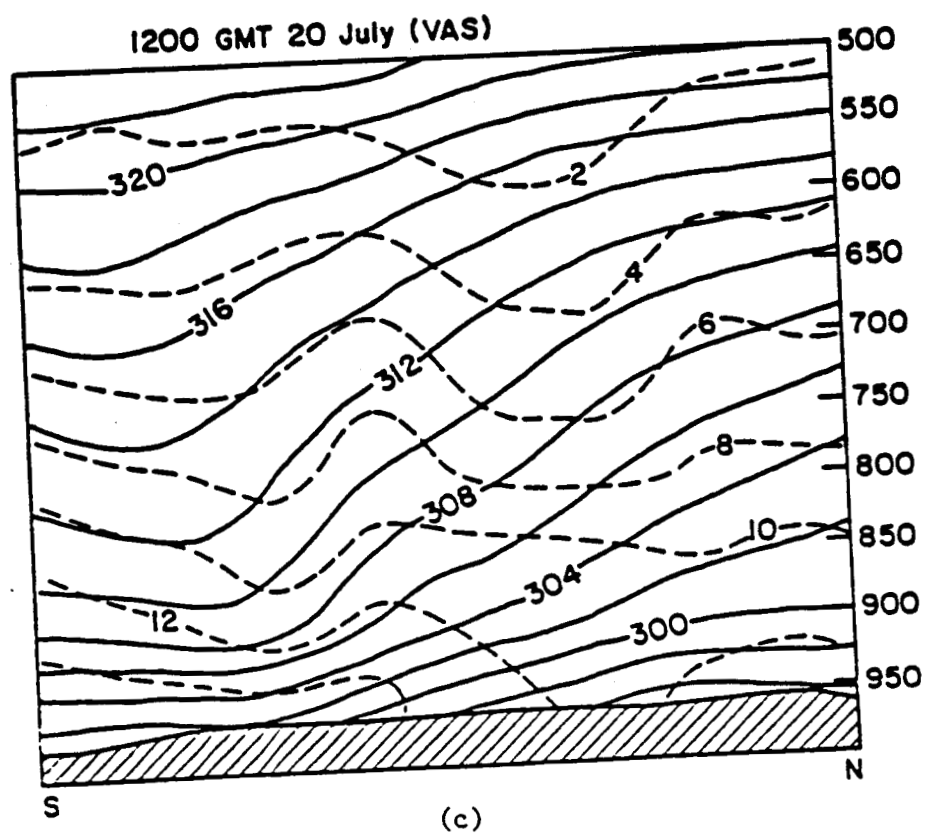
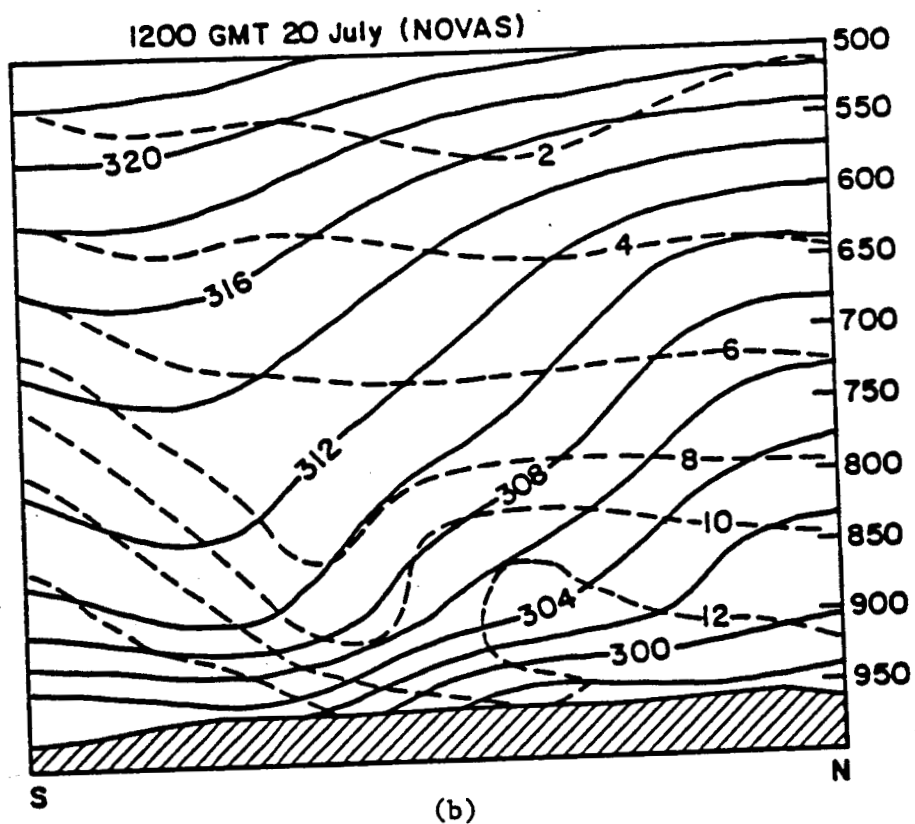
- NOVAS analysis. The contour interval is 0.1 g/kg.
- VAS analysis. The contour interval is 0.1 g/kg.
- Differences between NOVAS and VAS (NOVAS-VAS) analyses. Positive differences indicate a drier VAS analysis. The contour interval is 1 g/kg.



(a)

Figure 4.13 NOVAS and VAS cross-sections of potential temperature and mixing ratio, taken through the stationary front for 1200 GMT 20 July 1981. The contour interval for potential temperature is 2°K . The contour interval for mixing ratio is 2 g/kg .

- a. Locations of the stationary front and the cross-section
- b. NOVAS cross-section
- c. VAS cross-section



cross-sections is indicated in Fig. 4.13a. In these cross-sections, below 900 mb, the temperature gradient across the front is weaker when VAS temperatures were included. Above the 900-mb level, the NOVAS and VAS temperature gradients are of comparable strength. In both cross-sections, some drying is apparent above the surface front, however this feature is more pronounced in the NOVAS analysis. Above 850 mb, it is evident that the VAS analysis of mixing ratio contains more detail than does the NOVAS analysis in the vicinity of this cross-section. The results of this particular cross-section comparison are generally characteristic of what is seen when other cross-sections taken across the stationary front are compared.

As a measure of stability, the change of potential temperature per 50-mb layer was calculated for both the NOVAS and VAS analyses from the surface to the model top. The layer stability between 750 and 700 mb was chosen for comparison because the stability at this level is an important factor in the possible development of convection. For this layer, the stability values from both analyses, fall between 1°K and 4°K per 50-mb layer. To compare the stability of the NOVAS and VAS analyses, a stability difference field (Fig. 4.14) was calculated for the 750-to 700-mb layer. Negative values indicate that the VAS analysis is more stable. The VAS temperature data increase stability over much of the analysis domain. This is especially true for northwestern South Dakota, eastern Colorado and western Kansas, eastern Arkansas, southeastern Louisiana and southern Mississippi, and along the Alabama-Georgia border. This measure of static stability indicates

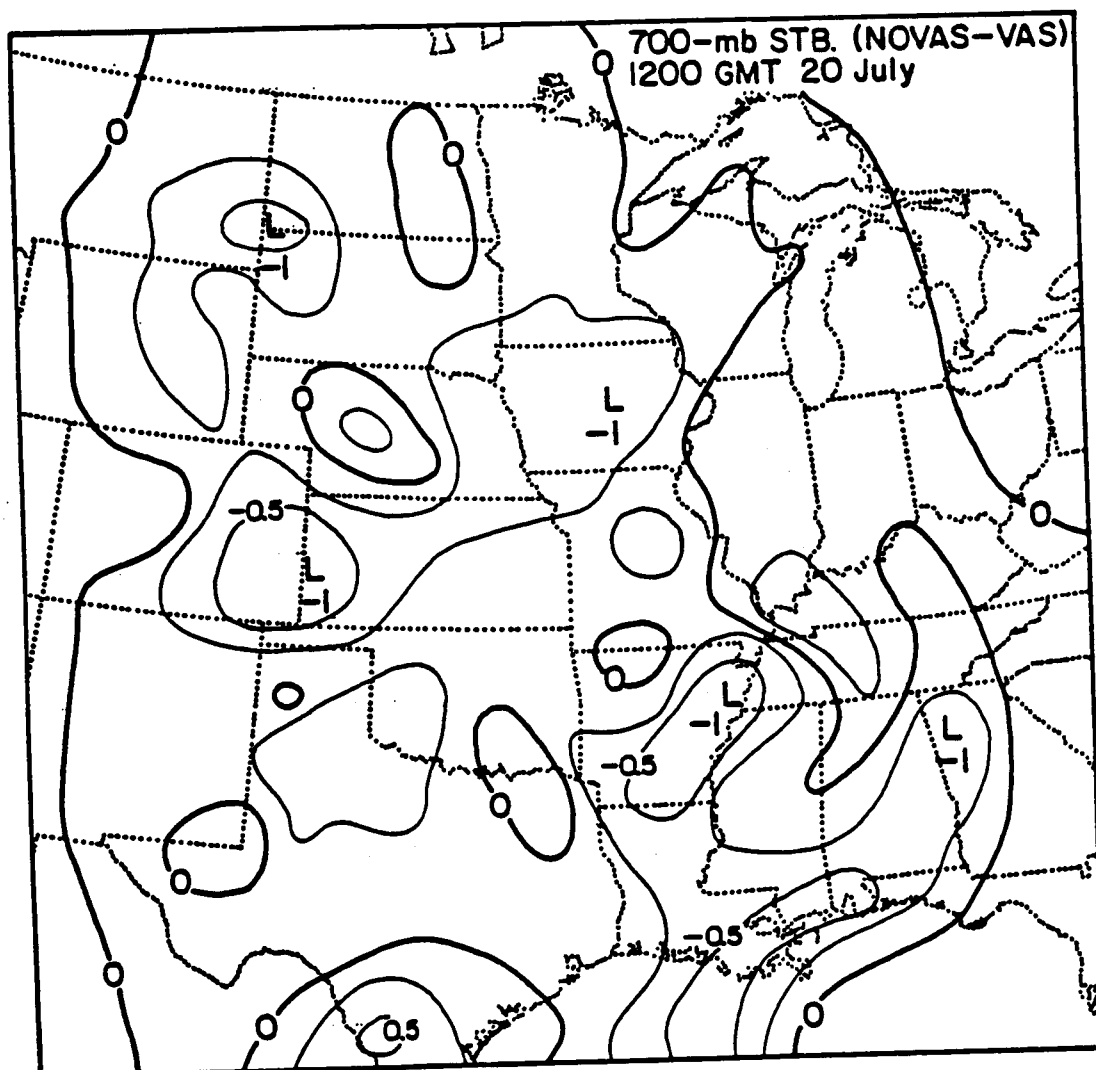


Figure 4.14 Differences in the static stability ($^{\circ}\text{K}/50\text{ mb}$) of the 750- to 700-mb layer between the NOVAS and VAS (NOVAS-VAS) analyses. Positive differences indicate a more unstable atmosphere due to VAS-derived temperatures. The contour interval is $0.25^{\circ}\text{K}/50\text{ mb}$.

that the VAS-defined model atmosphere is possibly less conducive to the support of convective activity in Missouri. It is necessary to point out however, that this stability measure uses a relatively thin layer and does not account for moisture. Comparisons of static stability for other levels show that the stability of NOVAS and VAS analyses is similar for layers above 700 mb but that VAS analyses are generally more stable for layers below 750 mb.

In this section, VAS and NOVAS analyses were examined by comparing temperature and mixing-ratio analyses on three pressure surfaces and along a vertical cross-section through the stationary front. A measure of static stability was also calculated from the VAS and NOVAS analyses. The differences between the two analyses are mostly on the small-scale. In the vicinity of the stationary front, the VAS analysis has a stronger 900-mb temperature gradient through Iowa, but the VAS data weaken the gradient over Missouri. Cold-air advection at 500 mb, believed to be a factor in the development of convection over Missouri, is greater in the NOVAS analysis. The VAS analysis of 850-mb mixing ratio is slightly more favorable for convection in Missouri but less so for thunderstorm development in Oklahoma. The narrow channel of dry air in the upper levels (300 mb) over Iowa and southwestern Wisconsin, is better defined in the VAS analysis. Below 700 mb, atmospheric stability, as measured by the change in potential temperature with height, is generally greater over much of the Midwest in the VAS analysis. All of these differences between analyses are small. For this reason, it is impossible to determine whether either analysis is more conducive to the outbreak of convection.

5.0 EXPERIMENTAL DESIGN

Various combinations of conventional radiosonde data, VAS data, and NMC global analyses from 1200 GMT 20 July were used for the model initialization of seven experiments. Table 5.1 summarizes these experiments in terms of the sources of initial data and whether a dynamic or static initialization was employed.

5.1 Static-Initialization Experiments

Table 5.1 indicates that for experiments E1 through E5 the model was statically initialized and for experiments E6 and E7 it was dynamically initialized. The forecast period for all experiments that used a static initialization was from 1200 GMT 20 July to 0000 GMT 21 July.

Experiment 1 (E1) may be considered the control experiment. A smooth global analysis, obtained from NMC, was modified by radiosonde temperature, wind, and moisture data. In Experiment 2 (E2), both radiosonde and VAS-derived temperature and moisture data were used to enhance the same smooth global analysis. No distinction was made between VAS and radiosonde soundings in this procedure. Both radiosonde and VAS-derived temperature and moisture data were used in E3, but in a different manner than in E2. The temperature and mixing-ratio analyses in E2 were often inconsistent with the radiosonde values. Because the radiosonde soundings are probably less likely to contain bias errors than the VAS soundings, a procedure was developed that corrected the final temperature and moisture analyses from E2 so

Table 5.1 Description of the Analysis/Initialization Procedure

Exp. No.	Temperature		Winds		Mixing Ratio		Initiali- zation
	Data	First Guess	Data	First Guess	Data	First Guess	
E1	R	GA	R	GA	R	GA	S
E2	R+V	GA	R	GA	R+V	GA	S
E3	R	R+V	R	GA	R	R+V	S
E4	-	GA	-	GA	-	GA	S
E5	V	GA	-	GA	V	GA	S
E6	R	GA	R	GA	R	GA	D
E7	R	R+V	R	GA	R	R+V	D

R - radaiosonde
 V - VAS
 GA - NMC Global Analysis

S - static initialization
 D - dynamic initialization

that local gradients defined by the VAS data were retained, but the large-scale structure was adjusted so that the final analyses were more consistent with the radiosonde data. This was accomplished by using an additional analysis cycle, that employed only radiosonde data, to correct temperature and moisture analyses from E2. This adjusted the large-scale characteristics of the field to be consistent with the radiosonde data, but retained the finer structures in the E2 analyses that resulted from the VAS data. Chapter 4 describes the objective analysis procedures used for E1, E2, and E3 in full detail.

Experiments E1, E2, and E3 used an identical initial windfield.

Experiments E4 and E5 were used to evaluate the impact of VAS data, when no radiosonde data are available. In E4, only the smooth global analysis was used for the initial conditions. Even though these analyses are ultimately based on radiosonde data, they are very smooth and have information with the same quality and scale characteristics as could be expected from an accurate forecast from a global model. In E5, VAS-derived temperature and moisture soundings were used to improve the smooth global analysis. Initial winds for experiments E4 and E5 were identical. A comparison of the forecast skill of E4 and E5 provides insight into the value of VAS data in regions where radiosonde data are unavailable.

5.2 Dynamic-Initialization Experiments

In experiments E2 and E3, VAS-derived temperature soundings were used to obtain an initial temperature field, but initial winds were obtained from a synoptic-scale radiosonde network. For mesoscale

motions however, the temperature field adjusts to the wind field during the geostrophic-adjustment process. Therefore it is likely that a significant amount of the horizontal temperature structure provided by the VAS soundings will be lost during the early forecast period in experiments E2 and E3. The dynamic-initialization procedure is an attempt to circumvent this problem by allowing model winds to adjust to the VAS temperatures before the start of the actual forecast. In a dynamic initialization, imbalances between the initial fields of mass and momentum are reduced by the model's predictive equations during a preforecast integration.

Hoke (Hoke, 1976; Hoke and Anthes, 1976; Hoke, 1983) describes a dynamic-initialization procedure that uses a Newtonian nudging approach. An additional term is added to either all or some of the model prognostic equations during a preforecast period to force the model atmosphere toward either individual observations or a target analysis that is based on the observations. During the preforecast period, the general form of the predictive equation for the variable α is

$$\frac{\partial \alpha}{\partial t} = F(\alpha, \underline{X}, t) + G(\alpha, t) \cdot (\alpha_{\text{obs}} - \alpha) \quad (5.1)$$

The first term on the right hand side, $F(\alpha, \underline{X}, t)$, includes all of the model's physical processes. In this term, α represents any predictive variable, \underline{X} is the position vector, and t is time. In the last term, $G(\alpha, t)$ is the nudging coefficient which determines the relative weight of the nudging term with respect to the physical processes. The

nudging coefficient is a nonnegative term that depends on observation accuracy, the distance between the observation and the grid point, and the typical magnitudes of the other terms in the predictive equation. Hoke (1976) found that a good initialization occurred when the time scales for both the slowest major physical adjustment process in the model and the nudging term were similar. Typical values of $G(\alpha, t)$ are 10^{-3} s^{-1} (strong nudging) and 10^{-4} s^{-1} (moderate nudging). The grid point value of α , based on observations, is denoted by α_{obs} . In experiments E6 and E7, the value of α_{obs} was defined based on a linear interpolation in time between analyzed values of α at the beginning and at the end of the preforecast period. Equation 5.1 shows that the magnitude of the nudging term depends on the difference between the forecasted value of α and the observed value, α_{obs} .

For both experiments E6 and E7, a static initialization (based on radiosonde data) was performed at 0000 GMT 20 July. During the preforecast period, which lasted from 0000 GMT to 1200 GMT, model predictive variables were nudged toward values of the target analysis valid at 1200 GMT 20 July. The 1200 GMT target analyses for E6 and E7 were based upon radiosonde data as used in E1 and a combination of radiosonde and VAS data as used in E3, respectively. The actual forecast period, 1200 GMT 20 July to 0000 GMT 21 July, was the same as that used in the static initialization experiments.

All of the predictive variables were nudged during the preforecast period. The nudging coefficient, $G(\alpha, t)$, remained constant with time. The temperature and mixing-ratio fields were nudged strongly using $G = 10^{-3} \text{ s}^{-1}$. Because McPherson (1975) reports that it is important to

use surface pressure observations when assimilating observed temperature data into a numerical model, p^* was moderately nudged using $G = 10^{-4} \text{ s}^{-1}$. Hoke and Anthes (1976) report that, for horizontal scales less than 2000 km in the middle latitudes, nudging toward the mass field alone is not very useful. Therefore, the winds were also moderately nudged ($G = 10^{-4} \text{ s}^{-1}$). It was hoped that this would prevent unnecessary error growth in the large-scale features of the wind field.

The effects of the dynamic initialization and the use of VAS data in the dynamic initialization can be separated by comparison of experiments E1, E6, and E7. The only difference between experiments E1 and E6, which both employ only radiosonde observations, is the dynamic-initialization procedure used in E6. Therefore comparison of these experiments indicates the effect of the dynamic initialization. Experiments E6 and E7 differ in that VAS data are included in E7 but not in E6. The impact of the VAS data in a dynamic initialization can be evaluated by comparing the results of E6 and E7.

6.0 THE NUMERICAL MODEL

The model used in this study is a modified version of the three-dimensional, mesoscale model developed at The Pennsylvania State University by Anthes and Warner (1978). The model contains a high-resolution planetary boundary-layer (HRPBL) parameterization (Blackadar, 1976, 1978, 1979; Zhang and Anthes, 1982). Following a brief discussion of the model and its HRPBL parameterization, is a general description of the model initialization procedure used for this study.

6.1 Model Description

The Penn State/NCAR mesoscale model is a limited-area, hydrostatic, primitive-equation model that uses a staggered horizontal grid and a staggered vertical grid. The vertical, terrain-following coordinate is defined by $\sigma = (p - p_t)/p^*$ where $p^* = p_{sfc} - p_t$, p is pressure, p_t is the constant pressure at the top of the model, and p_{sfc} is the surface pressure. The important features and parameters of the model are summarized in Table 6.1.

A horizontal grid was chosen so that available VAS data would cover a large, central portion of the model domain. This grid contains 43×43 points, spaced 60 km apart, and is centered at 39°N latitude and 95°W longitude. The vertical structure (Table 6.2) of the model is defined by fourteen computational levels, which are concentrated in the lower troposphere to better resolve boundary-layer structure.

Table 6.1 Summary of Model Features and Parameters

Model:	Hydrostatic, three-dimensional, predictive (Anthes and Warner, 1978)
PBL:	High resolution, one-dimensional, multi-layer; surface heating determined by surface energy budget using horizontal variability of the surface parameters
Moisture cycle:	Stable and convective modes of precipitation
Predicted variables:	$u, v, T, q,$ and $p^* = p_{sfc} - p_t$
Coordinate system:	$x, y, \sigma = (p - p_t)/p^*$
Map projection:	Lambert Conformal, true at 30°N and 60°N
Numerics:	Fourth-order diffusion; second-order advection; centered-in-time, centered-in-space finite differencing; Brown-Campana (1978) pressure-force averaging
Lateral boundaries:	p^*, p^*q, p^*T, T specified p^*u, p^*v extrapolated u, v extrapolated on outflow, specified on inflow
Grid structure:	
Horizontal:	Staggered (lattice B as described by Messinger and Arakawa (1976)): u and v defined at dot points with all other variables at cross points
Vertical:	Staggered; $d\sigma/dt$ defined at sigma levels with all other variables defined at half-sigma levels
Grid dimensions:	43 x 43 x 14, centered at 30°N and 95°W
Grid length:	60 km
Model top (p_t):	100 mb
Model base:	Half-degree global terrain data, archived at the National Center for Atmospheric Research (NCAR)
Integration period:	
Forecast:	1200 GMT 20 July to 0000 GMT 21 July 1981
Preforecast:	0000 GMT 20 July to 1200 GMT 20 July 1981
Time step:	120 s

Table 6.2 Vertical structure of the model. Pressure levels (p) based on $p_{sfc} = 1000$ mb, weighting function for convective heating (N), and vertical eddy flux of water vapor (W) are tabulated against sigma at the computation levels.

Sigma	p(mb)	N	W(μbs^{-1})
0.050	145.0	0.375	0.000
0.150	235.0	1.050	9.000
0.250	325.0	1.575	7.000
0.350	415.0	1.875	3.500
0.450	505.0	1.725	-0.500
0.550	595.0	1.525	-3.500
0.650	685.0	1.200	-7.500
0.750	775.0	0.675	-8.000
0.830	847.0	0.000	0.000
0.885	896.5	0.000	0.000
0.925	932.5	0.000	0.000
0.955	959.5	0.000	0.000
0.984	985.6	0.000	0.000
0.999	999.1	0.000	0.000

The equations of motion in flux form, continuity equations for mass and water vapor, and the thermodynamic equation are described in Anthes and Warner (1978). The effects of radiation and evaporation are included in the surface energy budget, but not in the thermodynamic equation for the free atmosphere. The parameterization scheme for subgrid-scale precipitation is described by Anthes and Warner (1978) and Anthes (1977). The amount of subgrid-scale precipitation and its associated latent heat release is proportional to the vertically integrated moisture convergence, once a threshold in this quantity has been reached. The calculation of the vertical distribution of convective heating and moistening is described by Anthes and Keyser (1979). Table 6.2 includes the parameters that determine the vertical distribution of convective heating and moistening. This vertical distribution is held constant in space and time. Noise from the aliasing process (defined by Haltiner and Williams, 1980) is suppressed by fourth-order diffusion on the domain interior and by second-order diffusion near the lateral boundaries.

The upper constant-pressure boundary of the model was chosen to be 100 mb. The terrain elevation at the lower boundary (Fig. 6.1) was interpolated from half-degree global terrain data archived at NCAR. On the lateral boundaries, p^* , p^*q , p^*T , and T were specified by a linear interpolation in time between 12-h observations. The horizontal momentum fluxes, p^*u and p^*v , were extrapolated outward from the forecast values at interior grid points. During outflow conditions, boundary values for u and v were defined using a zero-order

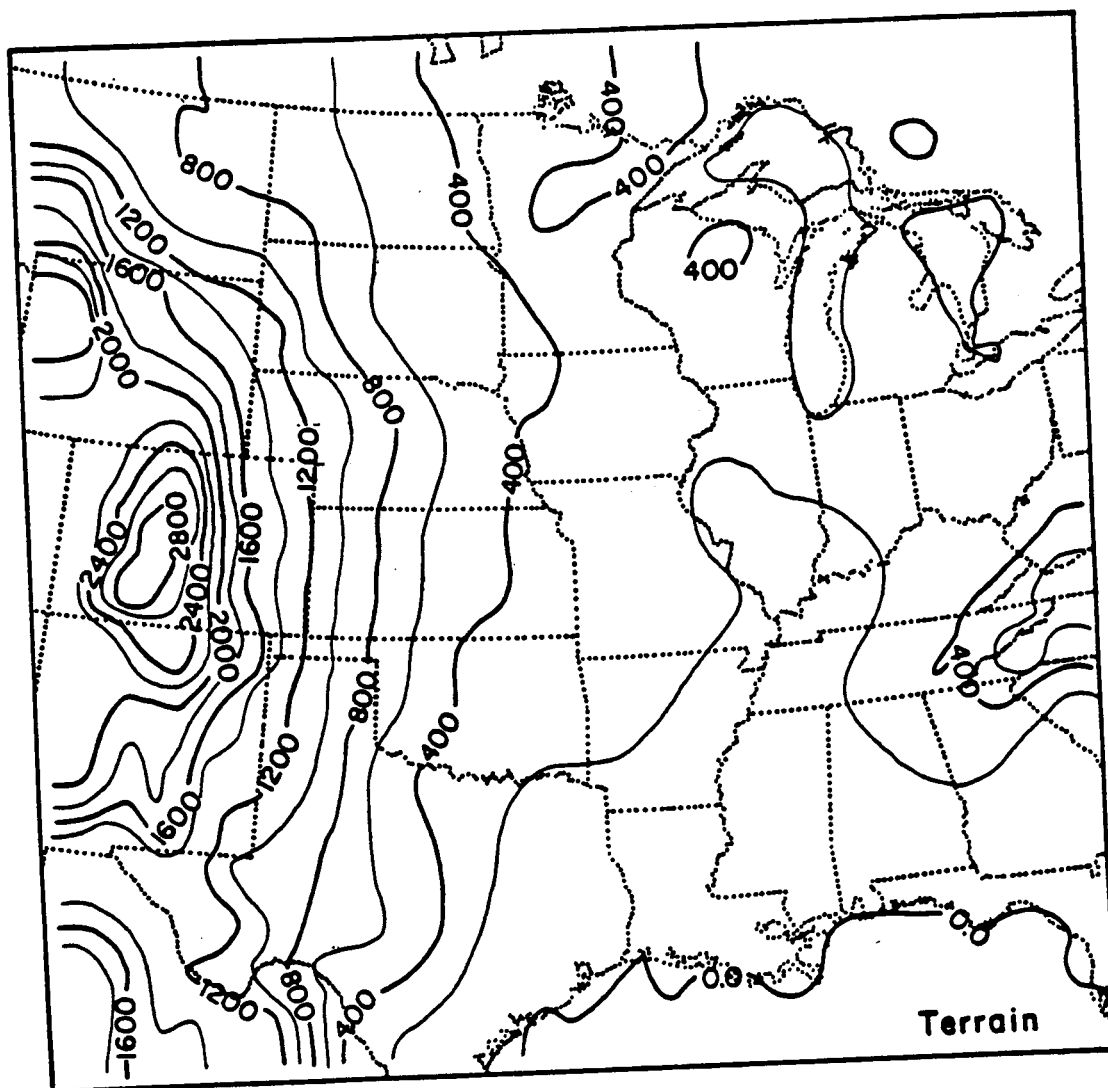


Figure 6.1 Model terrain for numerical simulations. The contour interval is 200 meters.

extrapolation outward from interior points. Boundary values of u and v were specified for inflow conditions.

6.2 High-Resolution Planetary Boundary-Layer Parameterization

The HRPBL contains both stable and unstable modes. Under stable conditions, K theory is used to calculate turbulent fluxes. During unstable conditions, heat, momentum, and moisture are exchanged directly between the surface layer and each layer of the mixed layer. Therefore, vertical transport is determined by the thermal structure of the entire mixed layer, allowing for accurate simulation of the counter-gradient fluxes observed in this regime.

The ground temperature and its temporal change largely determine the behavior of the HRPBL. Ground temperature is predicted by a surface energy budget (Blackadar, 1978) which includes the effects of the net longwave and shortwave irradiance at the surface, the heat flux by molecular conduction into the soil substrate, and the sensible and latent heat fluxes into the atmosphere. These processes depend on the following surface parameters: thermal inertia, emissivity, albedo, moisture availability, and roughness length. Values of these surface parameters were allowed to vary horizontally over the model domain. A surface index map (Fig. 6.2) was used to assign surface index values to each grid point. The formulation of this surface index map follows Benjamin (1983). Table 6.3 specifies surface parameter values for each surface index.

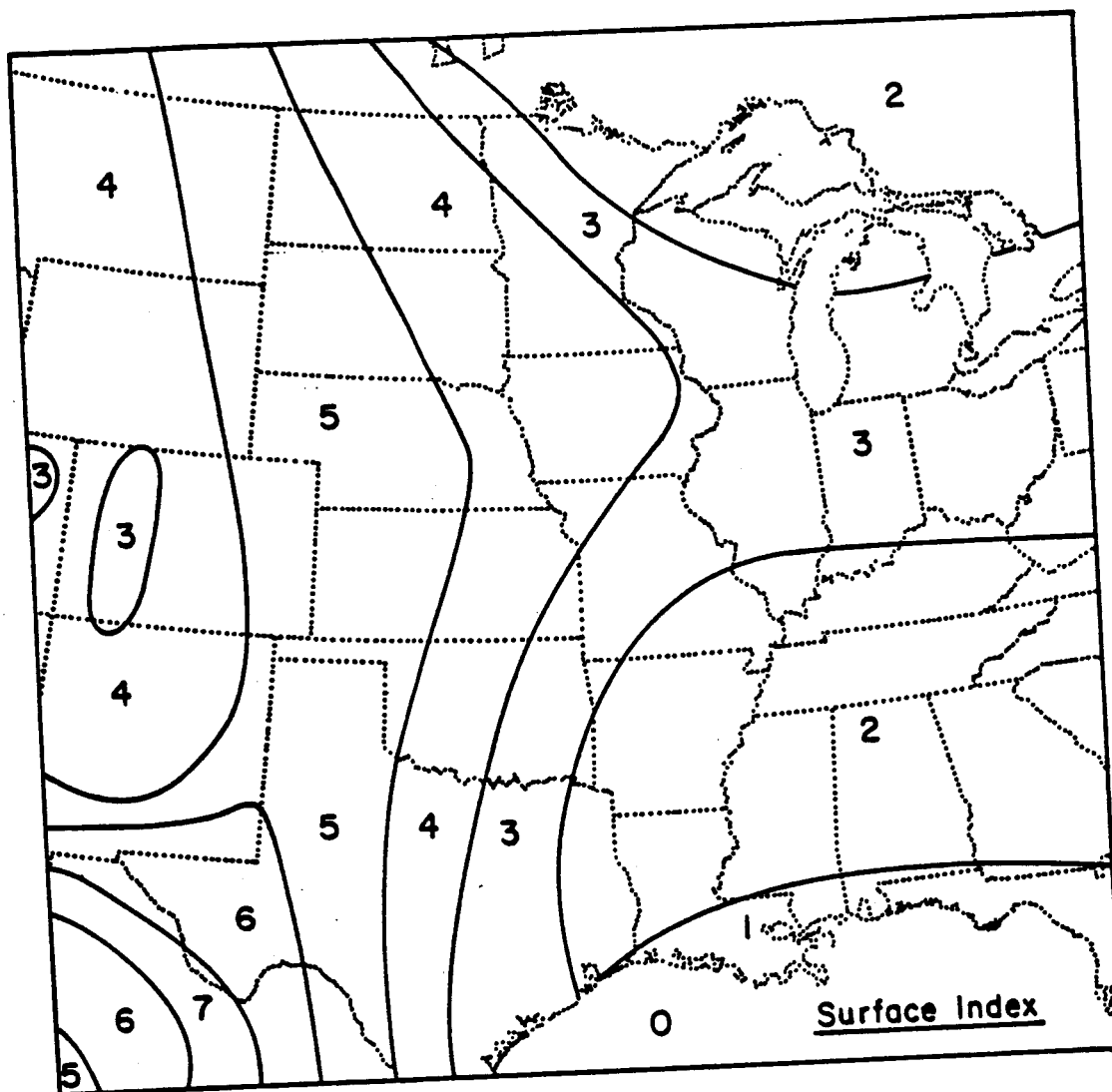


Figure 6.2 Surface index distribution for numerical simulations. Table 6.3 was used to specify surface characteristics from the surface index assigned to each grid point.

Table 6.3 Surface Characteristics Used for Each Surface Index Type

Surface Index	Type of Surface	Surface Albedo (%)	Soil Moisture Availability	Thermal Inertia ($\text{cal cm}^{-2} \text{s}^{-0.5 \text{ K}^{-1}}$)	Surface Emissivity at $9 \mu\text{m}$ $\% \times 10^{-2}$	Surface Roughness Length (cm)
0	Ocean	6	1.0	0.1	1.00	0.01
1	Rain Forest, Swamp	8	0.83	0.08	0.97	100.00
2	Woodland	10	0.75	0.07	0.95	50.00
3	Mixed Grass and Trees	12	0.60	0.06	0.92	30.00
4	Crops and Grass (pasture land)	15	0.30	0.05	0.90	20.00
5	Semi-arid (Shrubs and Trees)	20	0.10	0.04	0.85	10.00
6	Arid (Shrubs)	25	0.05	0.03	0.80	5.00
7	Desert (Sparse-grass)	30	0.02	0.02	0.75	1.00

6.3 Initialization

All experiments were initialized by first interpolating from the NMC northern-hemisphere octagonal grid to the grid points of the model domain. NMC fields include horizontal winds and temperatures at all mandatory levels, relative humidity at three levels, sea level pressure, and surface temperature. These fields were then interpolated to supplementary analysis levels at 600, 780, 900, 940, and 980 mb. Data at mandatory and supplementary levels were enhanced with standard radiosonde and VAS observations. A successive-correction technique was used for the objective analysis. Details of the specific initialization procedures used in this study are discussed in Chapter 4. After determining the surface pressure hydrostatically from sea-level pressure and terrain height, all three-dimensional fields were interpolated to model sigma surfaces. No balancing was performed on the initial mass and momentum fields. However, the vertically averaged mass divergence in a column was removed from the wind field to minimize noise early in the forecast. This procedure results in an initial pressure tendency of zero while allowing non-zero vertical motions.

7.0 RESULTS

A number of measures were used to determine the forecast skill associated with each of the seven experiments that were summarized in Table 5.1. An objective analysis, based upon both VAS and radiosonde observations, was produced for 0000 GMT 21 July and used for verification purposes. SI scores and average-error statistics were computed using the grided forecast and verification data. Regional differences and similarities between the forecasts and verification fields were also examined. Model-produced rainfall was compared with observed rainfall for the same period. Finally, gravity-inertia wave noise characteristics of the forecasts were evaluated.

7.1 Verification Procedure

Radiosonde wind, temperature, and moisture observations from 0000 GMT 21 July 1981 and VAS-derived temperature and moisture data, valid for 2301 GMT 20 July, were objectively analyzed for forecast-verification purposes. The objective analysis procedure used to obtain these verification fields is the same as that described in Section 4.2.2, in which large-scale features are adjusted using radiosonde data in a second analysis cycle. There was uncertainty about whether or not VAS data should be used in the construction of the verification fields. However, the use of VAS observations should impart additional mesoscale structure to the analyses. It was felt that the advantages of using the VAS data outweighed the disadvantages, especially since the model produced mesoscale features in the forecast fields.

7.2 Verification Statistics

The relative skill of the 12-hour numerical forecasts was quantified by computing S1 scores and root-mean-square and average errors. Table 7.1 shows S1 scores for sea-level pressure, 700-mb height, and 500-mb height as well as average errors for the upper, middle, and lower troposphere. The S1 score relates horizontal differences in forecast sea-level pressure or geopotential height to the observed differences. No smoothing was applied to the forecast fields in the S1-score computations. Average-error statistics were computed on model sigma surfaces for temperature, mixing ratio, wind speed, wind direction, and surface pressure. Error values were then averaged for upper-, mid-, and lower-level sigma surface and these statistics were included in Table 7.1. These three layers roughly correspond to the following pressure (p) intervals: p less than 500 mb, p between 850 mb and 500 mb, and p greater than 850 mb.

From inspection of Table 7.1, it is apparent that the model predictive skill, at least as measured by these types of statistics, was not very sensitive to the type of data or the initialization procedure used. Some interesting trends are evident however. Comparison of E2 and E3 with E1 indicates the impact on forecast skill of using VAS data together with radiosonde data for the model initialization. The mass field statistics, for sea-level pressure and temperature in the lower, middle, and upper model layers, show a slight improvement when VAS data are employed. There is also a modest reduction in mixing-ratio error associated with the use of VAS data. This is most apparent for low levels. The wind-speed error is slightly

7.1 Forecast Verification Statistics

<u>Sl scores</u>	<u>E1</u>	<u>E2</u>	<u>E3</u>	<u>E4</u>	<u>E5</u>	<u>E6</u>	<u>E7</u>
sea-level preessure	56.7	55.5	55.5	54.5	58.4	54.1	54.8
700-mb height	40.5	39.0	40.1	42.6	45.3	44.0	43.7
500-mb height	33.8	33.3	32.9	34.3	36.1	36.0	36.0
<u>Average errors</u>							
Temperature ($^{\circ}\text{C}$)							
High	0.78	0.68	0.70	0.80	0.64	0.75	0.66
Middle	0.74	0.66	0.69	0.75	0.63	0.72	0.69
Low	1.43	1.40	1.41	1.58	1.37	1.71	1.76
Mixing Ratio (g kg^{-1})							
High	0.17	0.16	0.16	0.16	0.15	0.17	0.16
Middle	1.24	1.22	1.22	1.17	1.18	1.22	1.18
Low	2.52	2.24	2.28	2.76	2.25	2.26	2.09
Wind Speed (ms^{-1})							
High	3.82	3.96	3.90	3.65	3.76	3.93	4.11
Middle	2.88	2.84	2.90	3.06	3.10	2.94	3.02
Low	2.00	2.02	2.02	1.98	2.03	2.09	2.07
Surface Pressure (mb)	0.81	0.85	0.84	0.71	1.27	0.93	0.89

higher when VAS data are included. The surface-pressure forecasts are a little worse with VAS data, probably because of the slightly larger-amplitude, deep, gravity-inertia waves.

It is interesting to speculate about the possibility that there is a systematic relationship between the verification statistics and whether VAS data were used in the initialization and verification of a variable. For example, if VAS temperature data are used and they impart some mesoscale structure to the wind field during the forecast period, the predicted winds are going to verify worse than those produced by the no-VAS initialization because the wind-field verification data have no structure on the VAS scale.

Comparison of these verification statistics for E2 and E3 indicates that the modified method of incorporating VAS soundings with radiosonde observations had no perceptible impact on forecast skill. This is not surprising because the results of the objective-analysis procedures used for the initialization of E2 and E3 were so similar. The additional corrective cycle, used in E3, had little impact. That is, throughout much of the domain, temperature and mixing-ratio values changed little when the corrective cycles were applied.

Evaluation of the results of E4 and E5 illustrates how effectively VAS data alone can be used to modify a smooth first-guess field which is based upon a global-scale analysis. The S1 scores for both E4 and E5 are consistently worse than the S1 scores for E1, E2, and E3 where either radiosonde or a combination of radiosonde and VAS data were employed. The S1 scores in E5 are especially high. A possible explanation for this occurrence is that significant temperature

gradients in the initial conditions are likely at the boundary between the area covered by the VAS data and the rest of the global analysis. These spurious temperature gradients would adversely affect the forecast of both sea-level pressure and the 700-mb and 500-mb height fields. Inspection of the initial 700-mb and 500-mb temperature analysis, however, indicates no evidence of any discontinuity near the boundary of the VAS network. The average errors for temperature show a very positive impact of VAS in E5. In fact, these temperature errors are smaller than those resulting from any other initialization technique. There is very little difference in the average error of mixing ratio between E4 and E5 for the upper and middle levels. However, for low levels, the moisture forecast in E5 is significantly better than that in E4. This is consistent with the comparison of the results of E1, E2, and E3, in which the addition of the moisture data also had its most positive impact at low levels. As before (i.e., the E1, E2, E3 comparison), the wind field verifies slightly worse with VAS data. Surface-pressure errors are relatively low in E4; however, these errors are quite high in E5. This poor forecast of surface pressure in E5 may be due to the existence of higher-amplitude gravity-inertia wave noise.

Comparison of experiments E7, E6, and E1 allows us to separate the effects of the dynamic initialization itself and the use of VAS data in the dynamic initialization. There is no systematic improvement in forecast skill when the dynamic-initialization procedure is used with only radiosonde data (compare E6 and E1). Inspection of the temperature and moisture statistics for E6 and E7 indicates that the

use of VAS data in the target analyses of temperature and mixing ratio had a positive impact on skill except for low-level temperature. Again, the wind statistics verify worse when the VAS data are employed. The VAS soundings have a slightly positive impact upon the forecast of surface pressure.

7.3 General Comparison of the Forecast Results

Forecast fields of sea-level pressure, temperature, geopotential height, horizontal wind, and mixing ratio from experiments E1 to E7 are compared with each other and also with the verification fields (obtained as described in Section 7.1) and the NMC analyses of these variables. The initial conditions used in E3 and the verification conditions are also compared to give some indication of how the atmosphere changed during the forecast period. Sea-level pressure, 500-mb temperature and geopotential height, 500-mb wind, and 850-mb mixing ratio are chosen, as a small sample, to be shown in the following figures. In general, there are few significant differences among the forecasts. For this reason, only results from experiments E1 and E3, together with initial and verification conditions, are included among the figures.

Figure 7.1a is a 1200 GMT 20 July sea-level pressure analysis and Figs. 7.1b, 7.1c, and 7.1d are 0000 GMT 21 July sea-level pressure fields based on the verification data, and from the E1 and E3 forecasts, respectively. Comparison of Figs. 7.1a and 7.1b indicates that, during the forecast period, the low-pressure system near the Great Lakes moved eastward and intensified. Experiments E1 and E3

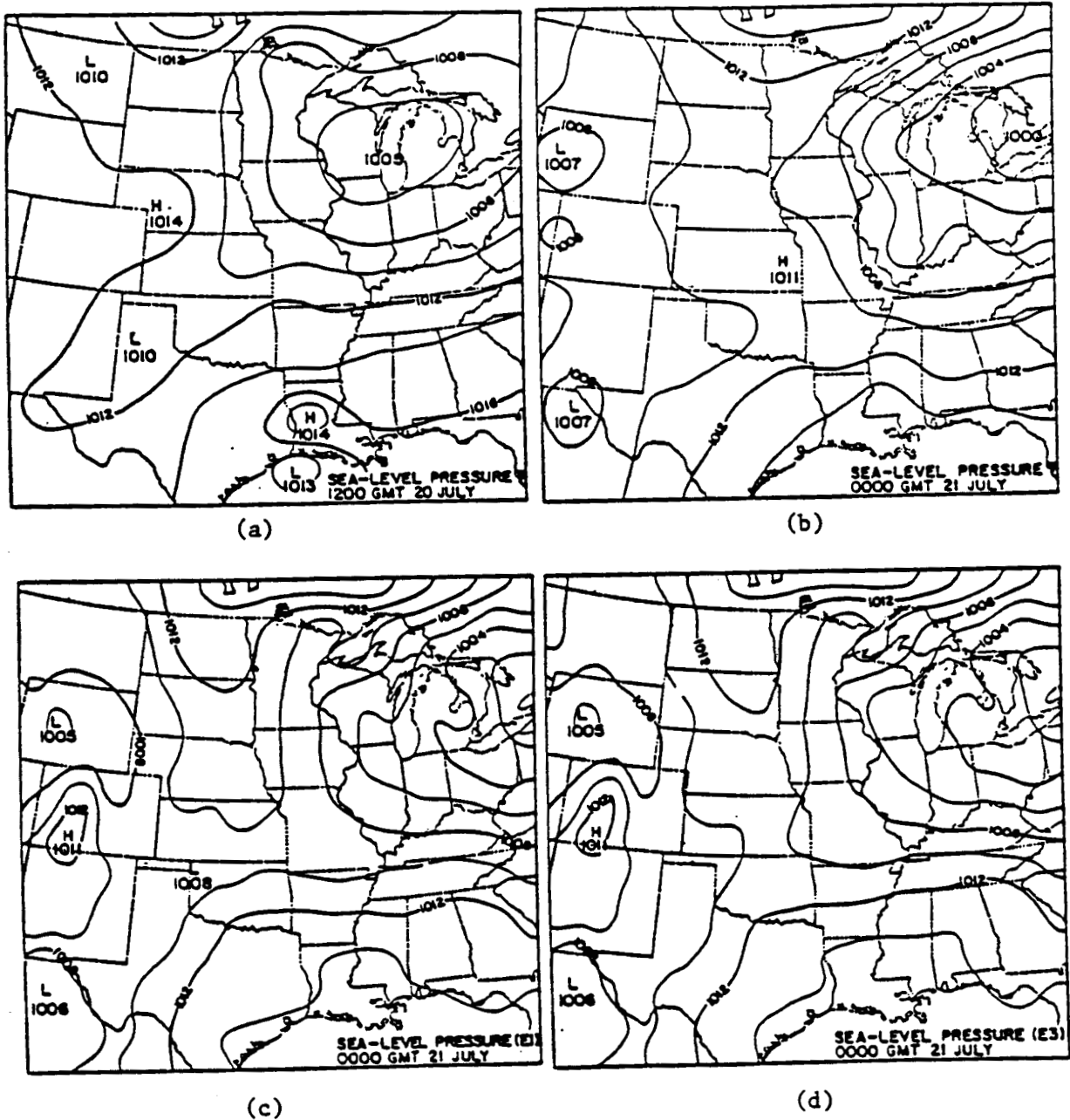


Figure 7.1 Sea-level pressure analyses. The contour interval is 2 mb.

- a. Observed sea-level pressure, valid 1200 GMT 20 July 1981
- b. Observed sea-level pressure, valid 0000 GMT 21 July 1981
- c. Forecast (E1) sea-level pressure, valid 0000 GMT 21 July 1981
- d. Forecast (E3) sea-level pressure, valid 0000 GMT 21 July 1981

handle this feature reasonably well, although the observed central pressure is slightly less than that of either forecast. A small area of high pressure, located over Louisiana at 1200 GMT 20 July, is no longer apparent at 0000 GMT 21 July in either the verification analysis or in the E1 and E3 forecasts. Both forecasts inappropriately put a wave in the isobars over the Great Lakes. Also, an area of high pressure, centered over southern Colorado, was erroneously forecast. Although all seven sea-level pressure forecasts are very similar, some differences between forecasts are evident. The forecast sea-level pressure pattern over Kansas and Nebraska in E3 agrees more closely with the verification analysis than does the pattern from E1. Also, the low-pressure system is handled better in E6 and E7 than it is in the other forecasts.

The 500-mb temperature and geopotential height fields for the initial and verification conditions and the E1 and E3 forecasts are shown in Figs. 7.2a, 7.2b, 7.2c, and 7.2d respectively. Figures 7.2a and 7.2b indicate that during the forecast period there are no large changes in either the 500-mb temperature field or the 500-mb geopotential height field. The forecast fields are very similar for all experiments and also agree fairly well with the verification fields, although the forecast temperature fields are smoother and they also indicate more of a thermal trough in the Midwest. Surface temperature forecasts differ only slightly. None of the forecast low-level temperature fields clearly indicate the position of the cold front at 0000 GMT 21 July. The skill of the 850-mb and the 300-mb

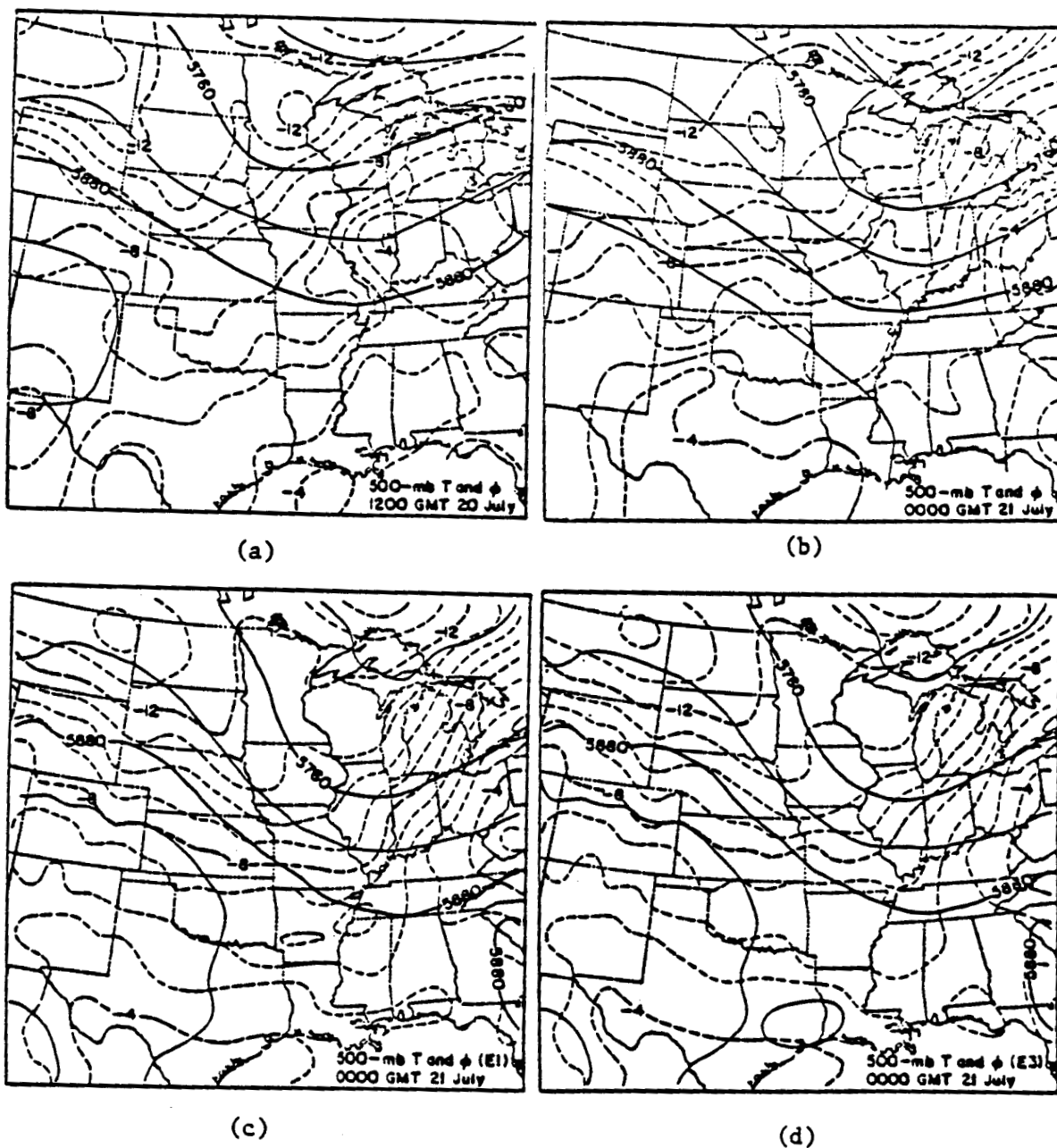


Figure 7.2 500-mb temperature (T) and geopotential height (ϕ) analyses. The contour interval for temperature is 1°C . The contour interval for geopotential height is 60 meters.

- Observed 500-mb temperature and geopotential height, valid 1200 GMT 20 July 1981
- Observed 500-mb temperature and geopotential height, valid 0000 GMT 21 July 1981
- Forecast (E1) 500-mb temperature and geopotential height, valid 0000 GMT 21 July 1981
- Forecast (E3) 500-mb temperature and geopotential height, valid 0000 GMT 21 July 1981

C-2

temperature forecasts is also found to be fairly independent of the analysis procedure or the initial data used.

The observed 500-mb winds from 1200 GMT 20 July and 0000 GMT 21 July are shown in Figs. 7.3a and 7.3b and the forecast (E1 and E3) 500-mb winds are shown in Figs. 7.3c and 7.3d. The similarity in the predicted mid-level wind fields of experiments E1 and E3, is readily apparent. An important feature in the 500-mb wind field of 1200 GMT 20 July is the region of strong winds (greater than 20 ms^{-1}), associated with the 500-mb trough, that stretches from Wyoming to northwestern Missouri. By 0000 GMT 21 July, this area has shifted eastward so that it covers an area from Nebraska to West Virginia. Maximum wind speeds in this feature increase slightly during the 12-hour period. This region of high wind speed is evident in both E1 and E3, although wind speeds are under-forecast, especially from Illinois to West Virginia. Also during this period, an area of very light winds drifts eastward from Minnesota to just north of Michigan. This is correctly forecast by both E1 and E3, however E3 handles the wind-speed minimum a little better. An area in southern Wyoming, having wind speeds in excess of 20 ms^{-1} , is apparent in the E1 and E3 forecasts. At 1200 GMT 20 July, observed wind speeds for this area are also greater than 20 ms^{-1} , however by 0000 GMT 21 July they have diminished significantly. Neither forecast correctly predicted this reduction in wind speed. The 500-mb wind forecasts from the other five experiments are also similar to those from E1 and E3, although the winds from E4 and E5 are somewhat weaker and smoother. The general

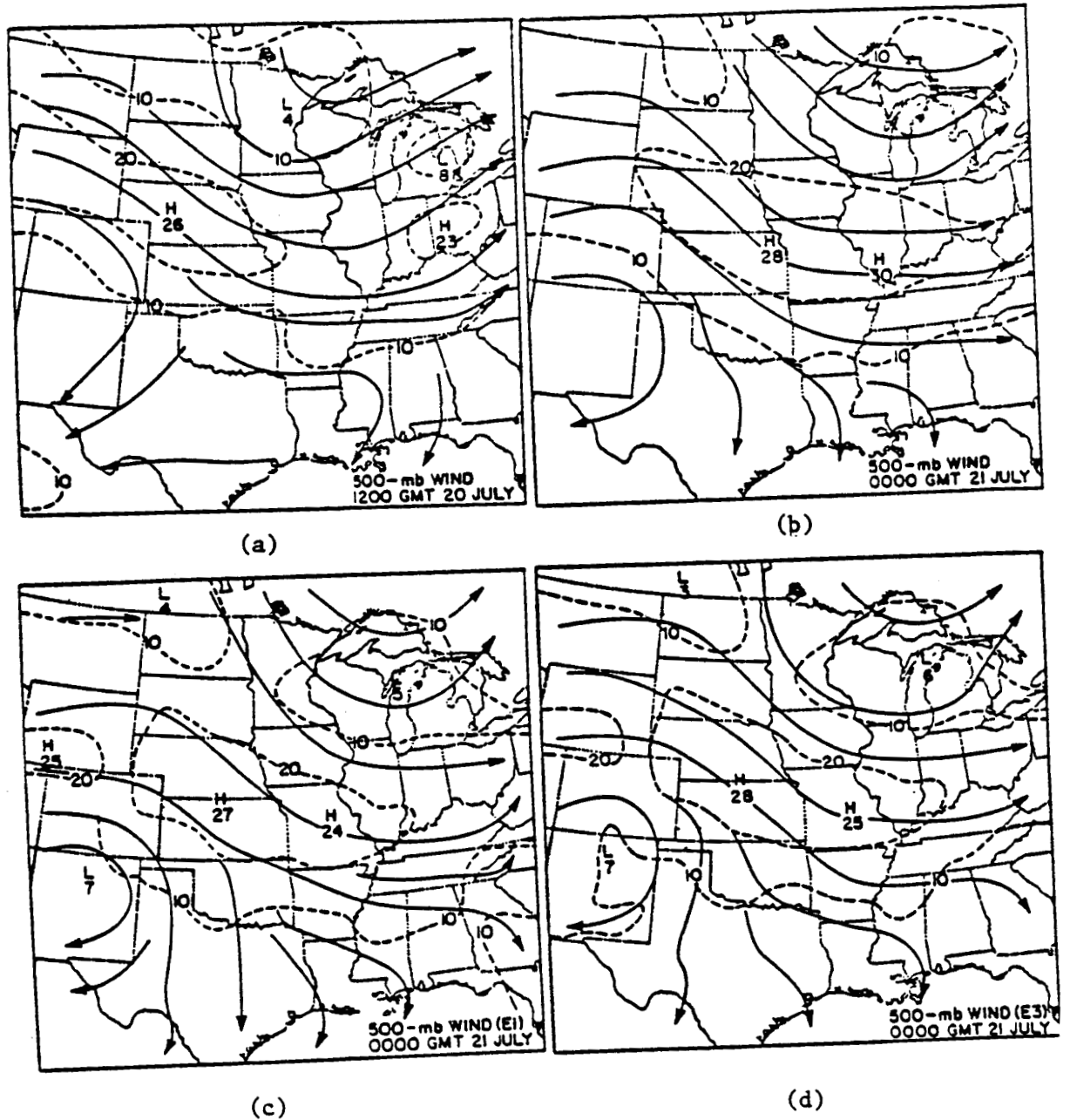


Figure 7.3 Streamline and isotach analysis of the 500-mb wind. The contour interval for wind speed is 10 ms^{-1} .

- a. Observed 500-mb wind, valid 1200 GMT 20 July 1981
- b. Observed 500-mb wind, valid 0000 GMT 21 July 1981
- c. Forecast (E1) 500-mb wind, valid 0000 GMT 21 July 1981
- d. Forecast (E3) 500-mb wind, valid 0000 GMT 21 July 1981

characteristics of the forecast winds from 850 mb and 300 mb correspond to those of the observed winds at these levels.

Figures 7.4a, 7.4b, 7.4c, and 7.4d are 850-mb mixing-ratio fields from the initial and verification conditions and from E1 and E3 respectively. The general characteristics of the forecast low-level moisture fields are similar in both E1 and E3 as well as in the other forecasts. There are, however, some noteworthy differences between the forecast and observed mixing-ratio fields. In all of the forecasts, a moisture gradient extending from west Texas northward to the Dakotas is evident. This feature is much less apparent in the verification fields. Observations (Figs. 7.4a and 7.4b) indicate that significant moistening occurred in southwestern Kansas during the forecast period. Neither experiment predicts this moistening; instead, both forecast lower moisture values. A plausible explanation for this discrepancy is that the observed winds in this region remained generally southerly and advected moist air; however the forecast winds rotated to westerly and then to northerly directions, bringing in relatively dry air. During the forecast period, mixing-ratio values in eastern Kansas, Missouri, and southern Illinois decrease enough so that an extensive dry tongue is apparent in the verification analysis. Although the forecast wind direction is fairly consistent with the observed wind direction in this area, neither E1 nor E3 forecasts this dry region. The 850-mb mixing-ratio analyses from the intermediate forecast times indicate that additional moisture was drawn into this area from Oklahoma. Figures 7.4a and 7.4b also indicate some moistening from eastern Texas to Alabama, however forecast mixing-ratio values remain nearly the

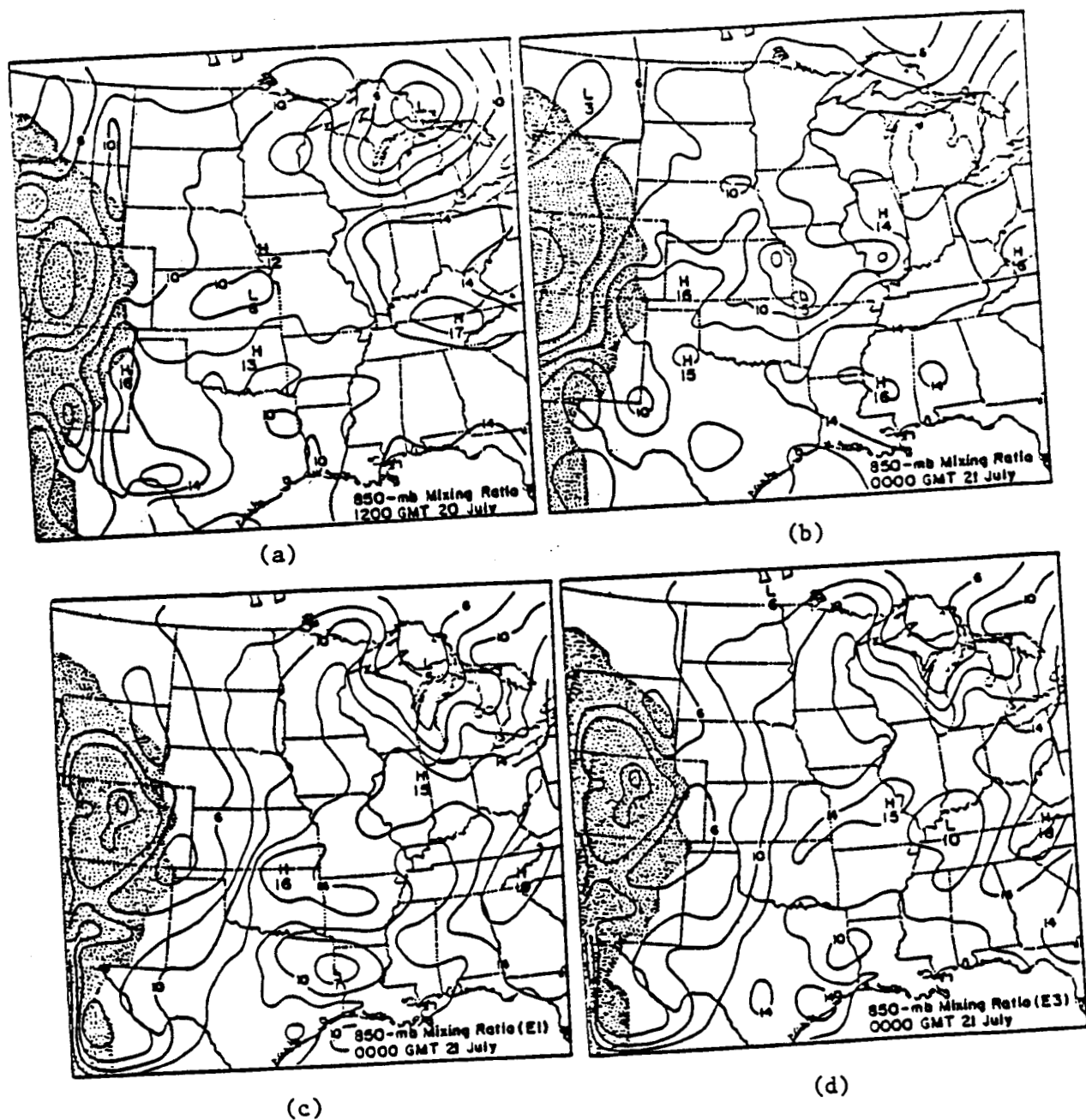


Figure 7.4 850-mb mixing-ratio (w) analyses. The stippled area represents the region where surface pressure is less than 850 mb. The contour interval is 2 g/kg.

- Observed 850-mb mixing ratio, valid 1200 GMT 20 July 1981
- Observed 850-mb mixing ratio, valid 0000 GMT 21 July 1981
- Forecast (E1) 850-mb mixing ratio, valid 0000 GMT 21 July 1981
- Forecast (E3) 850-mb mixing ratio, valid 0000 GMT 21 July 1981

same. The 850-mb winds over the western Gulf of Mexico at 1200 GMT 20 July are southerly, but by 0000 GMT 21 July they are westerly. The forecast winds are also westerly by 1500 GMT but the wind, to a less southerly direction, may have occurred so early as to prevent sufficient moisture to be advected from the Gulf of Mexico. The forecast moisture field for much of the eastern part of the domain generally agrees with the observed field. There are only small differences among the forecasts of 700-mb and 500-mb mixing ratio. One of these expected differences is due to the relative smoothness of the forecast mixing-ratio fields from E4.

Although the various combinations of data used in the initialization process produced some differences in the initial conditions of temperature and moisture, the forecast results from the seven experiments are very similar. This is illustrated in Fig. 7.5, which shows temperature-differences between E1 and E2 ($E1-E2$) for sigma-level 0.95. These differences correspond to the following times during the forecast period: 1200 GMT, 1500 GMT, and 1800 GMT 20 July, and 0000 GMT 21 July. Regions of significant initial temperature differences between E1 and E2 generally advect a small distance eastward, the magnitude of these differences decreasing markedly by 0000 GMT 21 July. This is especially true for the area of lower VAS temperature over Kansas. Although E1 and E2 have identical initial wind fields, by 1500 GMT wind direction differences and wind speed differences greater than 2 ms^{-1} are evident at all levels. The areas where wind speed differences are greatest generally correspond to areas of significant temperature differences between forecasts. After 1800 GMT, these wind-speed differences are less extensive. Moisture differences

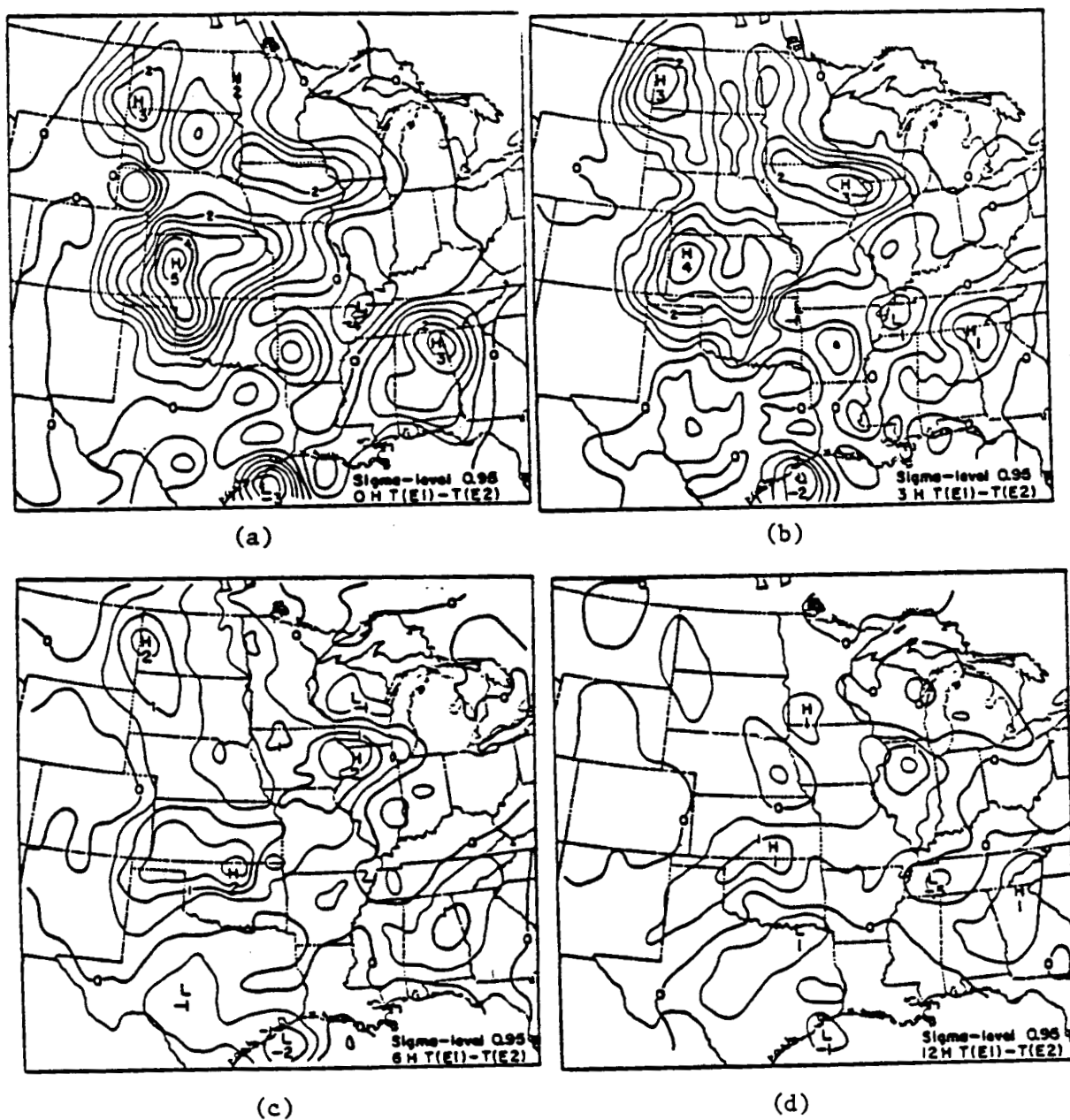


Figure 7.5 Temperature differences between E1 and E2 ($E1-E2$) for sigma level 0.95. The contour interval is 0.5°C .

- a. 1200 GMT 20 July 1981
- b. 1500 GMT 20 July 1981
- c. 1800 GMT 20 July 1981
- d. 0000 GMT 21 July 1981

between E1 and E2 decrease less than do temperature differences during the forecast period. This is to be expected because of the temperature fields response in the geostrophic-adjustment process.

7.4 Quantitative Precipitation Forecast (QPF) Results

To verify the QPF of experiments E1 through E7, observed rainfall data were taken from the publication, Hourly Precipitation Data, which is published by The National Climatic Center. Cumulative totals of the hourly rainfall for the forecast period, 1200 GMT 20 July and 0000 GMT 21 July, were plotted and subjectively analyzed (Fig. 3.7).

The small-scale convective precipitation events in western Iowa, Kansas, Texas, and Oklahoma were sufficiently isolated so that only two hourly-precipitation stations recorded any rain during the simulation period. Figure 3.7 indicates that more widespread precipitation occurred to the east of the VAS network, with one region in Missouri, southern Illinois and Kentucky, one in Wisconsin, one in Indiana, one in eastern Ohio and Pennsylvania, and finally one over the Florida panhandle and Georgia.

The 12-hour QPF from experiments E1 to E7 are shown in Fig. 7.6. Contours of precipitation (P) are logarithmically scaled by $\ln(R + 0.01) + 4.6$ where R is rainfall in centimeters. The relationship between these scaled contours and forecast precipitation is given in Table 7.2. The Florida-Georgia maximum was located reasonably by all of the forecasts, even though it was very close to the model's lateral boundary. Experiments E1 and E6 have the best

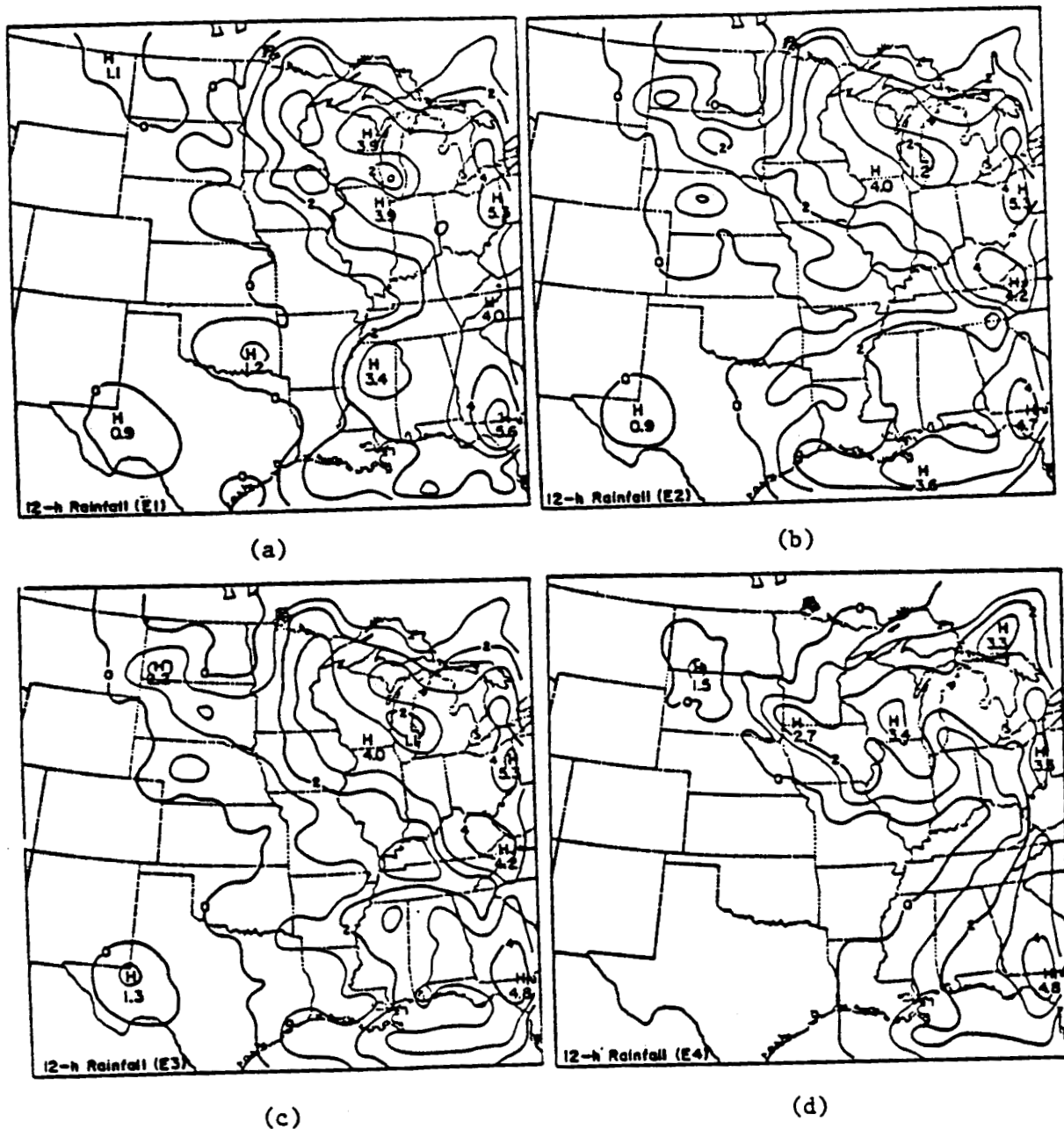
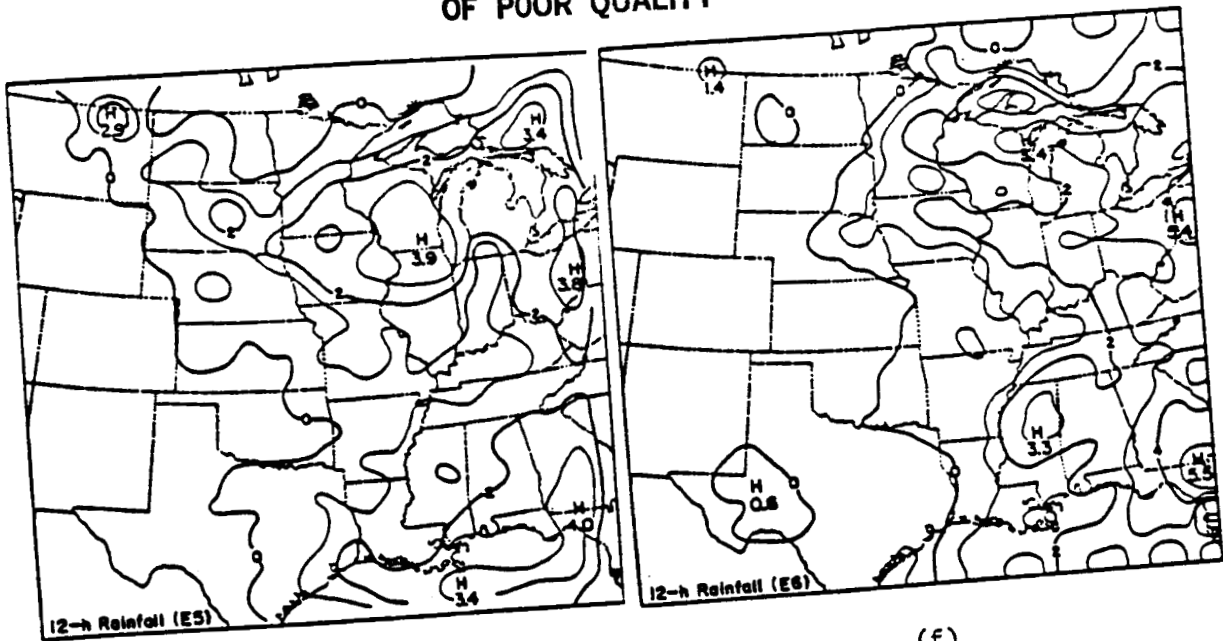


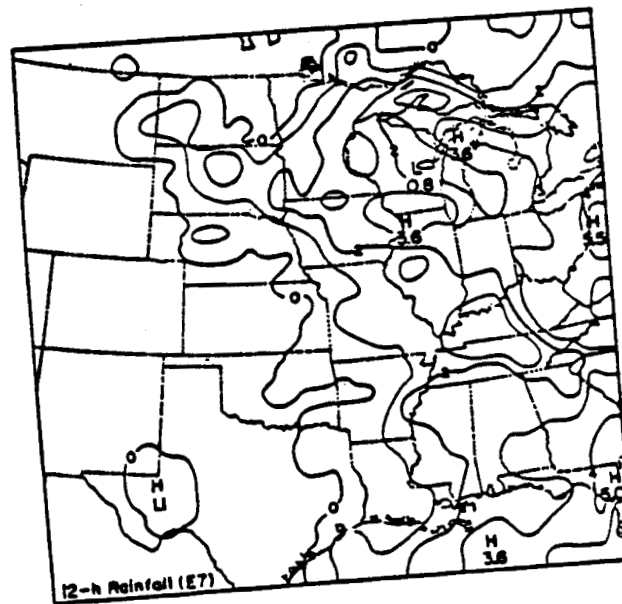
Figure 7.6 Total predicted rainfall during the 12-h forecast period, 1200 GMT 20 July to 0000 GMT 21 July 1981, for experiments E1 to E7. Rainfall amounts are logarithmically scaled (Table 7.2).

- a. E1
- b. E2
- c. E3
- d. E4
- e. E5
- f. E6
- g. E7



(e)

(f)



(g)

Table 7.2 Forecast Precipitation Scale

<u>P</u>	<u>R (cm)</u>
1	0.017
2	0.064
3	0.192
4	0.539
5	1.482
5	4.045
7	11.013

agreement with observed precipitation amounts for this area. The VAS data in E2, E3, and E7 prevented the spurious development of a precipitation maximum in Mississippi that occurred in E1 and E6. The maximum in Ohio and Pennsylvania was handled equally well by all forecasts except E4 and E5. The Wisconsin maximum was best forecast by E1, E2, E3, and E7. The use of a dynamic-initialization procedure worsened the precipitation forecast for Wisconsin, although the impact of the VAS data in the dynamic initialization was positive (compare E6 and E7). The poorest QPF for Wisconsin was produced by E4. The QPF's from E2 and E3 are nearly identical. This is consistent with the comparison of the verification statistics discussed in Section 7.2. A comparison of E1 with E6 and E3 with E7 indicates that the use of a dynamic-initialization procedure had little impact on the QPF. The QPF amounts from all of the experiments is less than the observed precipitation.

In an attempt to improve the QPF results, the model was initialized using a divergence field diagnosed from a mesoscale omega equation. This equation includes the effects of latent heating, which are estimated from the observed rainfall. This procedure has improved other precipitation forecasts, especially very short-range forecasts (Tarbell et al., 1981; Salmon, 1985). Hourly rainfall observations from 1200 GMT and 1300 GMT were used to determine the latent heating rates in the omega equation, which were then used to diagnose the divergent component of the initial wind field. In this case, however, this procedure had very little impact on the QPF amounts, probably because there were so few rainfall observations near the start of the

forecast period. Since this initialization technique was ineffective, the results were not tabulated with the other seven experiments.

None of the simulations predicted the Missouri-Illinois-Kentucky maximum satisfactorily. This is disappointing because this precipitation, associated with the widespread outbreak of convection over Missouri, was the most noteworthy weather event that occurred in the VAS region. There is some indication of a precipitation maximum in Missouri for E2, E3, and E7 which all use VAS data. However, the reason for the model's failure to better predict this precipitation is unknown. Much of the precipitation that fell in Missouri and southern Illinois came near the end of the forecast period. If there was a problem of timing, then extending the forecast period several hours might allow reasonable precipitation forecasts.

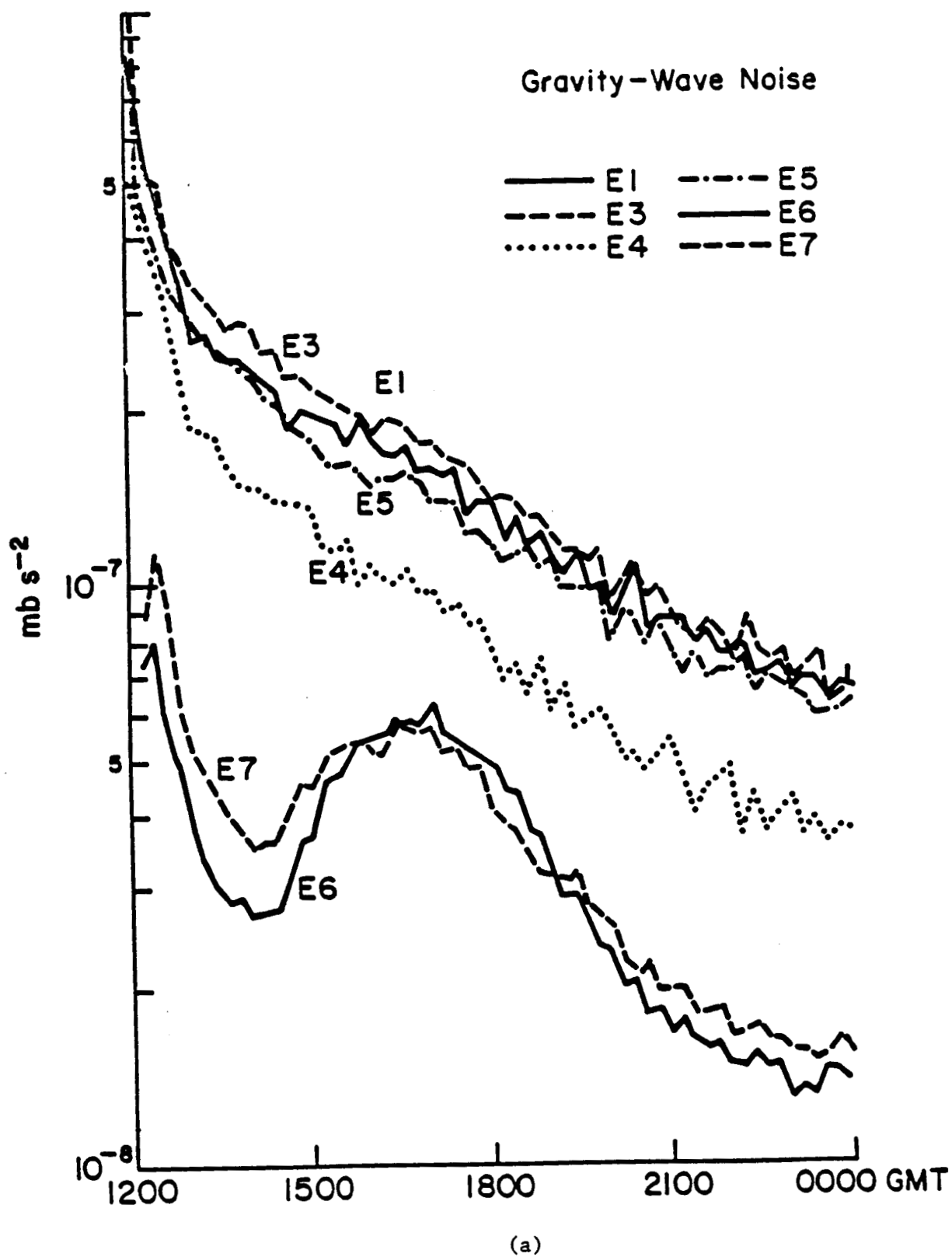
7.5 Gravity-Inertia Wave Characteristics of the Forecasts

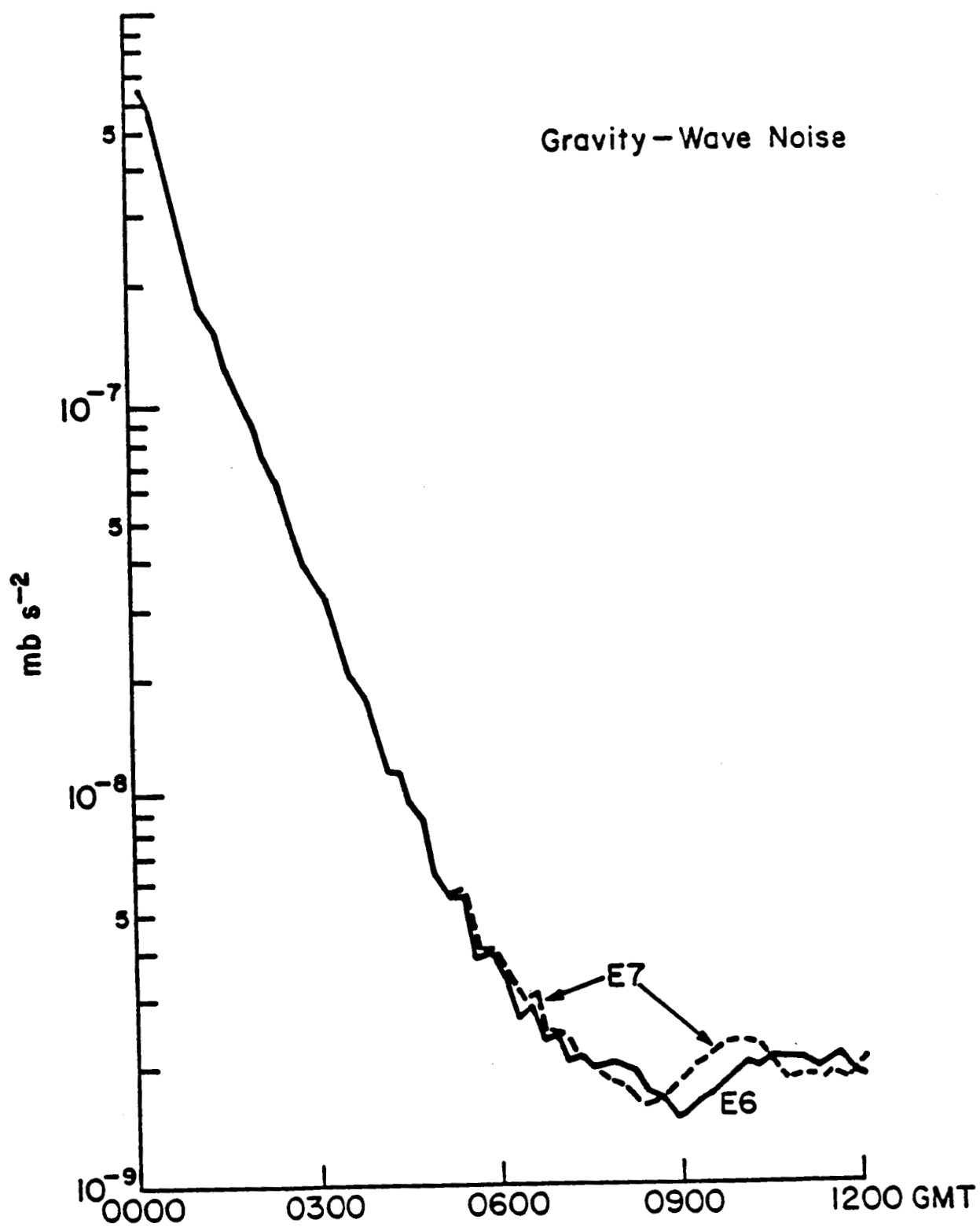
Gravity-inertia waves, often referred to as "noise," may obscure meteorologically important motions during the first twelve hours of a numerical forecast (Sasaki, 1969; Haltiner and Williams, 1980). In the PSU mesoscale model $|\partial p^*/\partial t|$ and $|\partial^2 p^*/\partial t^2|$ are used as measures of model-generated noise. These domain-averaged derivatives are calculated every time-step. They are appropriate indications of noise because they are related to the divergence and its temporal rate of change (Warner et al., 1978).

Plotted in Fig. 7.7a are values of $|\partial^2 p^*/\partial t^2|$ during the forecast period for experiments E1, E3, E4, E5, E6, and E7. The preforecast noise values were plotted for E6 and E7 in Fig. 7.7b. The results of

Figure 7.7 Gravity-wave noise as shown by the temporal variation of $|\partial^2 p^* / \partial t^2|$ for all experiments except E2.

- a. Gravity-wave noise during the forecast period, 1200 GMT 20 July to 0000 GMT 21 July 1981
- b. Gravity-wave noise of the dynamic-initialization experiments during the preforecast period, 0000 GMT to 1200 GMT 20 July 1981





(b)

E2 were excluded because they are almost identical to those in E3. Noise statistics from every sixth time-step were used in these graphs.

In the static initialization experiments (E1 to E5) there is a sharp drop in noise during the first three hours and then the decline is more gradual. The gravity-inertia wave noise associated with E4 is significantly lower than that found in E1, E3, and E5. This is probably because the initial fields (in E4) of mass and momentum were based upon a previous forecast and were therefore more closely balanced. The noise plots for E1, E3, and E5 are very similar. For these three experiments, noise is lowest when the initial conditions included only VAS observations and highest when both radiosonde and VAS data were employed.

The noise characteristics of experiments E6 and E7 are very much alike and also rather interesting. During the first six hours of the preforecast period (Fig. 7.7b), the noise is nearly identical (only one line was drawn) because both E6 and E7 have the same initial conditions at 0000 GMT 20 July. The plot begins to diverge as the effect of nudging toward two different target analyses becomes more important. The addition of VAS data in the target analysis results in no systematic increase or decrease in model noise during the preforecast period. Noise values of E6 and E7 are relatively low (nearly $10^{-9} \text{ mb s}^{-2}$, by the end of the preforecast period, however these values jumped nearly two orders of magnitude (Fig. 7.7a) when nudging was abruptly discontinued at the start of the forecast period. Despite this dramatic increase, noise values for E6 and E7, after the start of the forecast, are significantly lower than the noise for any of the

statically initialized experiments. After a sharp decline between 1200 and 1400 GMT, there is a significant increase in noise and a second peak is evident at about 1700 GMT. Noise statistics are generally higher for E7 than for E6 during the forecast period.

8.0 SUMMARY AND CONCLUSIONS

Several procedures were tested for including VAS-derived temperature and moisture data in objective analyses that served as the basis for the initial conditions of mesoscale model simulations. Comparison of objective and subjective temperature and moisture analyses of the VAS data showed that they were being successfully incorporated by the objective-analysis procedure of the Penn State/NCAR mesoscale modeling system. Two procedures that used a combination of radiosonde and VAS temperature and moisture data produced similar final analyses. Model initial conditions based on radiosonde data only and on both radiosonde and VAS data were thoroughly compared in terms of which was more conducive to allowing the mesoscale model to develop realistic convection over the central United States. Although there were some small-scale differences between the NOVAS and VAS analyses, neither appeared to be more conducive to the outbreak of convection. The use of VAS data did have some impact on the actual rainfall forecast but not over the region of heaviest observed rainfall for this case.

There are several reasons why the addition of VAS data may have failed to significantly improve the objective analyses. The objective-analysis procedure that combined the VAS and radiosonde data may have been inadequate, the quality of the VAS data may have been

too poor, or there may have been no important mesoscale features that were resolved better by VAS than by the conventional radiosondes.

Even though the forecast-verification statistics were generally similar for all the forecasts, there were some interesting trends. When VAS data were used in a static initialization of the model, a small improvement in the quality of the forecast temperature and moisture fields was apparent at all levels when verified against a VAS analysis. It was also found that the VAS data allowed more accurate predictions of temperature and moisture when no radiosonde data were used. Winds verified worse when VAS data were used in the initial conditions. This was not too surprising because VAS-scale structure does not exist in the verification analysis and the VAS data might have imparted additional mesoscale detail to the wind field during the geostrophic-adjustment process in the forecast. This could be clarified by verifying forecast winds against individual observations. Finally, the forecast skill was not sensitive to the specific method of incorporating VAS data into the objective analysis using successive correction techniques.

The results from the dynamic-initialization and the static-initialization experiments which use only radiosonde data were much alike. Apparently the dynamic-initialization procedure had little impact. Except for low-level temperature, which verified worse when VAS data were used, the positive impact of the VAS data in the dynamic initialization was comparable to that in the static initialization.

The QPF results were rather insensitive to the type of data or the analysis procedure used to define the initial conditions. All of the

model simulations, except E4 and E5, adequately forecasted precipitation over Wisconsin, eastern Ohio and Pennsylvania, and the Florida panhandle and Georgia. Experiments E4 and E5, which used no radiosonde data, had to rely on an initial wind field obtained from the NMC global analysis. Precipitation amounts were underforecast in all of the experiments. Unfortunately, all of the simulations failed to predict the large area of convection over Missouri and Illinois. The reason for the model's failure to forecast this precipitation is not known, although poor model timing in forecasting the onset of the convection or the existence of underforecast relative humidities are two possibilities.

REFERENCES

- Anthes, R.A., 1977: A cumulus parameterization scheme utilizing a one-dimensional cloud model. Mon. Wea. Rev., 105, 270-286.
- Anthes, R.A. and T.T. Warner, 1978: The development of mesoscale models suitable for air pollution and other mesometeorological studies. Mon. Wea. Rev., 106, 1045-1078.
- Anthes, R.A. and D. Keyser, 1979: Tests of a fine mesh model over Europe and the United States. Mon. Wea. Rev., 107, 963-984.
- Anthes, R.A., Y.H. Kuo, S.G. Benjamin and Y.F. Li, 1982: The evolution of the mesoscale environment of severe local storms: preliminary modeling results. Mon. Wea. Rev., 110, 1187-1213.
- Atkins, M.J. and M.V. Jones, 1975: An experiment to determine the value of satellite infrared spectrometer (SIRS) data in numerical forecasting. Meteor. Mag., 104, 125-142.
- Atlas, R., M. Ghil and M. Halem, 1982: The effect of model resolution and satellite sounding data on GLAS model forecasts. Mon. Wea. Rev., 110, 662-682.
- Benjamin, S.G., 1983: Some Effects of Heating and Topography on the Regional Severe Storm Environment. Ph.D. Thesis, The Pennsylvania State University, 265 pp.
- Benjamin, S.G. and N.L. Seaman, 1985: A simple scheme for objective analyses in curved flow. Mon. Wea. Rev., 113, 1184-1198.
- Blackadar, A.K., 1976: Modeling the nocturnal boundary layer. Preprints, Third Symp. on Atmospheric Turbulence, Diffusion, and Air Quality, Raleigh, Amer. Meteor. Soc., 46-49.
- Blackadar, A.K., 1978: High resolution models of the planetary boundary layer. Advances in Environmental Science and Engineering, 1, Eds. J.R. Pfafflin and E.N. Ziegler, Gordon and Breach, 276 pp.
- Blackadar, A.K., 1979: Modeling pollutant transfer during daytime convection. Preprints, Fourth Symp. on Atmospheric Turbulence, Diffusion, and Air Quality, Reno, Amer. Meteor. Soc., 443-447.
- Bonner, W., P. Lemar, R. van Haaren, A. Desmarais and H. O'Neil, 1976: A test of the impact of NOAA-2 VTPR soundings on operational analyses and forecasts. NOAA Tech. Memo. NWS-57, NMC, Washington, DC, 43 pp. [NTIS PB-256075].

- Brown, J.A., Jr. and K.A. Campana, 1978: An economic time-differencing scheme for numerical weather prediction models. Mon. Wea. Rev., 106, 1125-1136.
- Chesters, D., L.W. Uccellini, H. Montgomery, A. Mostek and W. Robinson, 1981: Assessment of the first radiances received from the VISSR Atmospheric Sounder (VAS) instrument. NASA TM 83827, 124 pp. [NTS-82N19730].
- Chesters, D., L.W. Uccellini and A. Mostek, 1982: VISSR Atmospheric Sounder (VAS) simulation experiment for a severe storm environment. Mon. Wea. Rev., 110, 198-216.
- Chesters, D., L.W. Uccellini and W. Robinson, 1983: Low-level water vapor fields from the VISSR Atmospheric Sounder (VAS) "split-window" channels. J. Climate Appl. Meteor., 22, 725-743.
- Cram, J.M. and M.L. Kaplan, 1984: Variational assimilation of VAS data into the MASS model. Preprints, Tenth Conf. on Weather Forecasting and Analysis, Clearwater Beach, Amer. Meteor. Soc., 373-379.
- Cressman, G.P., 1959: An operational objective analysis system. Mon. Wea. Rev., 87, 367-374.
- Druyan, L.M., T. Ben-Amram, Z. Alperson and G. Ohring, 1978: The impact of VTPR data on numerical forecasts of Israel Meteorological Service. Mon. Wea. Rev., 106, 859-869.
- Ghil, M., M. Halem and R. Atlas, 1979: Time-continuous assimilation of remote-sounding data and its effect on weather forecasting. Mon. Wea. Rev., 107, 140-171.
- Gruber, A. and C.D. Watkins, 1982: Statistical assessment of the quality of TIROS-N and NOAA-6 satellite soundings. Mon. Wea. Rev., 110, 867-876.
- Haltiner, G.J. and R.T. Williams, 1980: Numerical Prediction and Dynamic Meteorology. John Wiley & Sons, Inc., New York, 477 pp.
- Hillger, D.W. and T.H. Vonder Haar, 1977: Deriving mesoscale temperature and moisture fields from satellite radiance measurements over the United States. J. Appl. Meteor., 16, 715-726.
- Hoke, J.E., 1976: Initialization of Models for Numerical Weather Prediction by a Dynamic-Initialization Technique. Ph.D. Thesis, The Pennsylvania State University, 202 pp.

- Hoke, J.E. and R.A. Anthes, 1976: The initialization of numerical models by a dynamic-initialization technique. Mon. Wea. Rev., 104, 1551-1556.
- Hoke, J.E., 1983: Several methods for initializing mesoscale forecast models. Mesoscale Meteorology - Theories, Observations and Models, Eds. D.K. Lilly and T. Gal-Chen, Reidel Publishing Company, 143-155.
- Inman, R.L., 1970: Operational objective analysis schemes at the National Severe Storms Laboratory. Tech. Cir. No. 10, National Severe Storms Lab., Environmental Sciences Services Administration, Norman, OK.
- Jedlovek, G.J., 1984: A statistical evaluation and comparison of VISSR Atmospheric Sounder (VAS) data and corresponding rawinsonde measurements. NASA TM 82575, 11 pp.
- Keyser, D.A., 1983: Documentation for GSFC VAS sounding data for 20 July 1981 expended retrievals. Goddard Laboratory for Atmospheric Sciences, 7 pp.
- Lee, T., D. Chesters and A. Mostek, 1983: The impact of conventional surface data upon VAS regression retrievals in the lower troposphere. J. Climate Appl. Meteor., 22, 1853-1873.
- McPherson, R.D., 1975: Progress, problems, and prospects in meteorological data assimilation. Bull. Amer. Meteor. Soc., 56, 1154-1166.
- Messinger, F. and A. Arakawa, 1976: Numerical methods used in atmospheric models. GARP Publications Series No. 14, WMO/ICSU Joint Organizing Committee, 64 pp.
- Mostek, A., D.A. Keyser, T. Lee and L.W. Uccellini, 1983: Remote retrievals for the 6 March 1982 AVE/VAS special network. Goddard Laboratory for Atmospheric Sciences, 15 pp.
- Ohring, G., 1979: Impact of satellite temperature sounding data on weather forecasts. Bull. Amer. Meteor. Soc., 60, 1142-1147.
- Petersen, R.A., L.W. Uccellini, D. Chesters, A. Mostek and D.A. Keyser, 1982: The use of VAS satellite in weather analysis, prediction and diagnosis. Preprints, Ninth Conf. on Weather Forecasting and Analysis, Seattle, Amer. Meteor. Soc., 219-226.

- Petersen, R.A., D.A. Keyser, A. Mostek and L.W. Uccellini, 1983a: Severe storms analysis and forecasting techniques using VAS satellite data. Preprints, Thirteenth Conf. on Severe Local Storms, Tulsa, Amer. Meteor. Soc., 29-32.
- Petersen, R.A., D.A. Keyser, A. Mostek and L.W. Uccellini, 1983b: Techniques for diagnosing phenomena affecting aviation using VAS satellite data. Preprints, Ninth Conf. on Aerosp. and Aeron. Meteor., Omaha, Amer. Meteor. Soc., 12-17.
- Philips, N., L. McMillin, A. Gruber and D. Wark, 1979: An evaluation of early operational temperature soundings from TIROS-N. Bull. Amer. Meteor. Soc., 60, 1188-1197.
- Salmon, E.M., 1985: Short-Term Precipitation Forecasts Based on an Initialization Using a Diagnosed Divergent-Wind Component. M.S. Thesis, The Pennsylvania State University, 122 pp.
- Sasaki, Y., 1969: Proposed inclusion of time variation terms, observational and theoretical, in numerical variational analysis. J. Meteor. Soc., Japan, Series II, 47, 115-124.
- Smith, W.L., H.M. Woolf and C.M. Hayden, 1979: The TIROS-N operational vertical sounder. Bull. Amer. Meteor. Soc., 60, 1177-1187.
- Smith, W.L., V.E. Suomi, W.P. Menzel, H.M. Woolf, L.A. Sromovsky, H.E. Revercomb, C.M. Hayden, D.N. Erickson and F.R. Mosher, 1981: First sounding results from VAS-D. Bull. Amer. Meteor. Soc., 62, 232-236.
- Smith, W.L., V.E. Suomi, F.X. Zhou and W.P. Menzel, 1982: Nowcasting applications of geostationary satellite atmospheric sounding data. Nowcasting, Ed. K.A. Browning, Academic Press, 123-135.
- Smith, W.L., 1983: The retrieval of atmospheric profiles from VAS geostationary radiance observations. J. of the Atmos. Sciences, 40, 2025-2035.
- Suomi, V.E., T. Vonder Haar, R. Krauss and A. Stamm, 1971: Possibilities for sounding the atmosphere from a geosynchronous spacecraft. Space Research, 11, 609-617.
- Tarbell, T.C., T.T. Warner and R.A. Anthes, 1981: An example of the initialization of the divergent wind component in a mesoscale numerical weather prediction model. Mon. Wea. Rev., 109, 77-95.

- Tracton, M.S., A.J. Desmarais, R.J. van Haaren and R.D. McPherson, 1980: The impact of satellite soundings upon the National Meteorological Center's analysis and forecast system - the Data Systems Tests results. Mon. Wea. Rev., 109, 197-200.
- Warner, T.T., R.A. Anthes and A.L. McNab, 1978: Numerical simulations with a three-dimensional mesoscale model. Mon. Wea. Rev., 106, 1079-1099.
- Zhang, D.L. and R.A. Anthes, 1982: A high resolution model of the planetary boundary layer--sensitivity tests and comparisons with SESAME-79 data. J. Appl. Meteor., 21, 1594-1609.